AFOSR·TR· 89·0001

AD-A204 487

MILLIMETER-WAVE GENERATION VIA PLASMA THREE-WAVE MIXING

R.W. Schumacher and J. Santoru

Hughes Research Laboratories
3011 Malibu Canyon Road
Malibu, California 90265

June 1988

F49620-85-C-0059

Annual Report

April 1, 1987 through March 31, 1988

AIR FORCE OFFICE OF SCIENTIFIC RESEARCH
Bolling Air Force Base
Washington, D.C. 20332-6448

Accession For

NTIS GRA&I		☒
DTIC TAB		☐
Unannounced		☐
Just.ification		

By

Distribution/

Availability Codes

Dist	Avail and/or Special
A-1	

`89 2 10 129

DISCLAIMER NOTICE

THIS DOCUMENT IS BEST QUALITY
PRACTICABLE. THE COPY FURNISHED
TO DTIC CONTAINED A SIGNIFICANT
NUMBER OF PAGES WHICH DO NOT
REPRODUCE LEGIBLY.

REPORT DOCUMENTATION PAGE

Form Approved
OMB No. 0704-0188

1a. REPORT SECURITY CLASSIFICATION	1b. RESTRICTIVE MARKINGS
Unclassified	DTIC FILE COPY

2a. SECURITY CLASSIFICATION AUTHORITY	3. DISTRIBUTION / AVAILABILITY OF REPORT
2b. DECLASSIFICATION / DOWNGRADING SCHEDULE	Unlimited

4. PERFORMING ORGANIZATION REPORT NUMBER(S)	5. MONITORING ORGANIZATION REPORT NUMBER(S)
	AFOSR·TR· 89 0001

6a. NAME OF PERFORMING ORGANIZATION	6b. OFFICE SYMBOL (If applicable) HRL	7a. NAME OF MONITORING ORGANIZATION
Hughes Research Laboratories		Air Force Office of Scientific Research/NP

6c. ADDRESS (City, State, and ZIP Code)	7b. ADDRESS (City, State, and ZIP Code)
3011 Malibu Canyon Road Malibu, CA 90265	Bolling Air Force Base, Bldg. 410 Washington, D.C. 20332-6448

8a. NAME OF FUNDING/SPONSORING ORGANIZATION Air Force Office of Scientific Research/NP	8b. OFFICE SYMBOL (If applicable) NP	9. PROCUREMENT INSTRUMENT IDENTIFICATION NUMBER F49620-85-C-0059

8c. ADDRESS (City, State, and ZIP Code)
Bolling Air Force Base, Bldg. 410
Washington, D.C. 20332-6448

10. SOURCE OF FUNDING NUMBERS

PROGRAM ELEMENT NO.	PROJECT NO.	TASK NO.	WORK UNIT ACCESSION NO.
61102F	2301	A8	

11. TITLE (Include Security Classification)
MILLIMETER-WAVE GENERATION VIA PLASMA THREE-WAVE MIXING (U)

12. PERSONAL AUTHOR(S)
Robert W. Schumacher and Joseph Santoru

13a. TYPE OF REPORT Annual	13b. TIME COVERED FROM 87/4/1 TO 88/3/31	14. DATE OF REPORT (Year, Month, Day) 1988 June	15. PAGE COUNT

16. SUPPLEMENTARY NOTATION

17. COSATI CODES			18. SUBJECT TERMS (Continue on reverse if necessary and identify by block number)
FIELD	GROUP	SUB-GROUP	

19. ABSTRACT (Continue on reverse if necessary and identify by block number)

Plasma three-wave mixing is a collective phenomena whereby electron-beam-driven electron plasma waves (EPWs) are nonlinearly coupled to an electromagnetic (EM) radiation field. The Hughes objective is to investigate the basic physics of three-wave mixing in the mm-wave regime and to establish the scaling of mm-wave characteristics with beam and plasma parameters. Our approach is to employ two counterinjected electron beams in a plasma-loaded circular waveguide to drive counterstreaming EPWs. The nonlinear coupling of these waves generates an EM waveguide mode which oscillates at twice the plasma frequency and is coupled out into rectangular waveguides. Independent control of the waveguide plasma, beam voltage, and beam current is exercised to allow a careful parametric investigation of beam transport, EPW dynamics and three-wave-mixing physics.

20. DISTRIBUTION / AVAILABILITY OF ABSTRACT ☐ UNCLASSIFIED/UNLIMITED ☒ SAME AS RPT ☐ DTIC USERS	21. ABSTRACT SECURITY CLASSIFICATION Unclassified
22a. NAME OF RESPONSIBLE INDIVIDUAL Robert W. Schumacher	22b. TELEPHONE (Include Area Code) (213)317-5439	22c. OFFICE SYMBOL NP

DD Form 1473, JUN 86   Previous editions are obsolete.   SECURITY CLASSIFICATION OF THIS PAGE

UNCLASSIFIED

The beam-plasma experiment, which employs a wire-anode discharge to generate high-density ($<10^{13}$ cm^{-3}) plasma in a 3.8-cm-diameter waveguide, has been used to generate radiation at frequencies from 7 to 60 GHz. Two cold-cathode, secondary-emission electron guns (<90 kV, and <6.5 A) are used to excite the EPWs. Output radiation is observed only when both beams are injected, and the total beam current exceeds a threshold value of 3 A. The threshold is related to the self-magnetic pinch of each beam which increases the beam density and growth rate of the EPWs. Above the pinch current, the mm-wave power scales nonlinearly with beam current up to peak values of 8 kW, which represents a peak beam-power conversion efficiency of 4% and a conversion efficiency of about 0.4% when averaged over the full mm-wave pulse.

During the third year of our program, we investigated the radiation characteristics using 15-cm-long and 1.9-cm-long waveguide cavities. The radiation modulation has a low-frequency (10 to 40 MHz) component which is controlled by the ion dynamics, and a high-frequency (~350 MHz) component. The low-frequency modulation depends on the beam current density and the background plasma density whereas the high-frequency modulation is largely independent of the experimental parameters. The 1.9-cm cavity imposes a longitudinal boundary condition on the beam-excited EPWs that results in normal modes in the voltage-tuning pattern; this is not observed using the 15-cm cavity. Experiments using low He gas pressure confirmed that collisions are a controlling factor in the saturation of the three-wave mixing process.

TABLE OF CONTENTS

LIST OF ILLUSTRATIONS

SECTION 1

INTRODUCTION

This annual report describes Hughes Research Laboratories' (HRL) investigation of millimeter-wave generation via plasma three-wave mixing. Specifically, we examined the plasma-physics issues relating to the generation of millimeter waves via the nonlinear interaction of two electron-beam-driven electrostatic plasma waves. The program supported an experimental effort to investigate the scaling of millimeter-wave power, frequency, and modulation with electron-beam and plasma parameters. We also conducted a comparison of experimental results with theoretical studies performed by M. Rosenberg and N.A. Krall of JAYCOR (San Diego, Calif.).

Our approach to this investigation is to employ two counterinjected electron beams in a plasma-loaded waveguide to drive counterstreaming electron plasma waves (EPWs). The nonlinear coupling of these waves generates an electromagnetic waveguide mode that oscillates at twice the plasma frequency. Independent control of waveguide plasma density, gas species, beam voltage, and beam current allows a careful parametric study of three-wave mixing physics. Although there have been earlier experimental studies of radiation generation in a plasma at twice the plasma frequency,[1-4] our program is the first to use high-power ($\leq$90 kV, $\leq$6.5 A) beams in a high-density, plasma-filled waveguide to generate substantial radiation power levels ($\leq$8 kW) at millimeter-wave frequencies.

We made significant progress toward understanding and experimentally demonstrating the basic physics of plasma three-wave mixing in the past year. The following items summarize our accomplishments and experimental results to date.

- Significant millimeter-wave radiation is observed only when beams counterstream and only when each beam current is adjusted above a threshold of about 1.5 A.

- Frequency equals twice the plasma frequency, and scales as $I_d^{1/2}$ up to 60 GHz.

- Peak radiation power was ≤ 8 kW with peak efficiency $\leq 4\%$.

- We learned that power and efficiency increase nonlinearly with beam current.

- Power increases with ion mass.

- Radiation is coherent, but is amplitude modulated at frequencies $<\omega_{pi}$.

- Modulation frequency (~ 40 MHz) scales as $M_i^{1/2}$.

- Beam-voltage tuning ($V_B^{LV} = V_B^{HV}$) is required only at low current (corresponds to weak-turbulence regime).

- Optimum beam voltage increases with frequency/plasma density (30 kV at 30 GHz, 43 kV at 60 GHz for 15-cm-long plasma).

- Beam steering via quadrupole fields optimizes power.

- Bennett pinch dominates beam dynamics and power scaling.

- Radiation modulation depends on waveguide plasma density and beam current, and correlates with electrostatic probe measurements.

- Experiments performed using a 1.9-cm-long beam-interaction cavity demonstrate that the cavity boundary conditions determine the allowed electron-plasma-wave modes.

- Radiation power nearly saturates at high beam current when low background gas pressure is used.

- Hollow-Cathode-Plasma (HCP) electron-gun development under Hughes Aircraft IR&D indicates beam current densities up to 50 A/cm^2 will be available after a system upgrade is performed next year.

In the following sections we will review our significant technical progress in understanding and demonstrating the basic physics of millimeter-wave generation via plasma three-wave mixing. In Section 2 we present a simple plasma three-wave mixing theoretical model. This is followed by a discussion of the experimental configuration. In Section 3 we present our experimental results, including radiation power and modulation scaling with beam current, plasma density, and waveguide cavity length. A draft of a paper which is being prepared for Physics of Fluids is enclosed in Appendix A.

SECTION 2

APPROACH

In this section we present our simple theoretical model describing the plasma three-wave mixing process. We conclude with a description of the experimental apparatus which utilizes the three-wave mixing process to efficiently generate electromagnetic radiation (efficiency $\leq 4\%$).

2.1 THEORY

Plasma three-wave mixing is based on the beam-plasma-interaction problem[5],[6] that has been explored in numerous publications for almost 40 years. Beam-plasma phenomena for radiation generation is attractive because of the ease with which intense, high-frequency electron-plasma waves (EPWs) can be excited when a high-power electron beam is injected into a dense plasma. However, the problem of efficiently coupling the power in the electrostatic waves to a radiation field has hindered[7] all previous attempts to use plasmas in millimeter-wave sources or amplifiers. In the following theoretical discussion, we will summarize the basic physics of beam-driven EPWs and present a simple kinematic model for the nonlinear coupling of two EPWs to the radiation field in a plasma-filled waveguide.

2.1.1. Excitation of EPWs

We begin the discussion by restricting the treatment to a weak, cold beam with density n_b and velocity v_b. By "weak" beam we mean that the ratio of beam density to plasma electron density,

$$\frac{n_b}{n_e} \equiv \epsilon \quad , \tag{1}$$

is small compared with unity ($\epsilon \ll 1$); by "cold beam" we mean that the beam temperature is much less than the beam energy.

5

Under these conditions, linear hydrodynamic theory[5,6,8,9] (electron-beam flow through an electron fluid that is stationary in the lab frame with a fixed ion background) shows that the beam will excite EPWs with phase velocity

$$\frac{\omega_e}{k_e} \simeq v_b \quad , \tag{2}$$

and, with the well-known Bohm-Gross dispersion,

$$\omega_e^2 = \omega_p^2 + 3k_e^2 v_{th}^2 \simeq \omega_p^2 \quad , \tag{3}$$

where ω_e and k_e are the EPW frequency and wave number, v_{th} is the plasma-electron thermal speed, and ω_p is the plasma frequency given by

$$\omega_p = \left(\frac{4\pi n_e e^2}{m_e} \right)^{1/2} \quad . \tag{4}$$

Because v_{th} is much less than v_b, the second term in Eq. (3) is much less than ω_p^2, so we have $\omega_e \simeq \omega_p$. The waves will grow along the beam trajectory with temporal growth rate,

$$\Gamma_t = \frac{3^{1/2}}{2^{4/3}} \epsilon^{1/3} \omega_e \quad , \tag{5}$$

and spatial growth rate,[10]

$$\Gamma_z = \frac{3^{1/6}}{2^{4/3}} \epsilon^{1/3} \left(\frac{v_b}{v_{th}} \right)^{2/3} k_e \quad . \tag{6}$$

The linewidth of the excited waves expressed in terms of wave number spread is also related to beam strength ϵ according to

$$\frac{\Delta k_e}{k_e} \sim \frac{3}{2^{5/6}} \, \epsilon^{1/3} \quad . \tag{7}$$

Nonlinear theory[8,9] shows that the EPW gains energy from the beam until it saturates by trapping beam electrons and broadening the beam-velocity distribution function. The saturated energy density in the EPW is given by

$$W = \frac{\langle E^2 \rangle}{4\pi} = \frac{n_b m_e v_b^2}{2} \left(\frac{\epsilon}{2}\right)^{1/3} \quad . \tag{8}$$

Because the factor $n_b m_e v_b^2/2$ is just the energy density in the electron beam, Eq. (8) shows that the fraction of beam energy coupled to EPW energy is $\sim (\epsilon/2)^{1/3}$. Note that for $n_b/n_e = 4\%$, up to 27% of the beam energy can be transferred to the EPWs.

The ratio $W/n_e T_e$ (where $n_e T_e$ is the plasma energy density) quantifies the strength of the beam-plasma interaction. For $W/n_e T_e$ greater than a few percent, the electric fields in the EPW begin to modify the plasma through ponderomotive-force effects. In this regime the EPWs and the plasma become strongly coupled and the beam-plasma system is said to be in the strong turbulence regime. In the opposite limit, where W is so small that

$$W/n_e T_e < (k_e \lambda_D)^2 \quad , \tag{9}$$

where λ_D is the electron Debye length $[\lambda_D = (kT_e/4\pi n_e e^2)^{1/2}]$, the beam-plasma system is said to be weakly turbulent.

2.1.2. Coupling of the EPWs to the Radiation Field

The oscillating field of the EPW contains the power that we wish to extract from the electron beam, but the power is trapped in the plasma as an electrostatic wave and must be coupled out in some manner as an electromagnetic mode. The Hughes solution to

the coupling problem is to use two counterstreaming electron
beams to excite two counterstreaming EPWs, as shown in Figure 1.
These two waves are then nonlinearly coupled to a TM
electromagnetic waveguide mode via plasma three-wave mixing. In
this process, the electric field of one wave induces a velocity
increment δv_e in the electron density fluctuations δn_e present in
the second wave, thereby generating a nonlinear source current
that is expressed as

$$J = e\delta n_e \delta v_e \quad .\tag{10}$$

This source current is nonlinear because it is a product of two
first-order fluctuations of the two linear, primary waves.

The plasma three-wave-mixing process can be described
quantitatively by using the dispersion relation for the plasma-
loaded-waveguide mode and the energy and momentum conservation
relations for three-wave mixing:

$$[\text{dispersion}] \qquad \omega_o^2 = \omega_p^2 + \omega_c^2 + k_o^2 c^2 \tag{11}$$

$$[\text{energy conservation}] \qquad \omega_o = \omega_{p_1} + \omega_{p_2} = 2\omega_p \tag{12}$$

$$[\text{momentum conservation}] \qquad \vec{k}_{e_1} + \vec{k}_{e_2} = \vec{k}_o \quad . \tag{13}$$

In these relations ω_o is the electromagnetic-waveguide-mode
frequency; ω_{p1} and ω_{p2} are the EPW angular frequencies; ω_c is the
waveguide-cutoff frequency in vacuum; k_{e1} and k_{e2} are the EPW
wave numbers; and k_o is the electromagnetic wave number.
Dispersion for each beam-mode plasma wave is described by
Eq. (2). As a consequence of wave-energy conservation
[Eq. (12)], the current J [of Eq. (10)] oscillates at twice the
EPW frequency. The oscillating axial current then couples to a
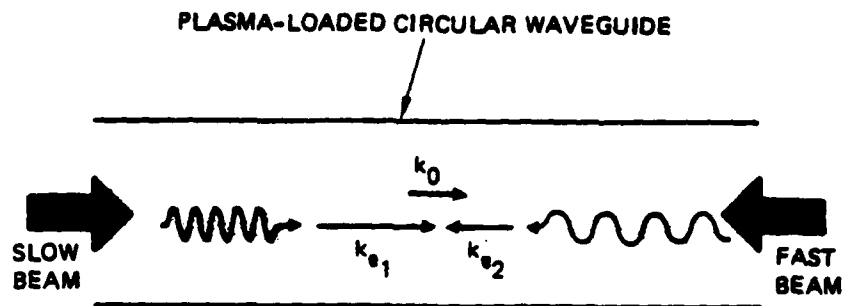TM electromagnetic waveguide mode at $2\nu_p$.

Figure 1. Beam-plasma-waveguide system.

The beam speeds, and thus the phase velocities of the EPWs, are always smaller than the phase velocity ($\geq c$) of the electromagnetic wave. Consequently, k_{e1} and k_{e2} will be larger than k_o. To satisfy Eq. (13) with collinear, but oppositely directed EPWs, the two electron-beam speeds must therefore be unequal for finite k_o. Cutoff waveguide modes with $k_o=0$ will be excited for equal beam speeds. The beam-speed difference can be expressed in terms of the plasma-waveguide parameters by solving Eqs. (2), (3), (11), (12), and (13) simultaneously. Inserting Eq. (12) into (11) and solving for k_o, we obtain the waveguide-mode wave number:

$$k_o = \frac{\left(3\omega_p^2 - \omega_c^2\right)^{1/2}}{c} .$$

(14)

This equation shows that ω_p must be greater than or equal to $3^{-1/2} \omega_c$ in order to couple to a waveguide mode. Inserting Eqs. (2) and (3) into (13) and equating the result to (14), we obtain the desired equation that relates the beam speeds to the plasma-waveguide parameters:

$$v_{b_2} - v_{b_1} = \frac{\left(3 - \omega_c^2/\omega_p^2\right)^{1/2} v_{b_2} v_{b_1}}{c} .$$

(15)

In this equation, v_{b1} is the speed of the slow beam from the low-voltage gun and v_{b2} is the speed of the fast beam from the high-voltage gun. Note that this tuning condition is applicable only to weak beams ($n_b/n_e < 10^{-4}$). In the strong-beam case (strong-turbulence regime), a broad spectrum of EPW wave numbers can be generated, and the velocity requirements in Eq. (15) can be relaxed. Note also that for high-order TM modes with large $\omega_c \sim 3^{1/2}\omega_p$, Eq. (13) requires that the two beam speeds be closely matched.

The dispersion relations described by Eqs. (2), (3), (11), (12), and (13) are plotted in Figure 2. The plot shows how two oppositely directed EPWs with different phase velocities (ω_p/k_{e1} and ω_p/k_{e2}) are coupled to a third space-charge wave with dispersion

$$\omega = \frac{2\omega_p}{k_{e_1} - k_{e_2}} k \quad .$$

(16)

A plasma-loaded-waveguide mode is excited at the intersection of this coupled space-charge wave with the electromagnetic dispersion curve.

As an example of a solution to Eq. (15), consider an experiment with a 3.81-cm-diameter waveguide operating in V-band at $\nu_0=50$ GHz. The plasma frequency ν_p will be 25 GHz, so Eq. (4) indicates that the waveguide plasma density must be 7.8×10^{12} cm^{-3}. The cutoff frequency ν_c of the TM_{01} mode in the waveguide in vacuum is 6 GHz. If the energy of the fast electron beam is chosen at 60 kV, then the slow-beam energy must be 18 kV in order to satisfy Eq. (15). However, if a higher-order TM_{nm} mode is excited with $\nu_c\sim43$ GHz, Eq. (15) requires that the beam energies be equal.

2.2 EXPERIMENTAL CONFIGURATION

Millimeter-wave generation via plasma three-wave mixing is being investigated using the beam-plasma-waveguide system shown in Figure 1. Two electron beams are counterinjected into a plasma-loaded circular waveguide, where they generate EPWs. The counterstreaming EPWs nonlinearly couple via the three-wave-mixing mechanism to generate a TM waveguide mode, which then propagates down the guide in the direction of the slower beam (as a consequence of momentum conservation). Consistent with energy conservation, the radiation frequency is centered at twice the plasma frequency. The plasma and beam parameters are listed in Table 1.

11
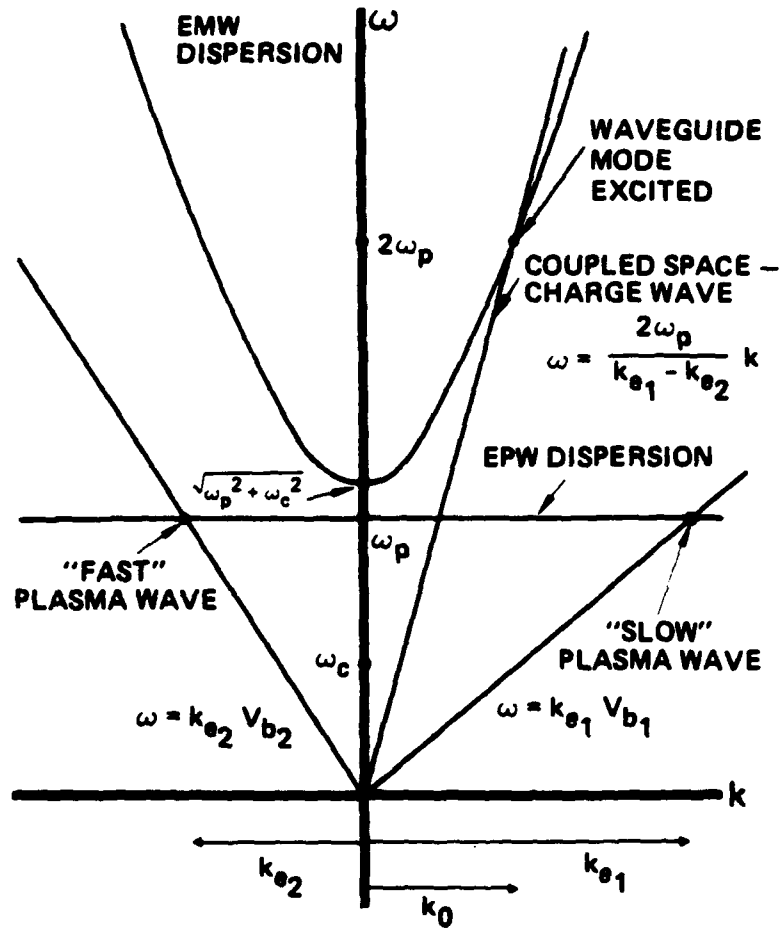
Figure 2. Dispersion relations for plasma three-wave mixing.

Table 1. Experiment Parameters.

- **GAS** : H_2, He, Ne, Ar, Kr, or Xe at 1 TO 45 mtorr
  typically He at 24 mtorr

- **PLASMA** : $n_e = 2 \times 10^{11}$ cm^{-3} to 10^{13} cm^{-3}
  $T_e \simeq 5$ eV

- **BEAMS** : $V_B \leqslant 90$ kV, typically 20-50 kV
  $I_B \leqslant 3.5$ A
  $T_B \geqslant 15$ eV
  $J_B \leqslant 4$ A/cm^2
  $n_B \leqslant 6 \times 10^9$ cm^{-3}, $0.03\% \leqslant n_B/n_e \leqslant 3\%$

- **WAVEGUIDE** : 3.8-cm diameter
  15-cm, 1.9-cm long

- **RADIATION** : 7-60 GHz, peak power $\leqslant 8$ kW

Figure 3 is a diagram of the experimental apparatus assembled for our investigation. High-density plasma ($\leq 1 \times 10^{13}$ cm^{-3}) is generated by a multiwire, wire-anode discharge[11-13] in the annular space surrounding a 3.8-cm-diameter perforated waveguide at helium-gas pressure in the 10-to- 65-mTorr range. The microperforations allow both ionizing discharge electrons and background plasma to penetrate the waveguide, thus loading it with a high-density, quiescent plasma. The perforations are large compared with a Debye length, but small compared with the electromagnetic wavelength; therefore, radiation remains trapped in the guide while plasma can pass through freely. Both ends of the circular waveguide are terminated by highly transparent grids (80%). Radiation is coupled out of this waveguide-cavity configuration through rectangular waveguides that are oriented to align the electric-field vector of the $TE_{1\theta}$ (rectangular-waveguide) mode with the axial electric field of a TM mode in the circular waveguide.

Secondary-emission electron guns[14,15] are used to generate the electron beams. As shown in Figure 3, each gun employs a separate wire-anode discharge in the region between the waveguide and the electron-gun cathode. The plasma in this discharge is partially confined between the waveguide-terminating grid on one side and a similar grid on the opposite side near the cathode. This latter grid also serves as the anode for the electron gun. A fraction of the ions produced in this plasma are extracted through the anode grid and are accelerated to the cathode (which is continuously held at negative high voltage) where they bombard the molybdenum electrode surface and produce secondary electrons. These electrons are accelerated back through the cathode-anode gap, forming a high-energy beam. The beam then passes through the anode grid and the waveguide-terminating grid and is injected into the waveguide with low (~36%) loss to the grid structures The beam then propagates through the plasma-filled waveguide
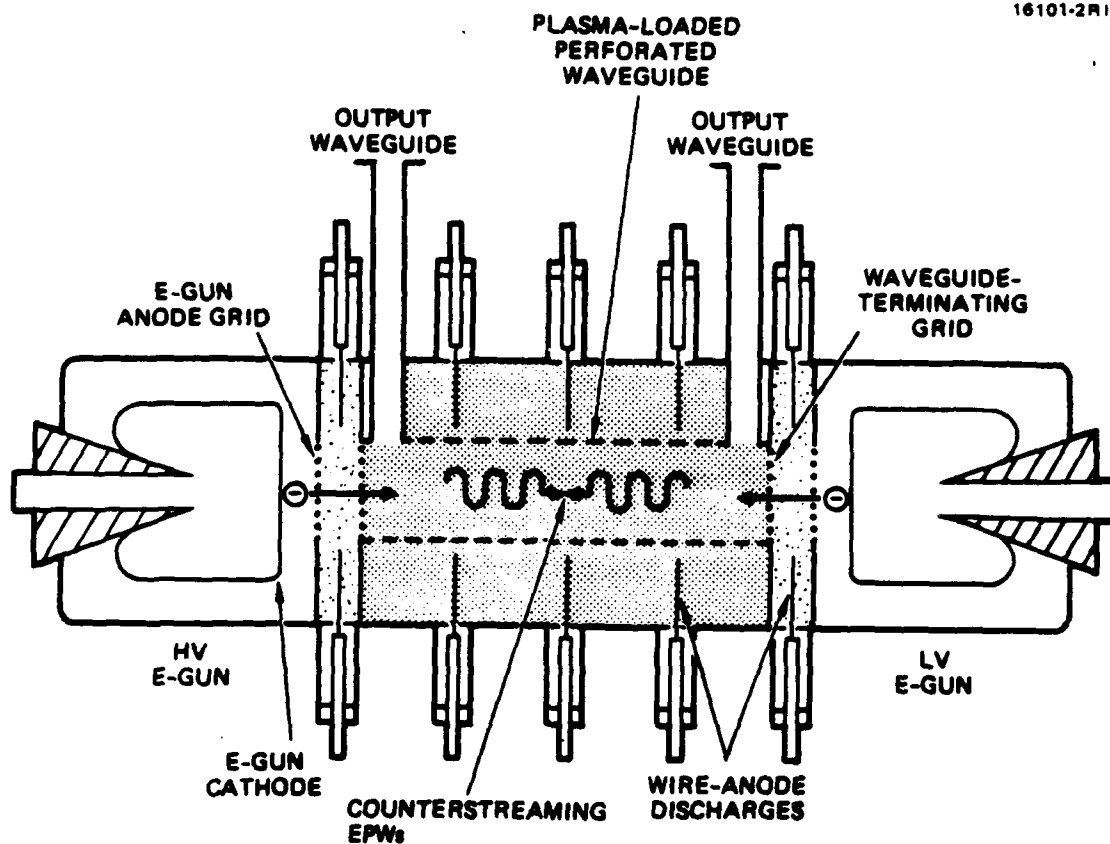
Figure 3. Experimental beam-plasma apparatus.

where ion charge in the plasma neutralizes the electron space charge in the beam. This "ion-focusing" effect allows the beams to propagate without having to use magnetic-focusing fields.

The utility of the secondary-emission gun is based on the high secondary-emission yield γ_s, which is obtained when high-energy ions strike gas-covered cathode-electrode materials. For example, γ_s varies from 5 to 15 when helium ions in the 35-to-150-kV range strike a molybdenum cathode in the presence of 20 mTorr of helium gas.[16]

The electron-beam current is controlled at low voltage by modulating the ($\leq$1-kV) wire-anode discharge at the ground-potential environment of the anode electrode. Because the plasma is confined within the gridded-anode structure (plasma electrons are unable to overcome the ~1-kV discharge-cathode drop to penetrate the gridded structure for ion current densities up to some limit), plasma closure of the high-voltage gap cannot occur and long-pulse (>>1 μs) operation is achieved. Modulation of the plasma source modulates the ion flux incident upon the cathode, which in turn controls the beam current. A mono-energetic beam is obtained throughout the beam pulse because the electron-beam is switched ON and OFF by the plasma source and not by the high-voltage supply for the cathode. Low-energy electrons produced from the rise and fall of the cathode voltage in conventional pulsed beams are not present. All this is accomplished without heater power and without high-vacuum-environment requirements, because the metallic cathode used in the secondary-emission gun cannot be poisoned.

The experiment is typically operated with 10- to 25-μs-wide flat-top pulses at a pulse-repetition frequency of 1 Hz. Circuits used to generate the plasma-discharge and beam pulses are shown in Figure 4. A 25-μs pulse-forming network (PFN) is employed to drive current pulses up to 800 A in the main waveguide-plasma-discharge section. A higher-impedance 18-μs PFN drives the wire-anode discharge in the low-voltage electron gun
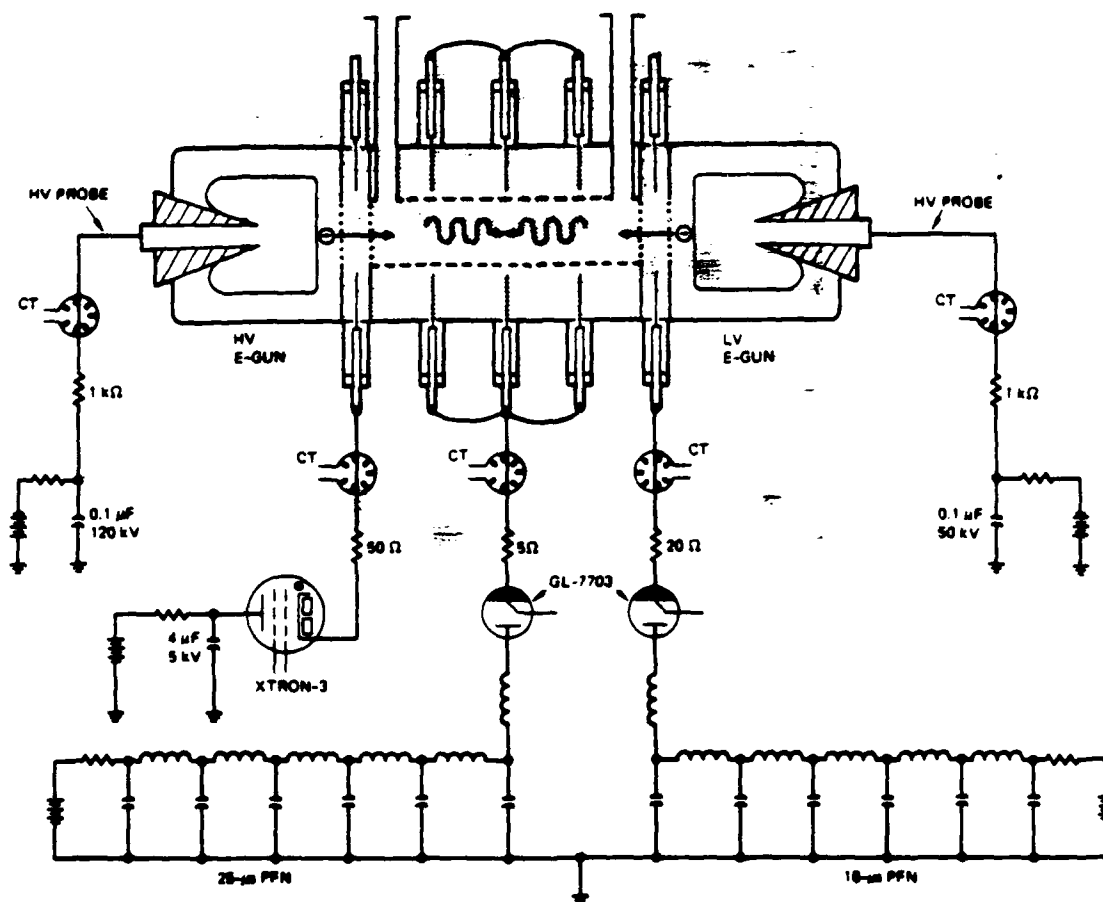
16

Figure 4. Schematic of plasma-discharge and electron-beam pulsed-power circuits.

(LV E-gun). GL-7703 ignitrons are used as closing switches to discharge both PFNs. The wire-anode discharge in the high-voltage (HV) E-gun is modulated by a circuit consisting of a capacitor and a XTRON-3 CROSSATRON^R Modulator Switch (CMS).[17,18] The Hughes CMS is an advanced thyratron-like device that both closes and opens under grid control, so square-wave pulses can be obtained in hard-tube-modulator fashion without having to use a fixed-pulse-length PFN. The E-gun wire-anode current pulses are typically 10 to 100 A. Finally, capacitors are used to continuously maintain high voltage on the E-gun cathodes through 1-kΩ current-limiting resistors. The HV E-gun is designed to operate up to 120 kV, and the LV E-gun up to 50 kV.

Each of the five circuits shown in Figure 4 is instrumented with high-voltage probes and Pearson current transformers (CT). These diagnostics, as well as the Langmuir probes, are interfaced to an 11-channel IBM-PC/AT-based data-acquisition system and oscilloscope array, which are housed within an RFI-screen room. The output waveguides are also fed into the screen room where the radiation is analyzed by a network of millimeter-wave detectors, filters, attenuators, and mixers. Figure 5 is a schematic drawing of the millimeter-wave detection system. The bandwidth of the storage oscilloscopes is 100 MHz and the maximum sampling rate of the analog-to-digital converters in the computer is 1 GHz.
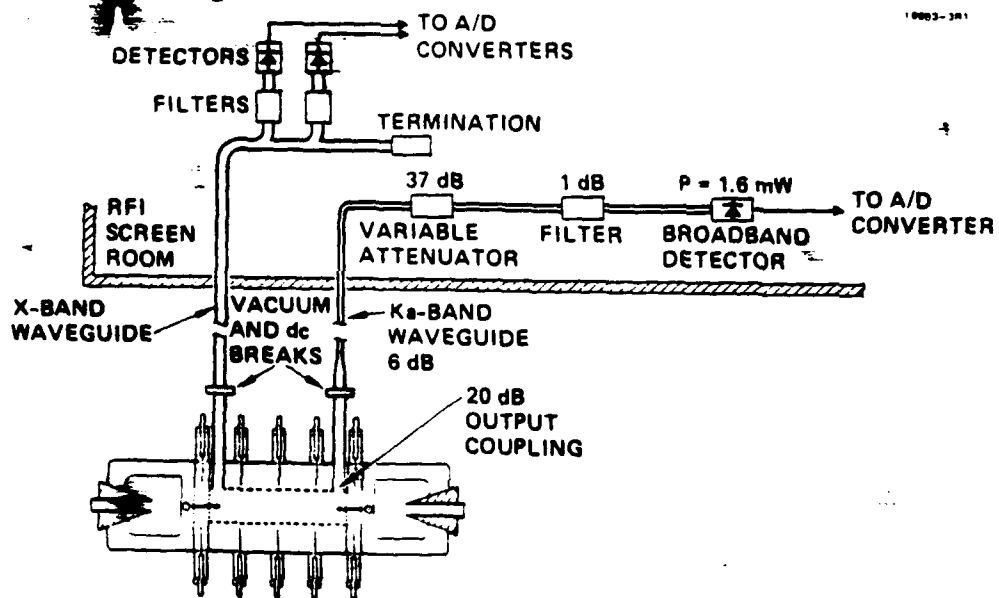
Figure 5.   Millimeter-wave diagnostics and power measurement system.

SECTION 3

RESEARCH PROGRESS

In the following section we review our significant technical progress in understanding and demonstrating the basic physics of millimeter-wave generation via plasma three-wave mixing. We describe our recent experiments investigating radiation modulation dependence on beam and waveguide plasma parameters, observation of cavity modes in a short 1.5-cm-long waveguide cavity, and attempts to increase the beam current to reach saturation of the three-wave mixing process.

Appendix A contains a preliminary draft of a paper we are preparing for publication in collaboration with Drs. N. Krall and M. Rosenberg. The paper includes a summary of the research performed during past years under this program.

3.1 RADIATION MODULATION CHARACTERISTICS IN 15-cm-LONG CAVITY

The radiation produced by the three-wave mixing process is strongly amplitude modulated. In the experiments described in this section, we found that the modulation depends on the beam current and the waveguide plasma density, and is also correlated with the local electrostatic oscillations in the plasma.

Experiments performed during past years under this program established that the output power is strongly modulated on a time scale that is near the ion-plasma frequency — behavior that is also characteristic of nonlinear beam-plasma instabilities. Figure 6 shows that the radiation at 35 GHz is actually emitted in random spikes with half-widths of ~10 ns. The spikes could be even narrower because the bandwidth limit of the oscilloscope was 100 MHz. Using the beam-plasma parameters listed in Figure 6, together with Eq. (8), we estimate the ratio of EPW energy density to plasma energy density, $W_{EPW}/n_e T_e$, to be about 7×10^{-2}. The beam-plasma interaction in the experiment is strongly turbulent, because this ratio exceeds the weak turbulence parameter $(k_e \lambda_D)^2$ by 3 orders of magnitude.
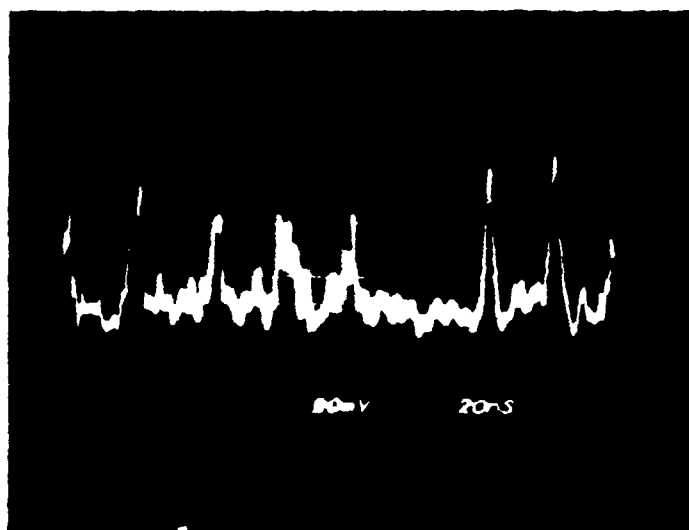
35-GHz
RADIATION

TIME, 40 ns/div

n_e $= 3.8 \times 10^{12} \, cm^{-3}$

T_e $= 5 \, eV$

I_b $= 2.5 \, A$

V_b $= 30 \, kV$

$\dfrac{n_b}{n_e}$ $\cong 2.3 \times 10^{-4}$

$\dfrac{W_{EPW}}{n_e T_e}$ $\cong 7 \times 10^{-2}$

$(k_e \lambda_D)^2 \cong 8 \times 10^{-5}$

Figure 6.   Output mm-wave radiation is strongly
modulated on a time scale that is near
the ion-plasma frequency.   Experiment
parameters corresponding to the observed
35-GHz radiation are listed below the
oscilloscope waveform.

22

The millimeter-wave modulation frequency decreases as the ion mass is increased. Oscilloscope photos of the crystal detector output for five different gases (i.e., hydrogen, helium, argon, krypton, and xenon) are shown in Figure 7. These data are reduced to a quantitative form in Figure 8, where the modulation inter-pulse period (IPP) and pulse width are plotted versus ion mass. The parameters scale approximately with the square root of the ion mass. These data clearly indicate that ion dynamics is important in determining the characteristics of the millimeter-wave radiation. The modulation could be caused by ion acoustic waves, which are known to be generated by parametric-decay instabilities in strong-EPW-turbulent systems.

3.1.1 Scaling With Waveguide Plasma Density

The radiation modulation changes from a nearly continuous emission process at low discharge current, to a more ordered, burst emission at high discharge current. Figure 9 shows the change in the modulation of 36-GHz radiation (filter pass-band = 35 to 37 GHz) as the waveguide plasma density is increased. At 230 A, the radiation consists of many very narrow-width (5 to 25 ns wide) spikes with a short inter-pulse period of about 10 to 50 ns. The radiation is emitted continuously and we do not observe periods when the radiation power drops to zero. However, when the discharge current is increased to 310 A, the bursts become wider (50 to 100 ns), the IPP increases to 100 to 200 ns, and the signal amplitude between bursts is low compared with the peak amplitude.

These characteristics are also exhibited at higher discharge currents. Figure 10 compares the Ka-band emission measured with waveguide discharge currents equal to 500 and 200 A. At 500 A, the emission is distributed in a series of bursts, and the signal amplitude between bursts is very low. When the discharge current is reduced to 200 A, the radiation power drops by about 14 dB and the bursts are replaced by narrow, high-frequency pulses. We
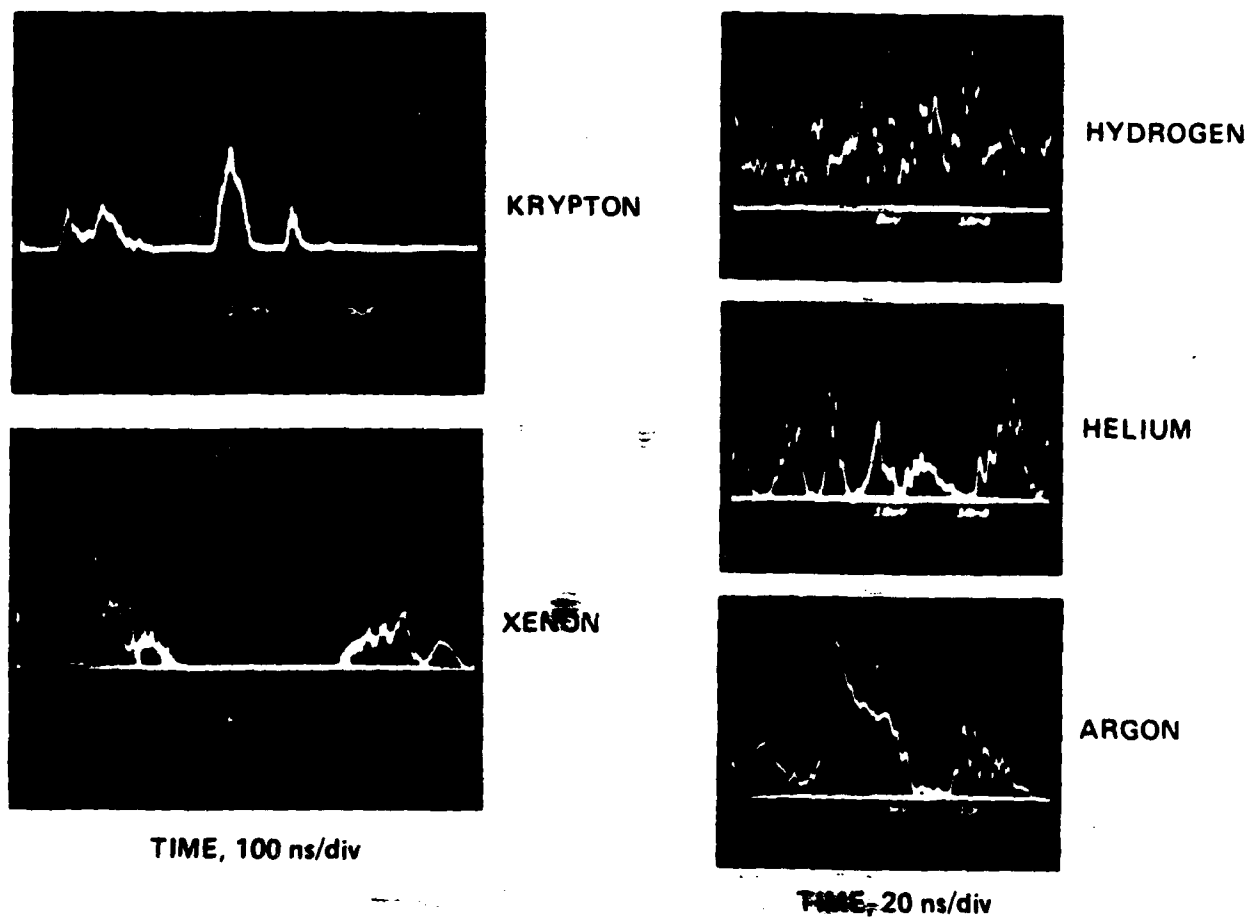
Figure 7. Millimeter-wave modulation frequency decreases with ion mass.
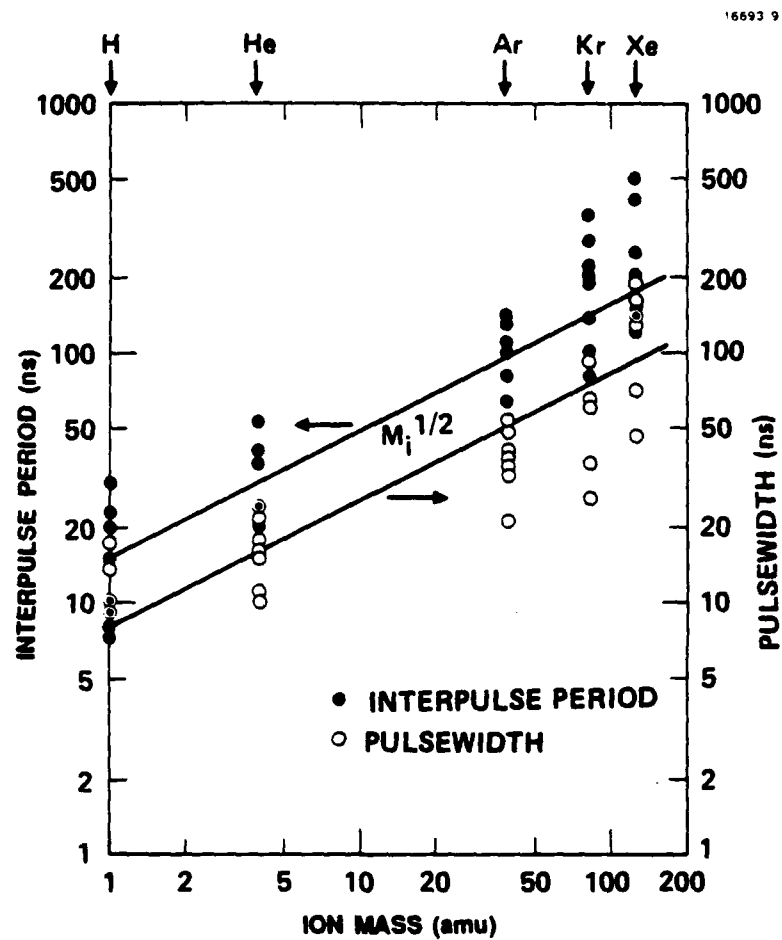
Figure 8.   Millimeter-wave pulsewidth and interpulse-period scale as $M_i^{1/2}$.

$I_D = 310\ A$

Ka-BAND
RADIATION

10 mV/div

TIME (200 ns/div)

$I_D = 230\ A$

Ka-BAND
RADIATION

10 mV/div

TIME (200 ns/div)
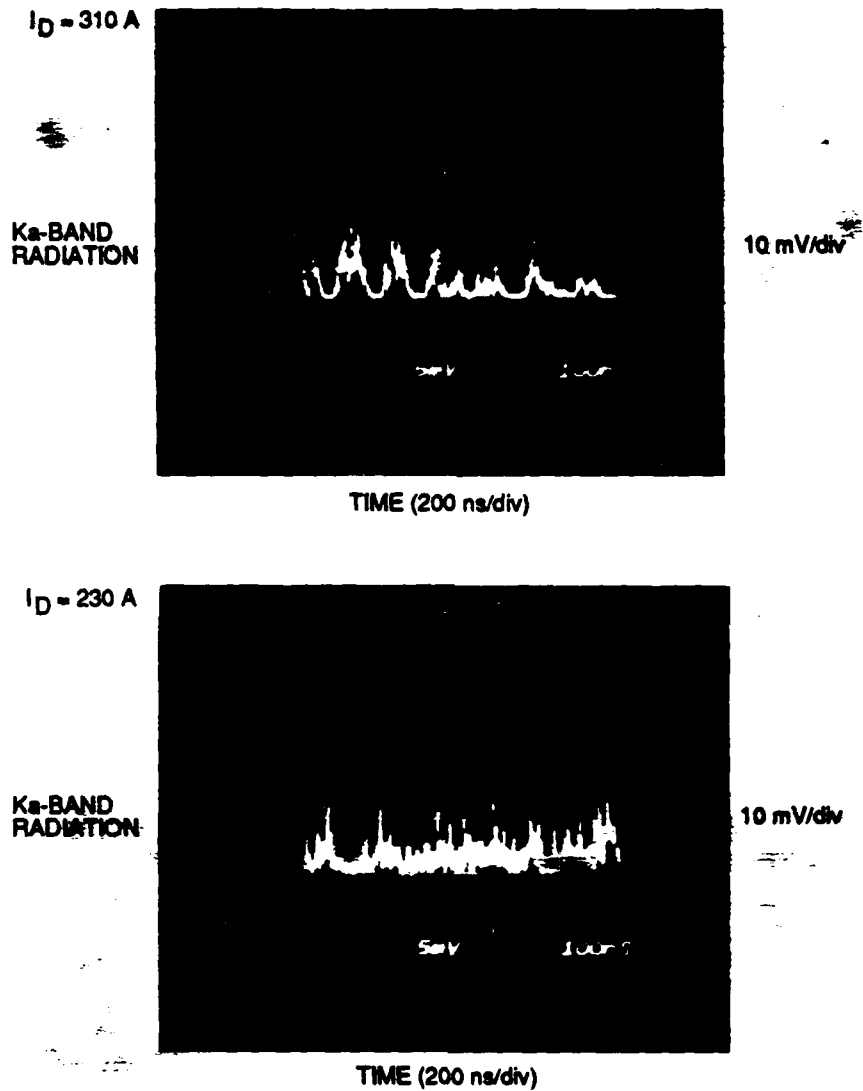
Figure 9. The modulation of Ka-band radiation is
dependent on the waveguide discharge
current. The total beam current was
5 A and the beam voltage was 30 kV.

18208-3

$I_D = 500$ A   ATTENUATOR = 22 dB

TIMING
PULSE

Ka-BAND
RADIATION   10 mV/div

TIME (1 µs/div)

$I_D = 500$ A   ATTENUATOR = 22 dB

TIMING
PULSE

Ka-BAND
RADIATION   10 mV/div

TIME (100 ns/div)

$I_D = 200$ A   ATTENUATOR = 8 dB

Ka-BAND
RADIATION   10 mV/div

TIME (100 ns/div)

Figure 10. The Ka-band radiation is strongly modulated for
a waveguide discharge current of 500 A. When the
discharge current is reduced to 200 A, the
radiation burst width becomes very narrow. The
total beam current was 5 A and the beam voltage
was 30 kV.

27

believe that the frequency of mm-wave spikes at lower discharge current is increased because the background plasma density is lower and the parameter ϵ in Equation (1) is higher. This will increase the growth rate of the EPWs and enhance the rate of energy transfer from the beam to the radiation field. However, since the plasma density is lower, there are fewer particles available for energy transfer and the net peak-power transfered is lower.

3.1.2 Scaling With Beam Current

As shown in Figure 11, the modulation IPP also depends on beam current. For this experiment the HV beam current ($I_B{}^{HV}$) was held constant at 2.6 A while the LV beam current was varied. At $I_B{}^{LV}$ = 2.5 A, the emission consists of 50-ns-wide bursts and the IPP is 50 to 2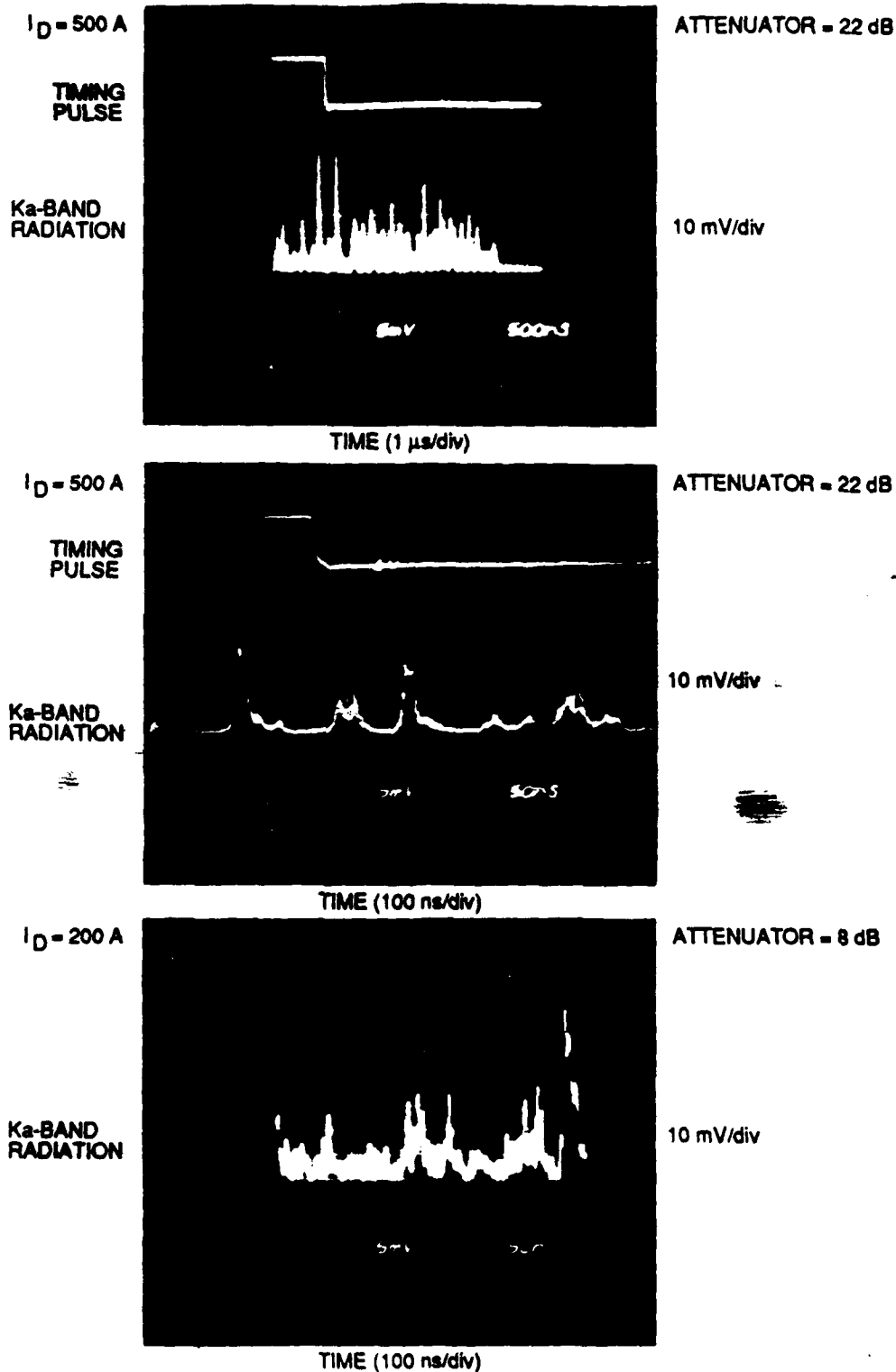00 ns. When $I_B{}^{LV}$ is reduced to 1.8 A, the radiation drops in power by about 15 dB (as predicted by the scaling of radiation power with beam current performed during 1986), and is generated in burst clusters with an IPP of 800 ns to 1 μs; very little power is emitted between bursts. This trend continues even when $I_B{}^{LV}$ is set to zero. However, voltage is still applied to the LV beam cathode, and radiation is still observed, but the IPP is now longer than 2 μs. Radiation is produced in this case because some of the HV beam electrons reach the LV cathode and are reflected into the waveguide plasma. The reflected electrons then excite EPWs, resulting in radiation emission. When the LV beam cathode is grounded so that the HV beam electrons traverse the waveguide plasma only one time, radiation is not detected.

The change in modulation IPP and burst width with beam current may also be related to the EPW growth rate. At lower beam current the ϵ parameter is lower and the EPW growth rate is reduced, leading to a lower rate of conversion of beam energy to mm-waves.

28

$I_b^{LV} = 2.5\,A$ ATTENUATOR = 26 dB

Ka-BAND RADIATION   10 mV/div

TIME (400 ns/div)

$I_b^{LV} = 1.8\,A$ ATTENUATOR = 10 dB

Ka-BAND RADIATION   10 mV/div

TIME (400 ns/div)

$I_b^{LV} = 0$ ATTENUATOR = 5.5 dB

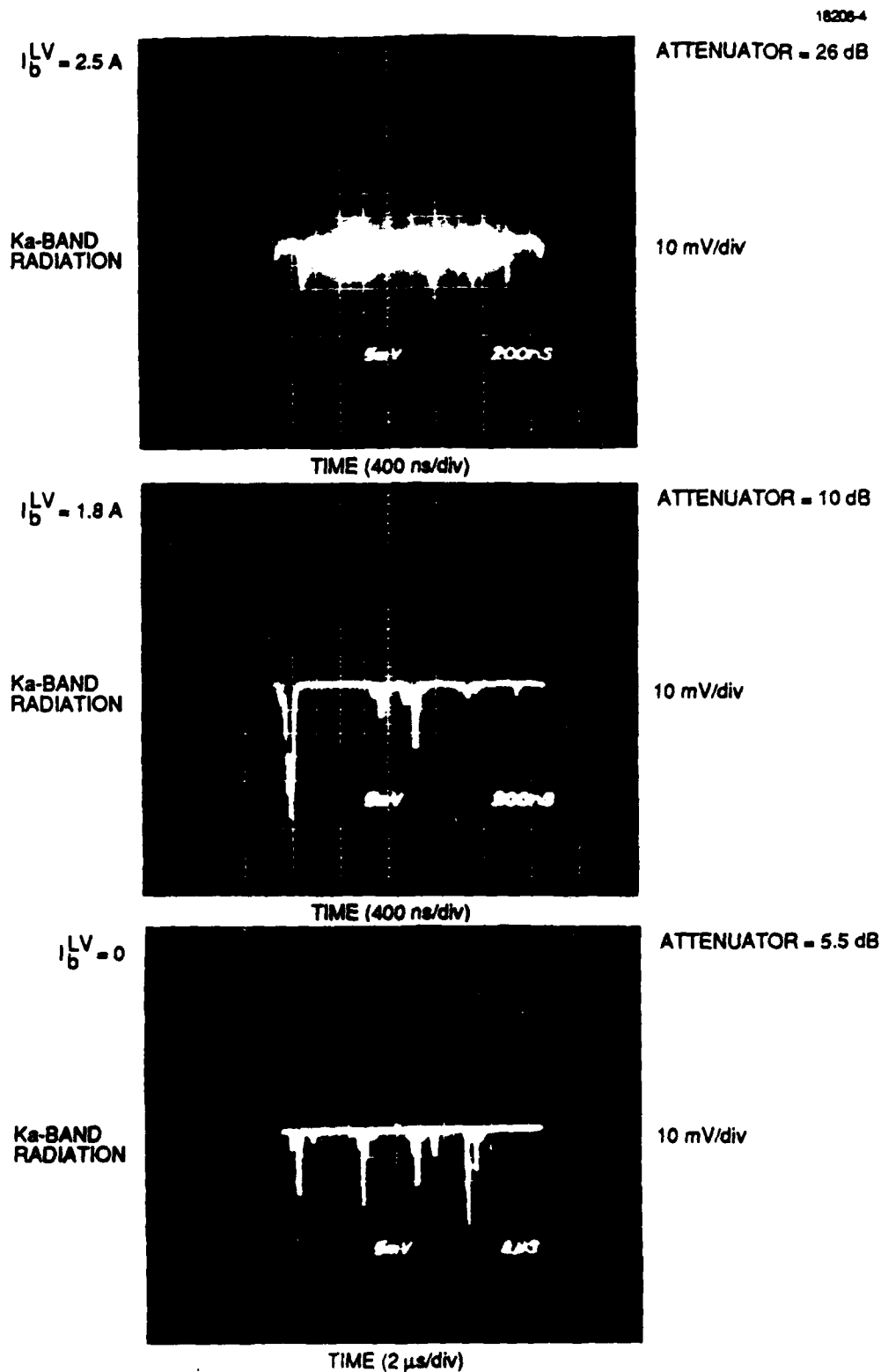Ka-BAND RADIATION   10 mV/div

TIME (2 µs/div)

Figure 11.   Ka-band modulation IPP depends on the beam current.
When $I_b^{LV} = 0$, but the LV cathode is biased to
reflect the HV beam electrons back into the plasma
radiation is still observed. The HV beam current
was held constant at 2.6 A, the beam voltage was
20 kV and the waveguide discharge current was 500 A.

29

3.1.8 Correlation With Electrostatic Probe

A disk probe was used to investigate the correlation of a high-frequency probe signal with the radiation coupled out of the waveguide cavity via the X-band waveguide port. The probe was located about 1 cm downstream of the beam injection grid shown in Figure 3 and was capacitively coupled into a 100-MHz-bandwidth oscilloscope.

The probe signal correlates well with the modulation of the 35-GHz radiation signal, as shown in Figure 12. The signals were recorded simultaneously using two oscilloscopes. The probe and radiation signals each have an IPP of about 200 ns. This is also shown in Figure 13, which displays the signals using a faster time scale. Figure 14 shows that when one of the beams is turned off, both the radiation signal falls to zero and the electrostatic (ES) probe signal is significantly reduced.

This preliminary investigation found that there is a direct correlation between the radiation and probe signals. The probe output, however, could be due to direct radiation pickup. Future experiments will utilize an array of specially-designed high-frequency radial ES probes to determine the spatial and temporal evolution of the ES oscillations so we can differentiate between direct radiation pickup and a propagating ES perturbation.

3.2 RADIATION MODULATION CHARACTERISTICS IN 1.9-cm-LONG CAVITY

Boundary conditions imposed by the waveguide cavity walls specify the allowed ES and EM modes. The boundary conditions, together with the beam current and voltage, determine the allowed ES EPW modes within the system. We expect this effect to be most easily observed when the waveguide cavity dimensions are reduced to values on the order of the EPW wavelength. To investigate the radiation scaling with cavity length, we replaced the 15-cm-long waveguide cavity with a 1.9-cm-long system. The short cavity was fabricated using the same type of perforated sheet used in the 15-cm cavity. A single Ka-band waveguide output was used to couple the radiation out of the cavity.

35-GHz RADIATION   **DISK PROBE SIGNAL**
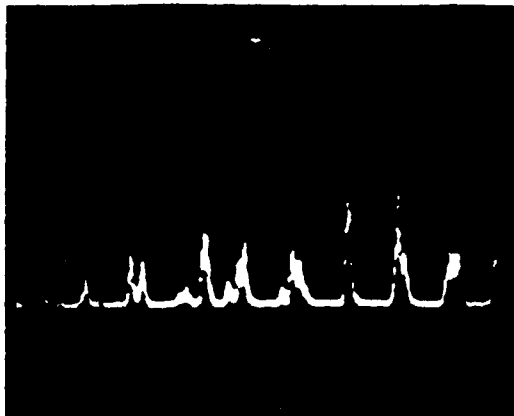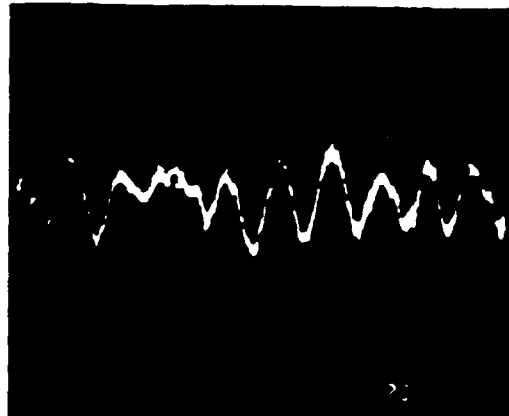
TIME, 200 ns/div   **TIME, 200 ns/div**

Figure 12.   Electrostatic fluctuations have the same
             frequency components as the output radiation.
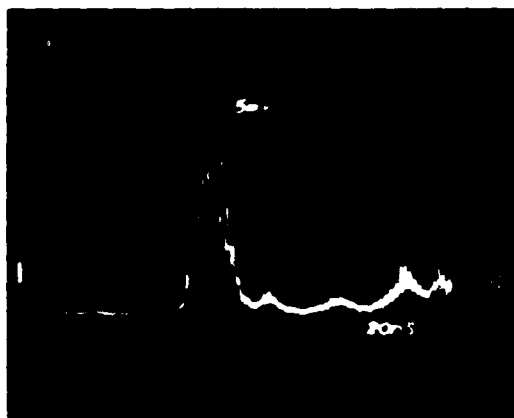
35-GHz RADIATION   **DISK PROBE SIGNAL**

TIME, 40 ns/div   **TIME, 40 ns/div**

Figure 13.   The radiation and the disk probe signal
             are compared using a faster oscilloscope
             time scale.

31

35 GHz RADIATION　　　　　　**DISK PROBE SIGNAL**

TIME, 200 ns/div　　　　　　**TIME, 200 ns/div**

Figure 14.　When only one beam is injected into the
waveguide cavity, the radiation signal
drops to zero and the probe signal is
significantly reduced.

The output radiation from the 1.9-cm-long cavity is very similar to the radiation produced in the 15-cm-long device. The radiation is strongly amplitude modulated, scales with the beam voltage, and has a threshold of about 3 A of beam current. One major difference is that the radiation power is about 20 dB lower in the shorter system. This indicates that there is insufficient distance for the E-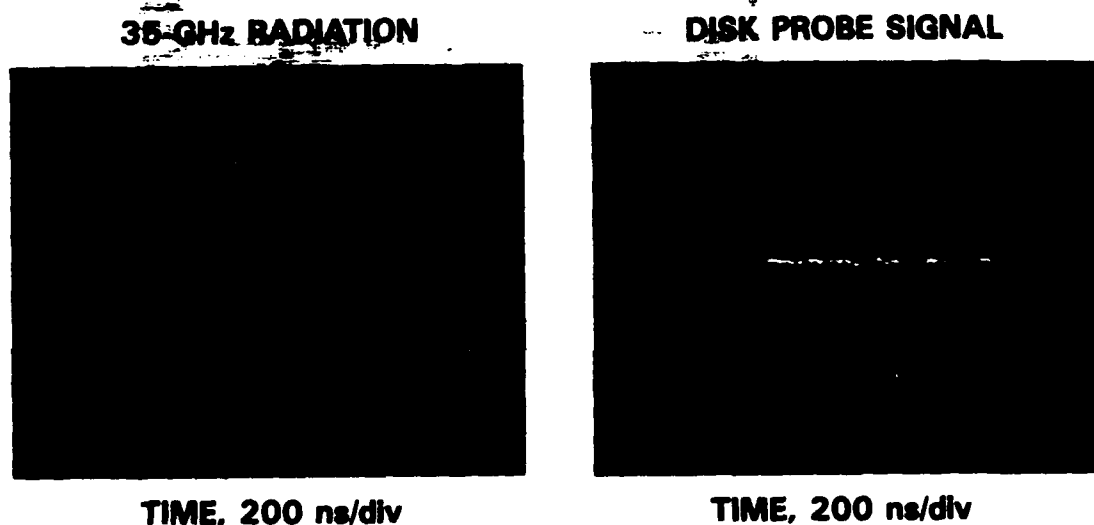beams to pinch and drive strong EPWs. For several experiments we used a gas mixture of 7% air and 93% He gas to improve the discharge stability in the small system.

3.2.1 Theoretical Discussion Of Cavity Modes

Consider a cylindrical cavity with walls fabricated from a highly transparent metal grid as shown in Figure 15. For our experimental conditions, the EPW wavelength is large compared with the grid aperture size so that we can treat the cavity walls as conducting boundaries. This boundary condition requires that the EPW electric fields vanish at the walls, and leads directly[19] to the quantization condition that $\lambda_z = 2L/n$, where L is the length of the waveguide cavity, and n is the integral number of half-wavelengths within the cavity, n = 1,2,3,$\cdots$. This can also be expressed in terms of the z-component of the EPW wavenumber, $k_z = n\pi/L$.

The requirement that the EPW be resonant with the beam as expressed by Eq. (2) places another constraint on the system. Combining Eq. (2) with the EPW quantization condition yields

$$v_{b,n} = \omega_e L/n\pi \qquad . \qquad (17)$$

Rewriting this in terms of the beam energy E_b we obtain

$$E_{b,n} = (m/2) \times (\omega_e L/n\pi)^2 \qquad . \qquad (18)$$

Equation (18), which was derived by M. Rosenberg,[19] requires that for fixed plasma density and device length, only certain values

33

mm-WAVE OUTPUT
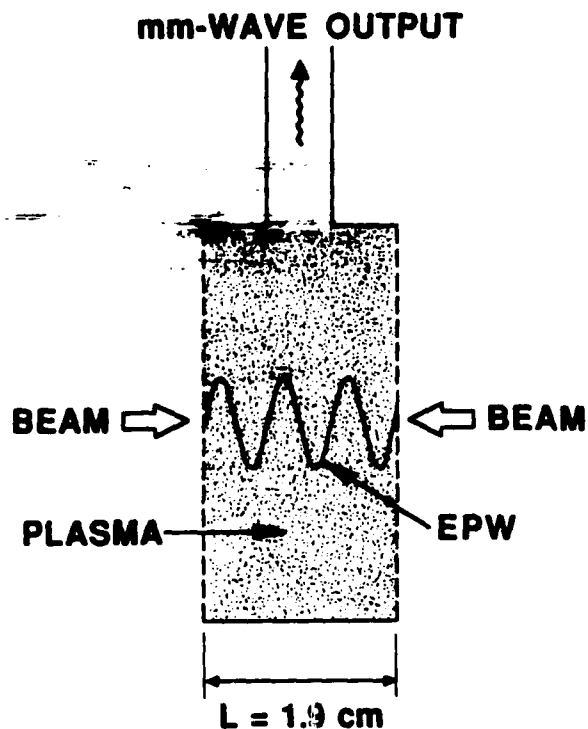
EPW QUANTIZATION: $k = \dfrac{n\pi}{L}$

DISPERSION: $\omega_p = k v_b$

ALLOWABLE MODES: $v_b = \dfrac{\omega_p L}{n\pi}$

BEAM ⇨   ⇦ BEAM

PLASMA →   EPW

$L = 1.9$ cm

Figure 15.   The allowed EPW modes are determined
by the quantization condition and the
dispersion relation.

of beam energy can excite the allowed EPW modes. Table 2 lists the mode numbers and corresponding beam energies for 15-cm- and 1.9-cm-long waveguide cavities. The modes are very closely spaced in beam energy in the 15-cm system, making it very difficult to experimentally differentiate between them. Also, because the EPW have a longer path length to grow and saturate in the 15-cm system, the spread of wavenumbers is larger and k_z approaches a continuum. However, the shorter system requires smaller mode numbers and the energy spacing between modes is larger.

TABLE 2. Waveguide Cavity Mode Numbers.

	Mode number	Beam energy kV
15-cm-long cavity		
	30	64.3
	31	60.2
	32	56.5
	33	53.1
	34	50.1
	35	47.2
	36	44.7
	37	42.3
	38	40.1
	39	38.1
	40	36.2
	41	34.4
	42	32.8
	43	31.3
	44	29.9
	45	28.6
	46	27.4
	47	26.2
	48	25.1
	49	24.1
	50	23.2
1.9-cm-long cavity		
	4	58.0
	5	37.1
	6	25.8
	7	19.0
	8	14.5

8.2.2 Power Scaling With Beam Voltage

Figure 16 shows the voltage-tuning curve for the 1.9-cm-long waveguide cavity. To reduce the effects of shot-to-shot power variations, and power variations within a single pulse, we used an RC circuit to integrate the total power in each shot, and this number was then averaged over ten successive shots using the computer. Three distinct peaks are now observed rather than the previously noted broad peaks for the 15-cm-long waveguide cavity (see Appendix A). The three peaks correspond to the n = 6, 7, and 8 modes listed in Table 2. The agreement of the physical model and the experimental results is excellent.

This experiment demonstrates that the boundary conditions imposed on the EPWs by the waveguide cavity determine the EPW modes that can be excited by the beam. This type of mode structure was not observed in the previous experiments using the 15-cm-long cavity because the modes for that system are so closely spaced. As shown in Figure 16, the 2 to 5 kV emission linewidth is sufficient to mask the presence of closely spaced modes. Another contributing factor is that the 15-cm-long cavity is many wavelengths long, as evidenced by the high mode numbers, whereas the short cavity is only a few wavelengths in length. Boundary effects are expected to be more important for the short chamber, while the longer chamber approaches a free-space simulation where the walls are well removed from the main plasma volume.

8.2.3 Modulation Envelope And Fourier Transform

The radiation emitted from the 1.9-cm-long cavity is strongly modulated with two distinctly different frequencies. Our approach to quantitatively analyze the signal was to record the crystal detector output using a fast digitizer operated at 1 GHz (effective bandwidth = 450 MHz). The digitized signal is displayed in Figure 17. The radiation bursts are now very
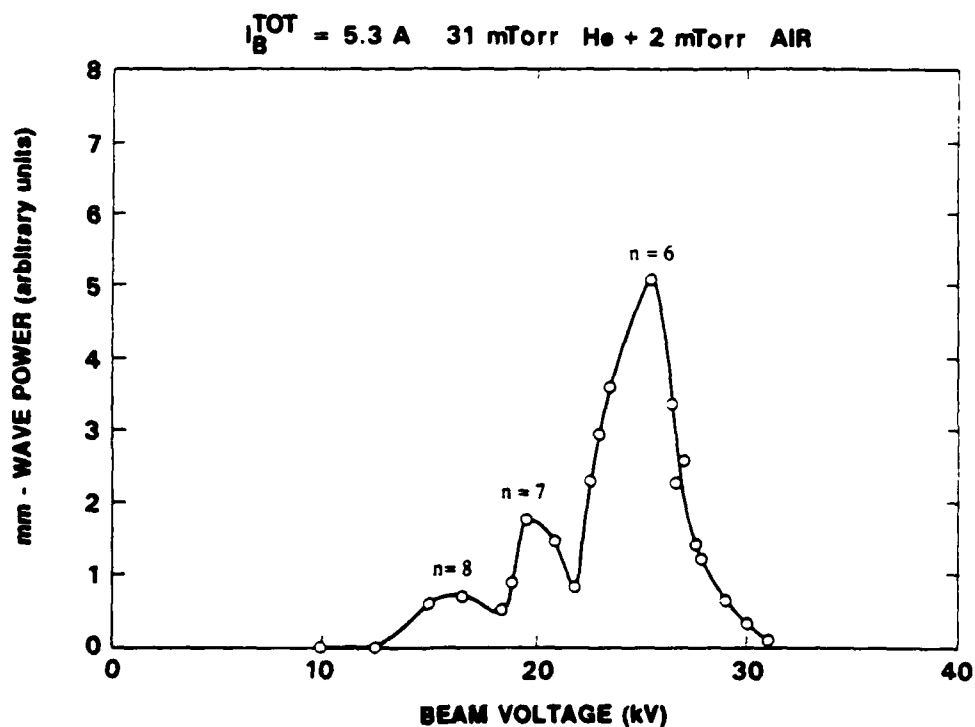
Figure 16. Radiation power scaling with beam voltage for 1.9-cm-long waveguide cavity reveals the EPW mode structure specified by the cavity longitudinal boundary conditions. Air was added to the He gas to improve the stability of the discharge.
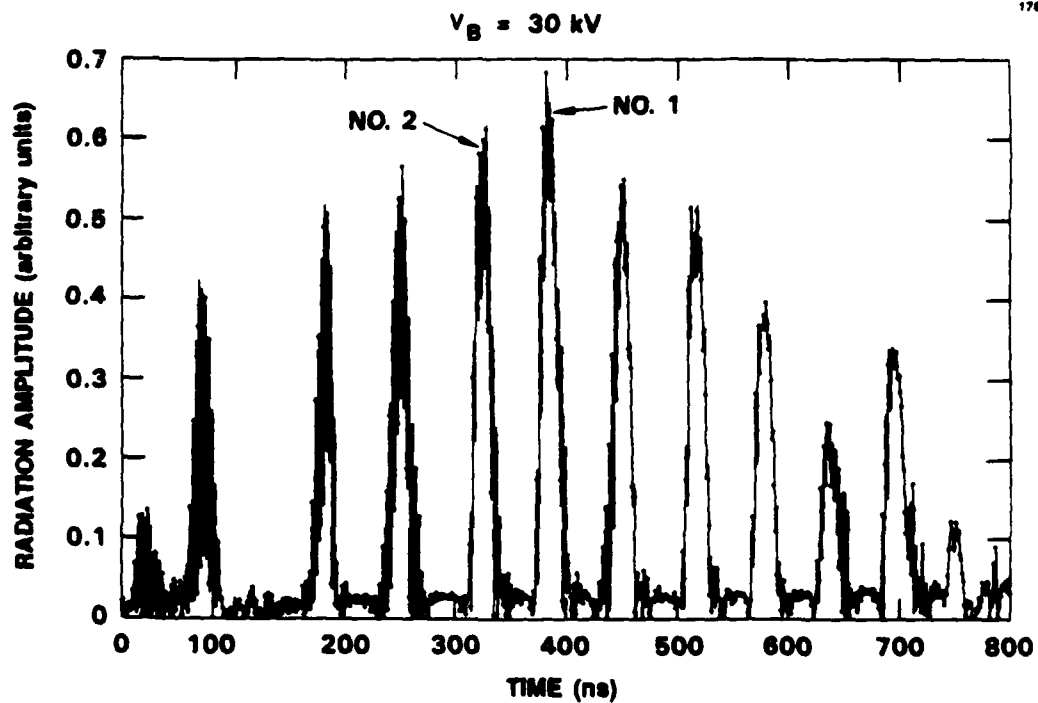
37

Figure 17. Radiation bursts are modulated at two different frequencies in the 1.9-cm-long waveguide cavity.

regularly spaced with a high-frequency modulation superimposed on the slower burst modulation. This is evident in Figures 18 and 19, which display two burst peaks from Figure 17 using an expanded time scale. The fast modulation depth can be a substantial fraction of the full burst amplitude, as shown in Figure 18.

The power spectrum for this data is obtained by calculating the Fast Fourier Transform using our Compaq 386/16 computer. The power spectrum is displayed on a log scale in Figure 20 and on a linear scale in Figure 21. The frequency of the slow modulation is about 14 MHz, with a second harmonic at about 28 MHz. The fast modulation peaks at 345, 356, and 371 MHz, as shown in Figure 22.

The 14 MHz modulation is controlled by the ion dynamics as described previously. The high frequency modulation near 350 MHz is a new feature that was first observed clearly in the 1.9-cm-long system. However, in contrast with the low frequency modulation, the high-frequency modulation is largely independent of the plasma and beam parameters. Subsequent experiments revealed that similar high-frequency radiation modulation is also observed using the 15-cm-long cavity. Next year we will perform scaling experiments to investigate the high frequency modulation in greater detail.

3.3 ATTEMPTS TO INCREASE BEAM CURRENT

The radiation power scaling with beam current measured previously demonstrated that up to the highest total beam current available, the radiation generation process had not saturated (see Appendix A). The saturation characteristics are an indicator of the physical processes that ultimately limit the radiation power and net conversion efficiency for the three-wave mixing process. In this section we describe several different approaches we used to increase the available beam current.
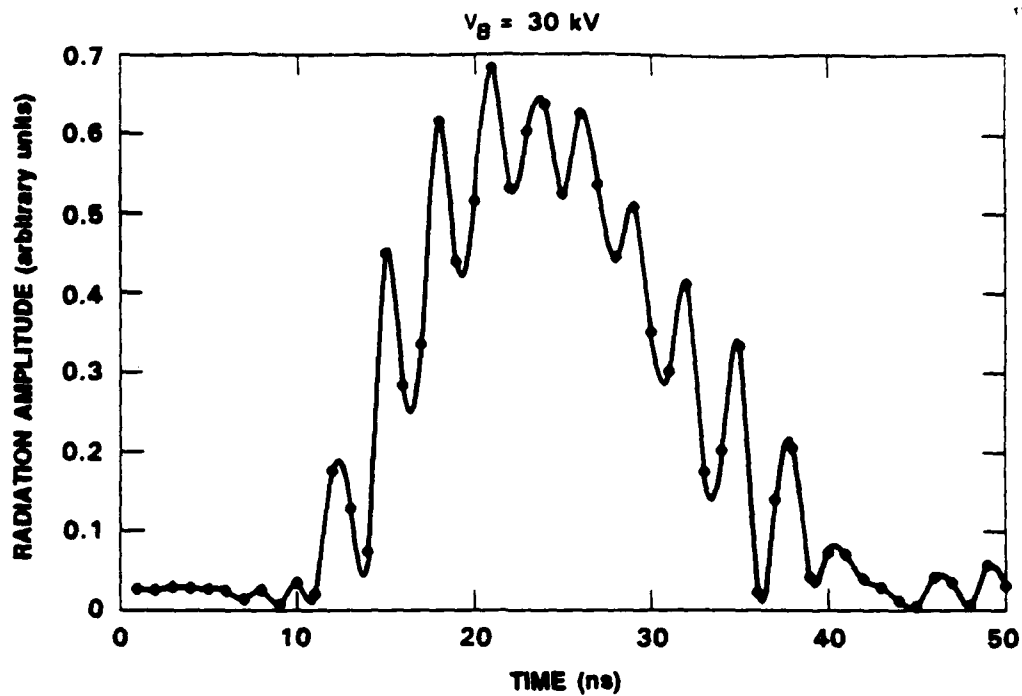
Figure 18. Peak number 1 from Figure 17 clearly shows the high- and low-frequency modulation components.
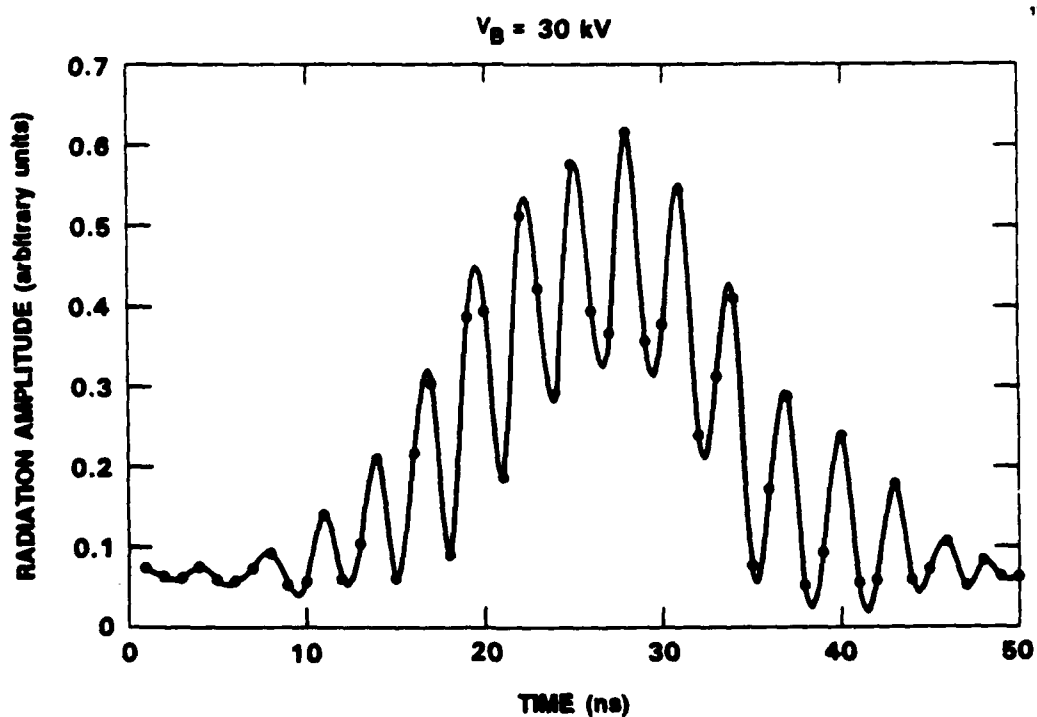
Figure 19. Peak number 2 from Figure 17.

V_B = 30 kV   35-GHz RADIATION

17847 11

Figure 20.   Two modulation frequency bands are evident
in the power spectrum calculated from data
shown in Figure 17.

V_B = 30 kV

17847-10

Figure 21.   Display of the radiation power spectrum
using a linear scale.

Figure 22. Display of high-frequency modulation
components using an expanded scale.

3.3.1 Reduce Beam HV Gap Spacing In 1.9-cm-Long System

The Child-Langmuir space-charge-limited current in a planar diode is

$$I = (4\epsilon_o/9)(2e/m)^{1/2}(V^{3/2}/d^2), \qquad\qquad (19)$$
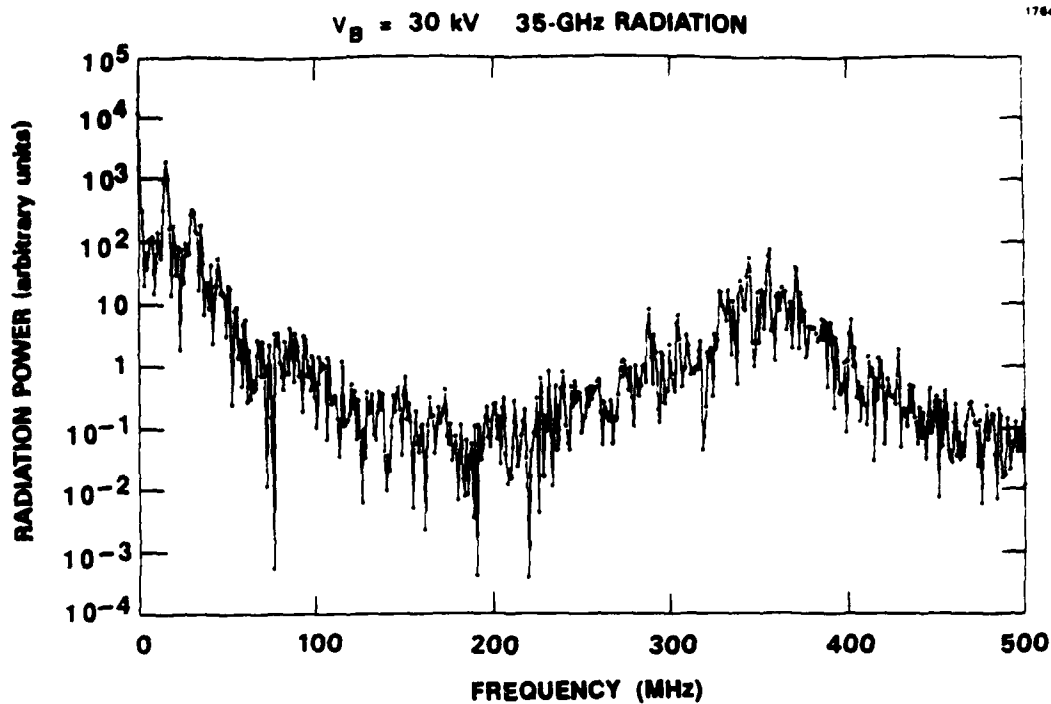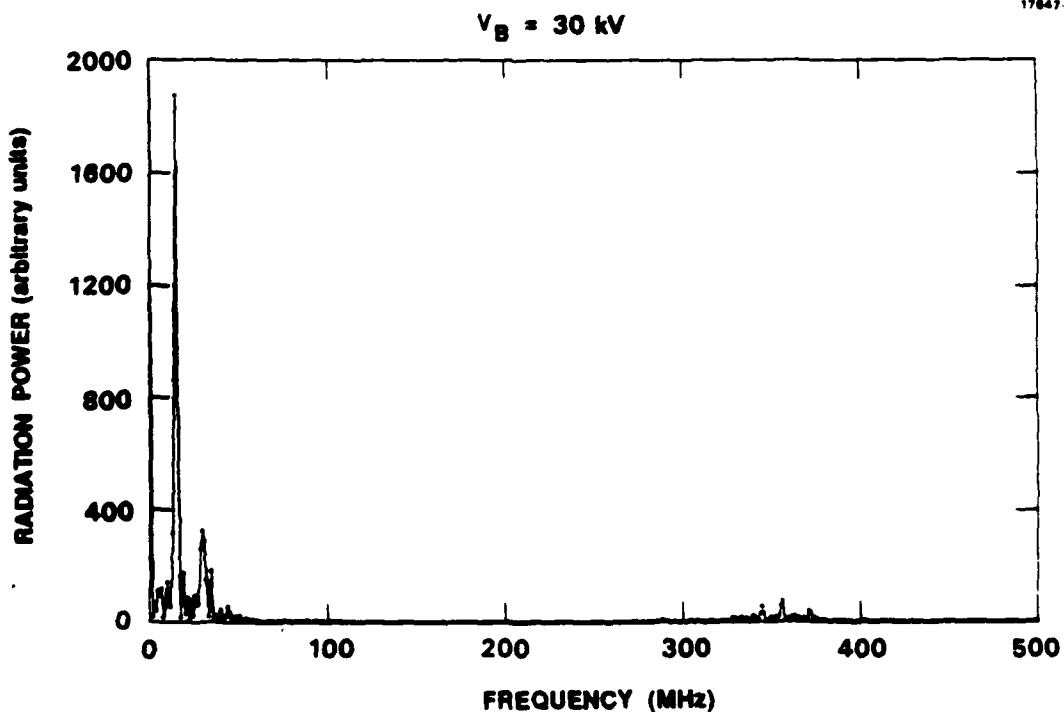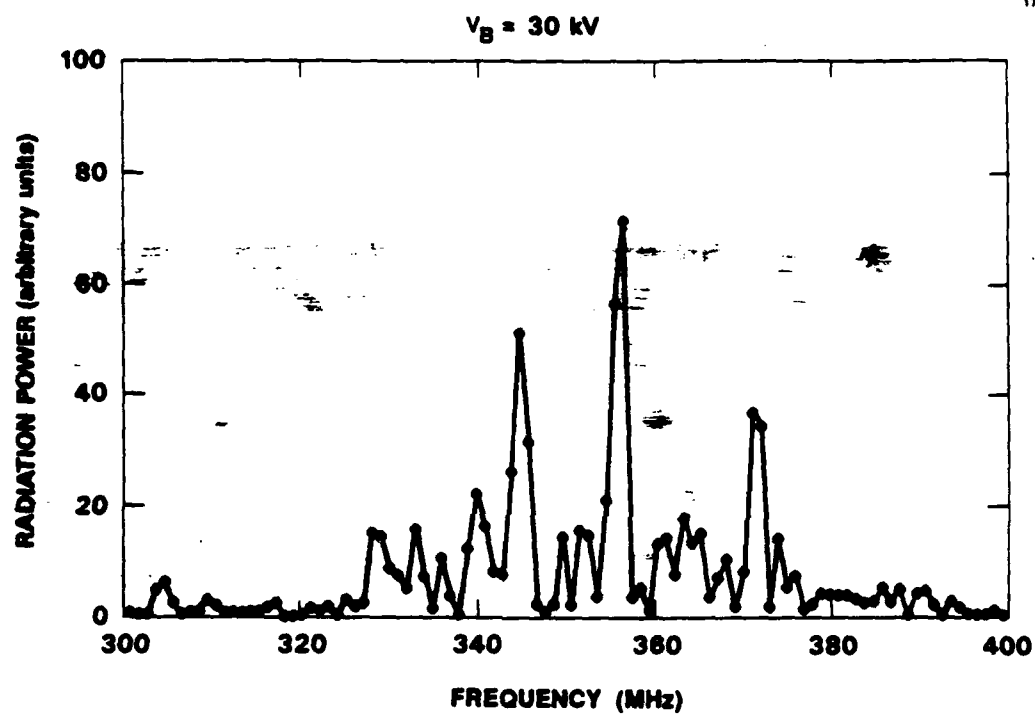
where V is the gap voltage in volts, d is the gap spacing, e/m is the charge-to-mass ratio, and ϵ_o is the permittivity of free space. Because the space-charge-limited current scales as $m^{-1/2}$, ion emission at the anode will become space-charge limited well before electron emission at the cathode. For singly charged helium ions, the space-charge-limited ion current is

$$J_i = 2.72\text{x}10^{-3}(V^{3/2}/d^2). \qquad\qquad (20)$$

One technique we used in an attempt to increase the space-charge-limited ion current, and consequently the E-beam current, was to decrease the gap spacing from 1.6 to 1 cm. The measured beam current scaling with beam discharge current is shown in Figure 23 for the 1.9-cm-long system with a 1-cm gap. This is compared with the scaling curve for the 15-cm-long device with a 1.6-cm-gap spacing. As expected, more beam current is produced when a small gap is used.

However, when the 1-cm-gap E-beams were installed on the 15-cm-long system, the scaling curve shown in Figure 24 was obtained. At high discharge current, we produce less beam current with the 1-cm gap, as compared with the 1.6-cm gap.

One factor is that in the 1.9-cm-long system beam electrons can easily traverse the full chamber length and interact with ions near the opposite beam cathode. The beam electrons partially cancel the ion space charge in the cathode-anode gap and thereby permit a higher net ion flux to reach the cold-cathode surface. This results in more beam current. However, when the waveguide length is increased to 15 cm, a smaller number
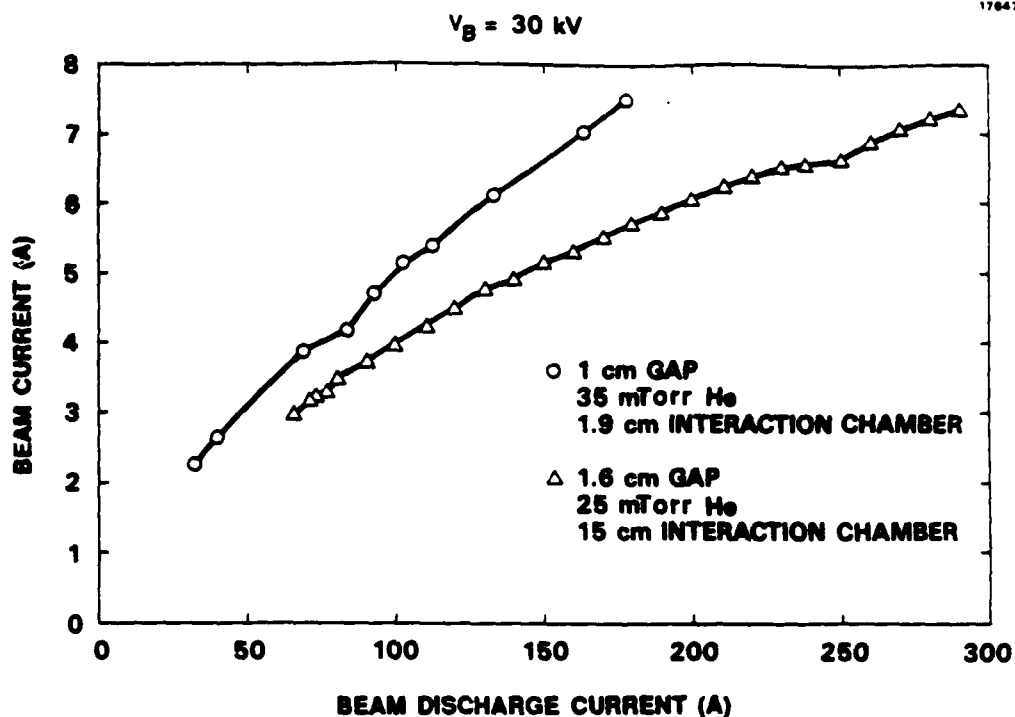
43

$V_B = 30$ kV

Figure 23. The electron beam current is increased when
the gap spacing is reduced in the 1.9-cm-long
waveguide system.

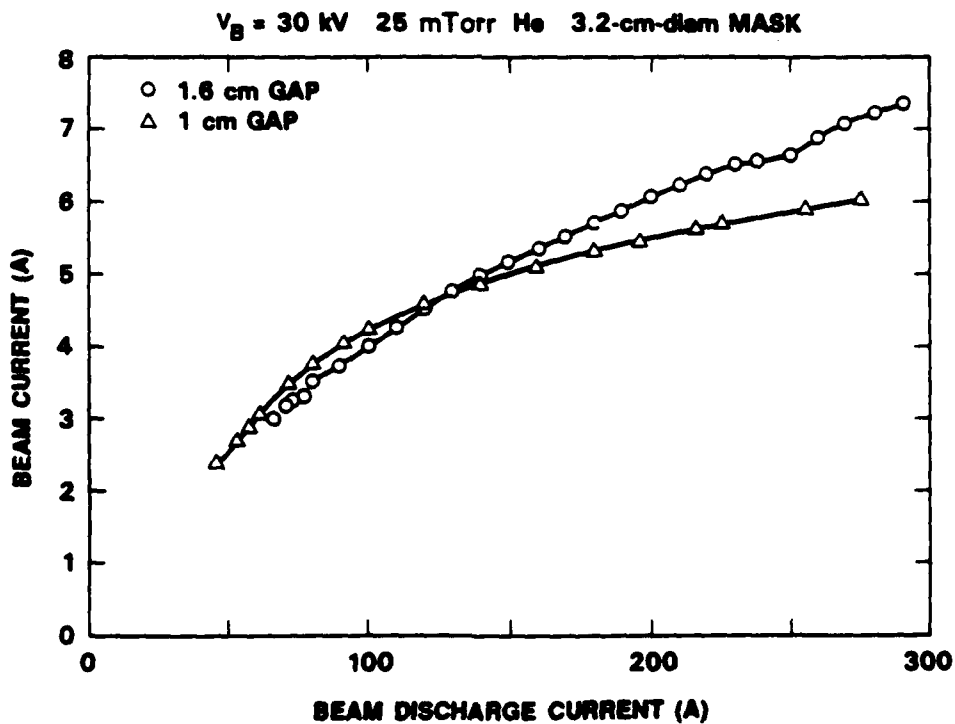$V_B = 30$ kV   25 mTorr He   3.2-cm-diam MASK

Figure 24. Reducing the gap spacing reduces the beam
current in the 15-cm-long system.

of electrons are able to traverse the long cavity and reach the opposite cathode. This lower beam density means that less neutralization of the ion current is provided by the E-beams, fewer ions are injected to the cold-cathode, and hence lower net beam current is produced. We plan to investigate this process next year by measuring the beam current scaling with discharge current for one beam as a function of the beam current and voltage of the other beam.

This explains why more beam current can be produced in the 1.9-cm-long device as compared with the 15-cm-long system, but it does not account for the reduction in beam current at high beam discharge current as shown in Figure 24. The results indicate that we cannot increase the ion current to the cathode (and thereby increase the E-beam current) by reducing the gap spacing in the 15-cm-long system.

3.3.2 Increase Beam Mask Diameter

Another way to increase the beam current is to increase the diameter of the beam mask so that more ion current can reach the cathode surface. The space-charge-limited ion current density specified by Eq. (20) has not increased, but the beam current, which is the product of the current density and the cross-sectional area of the ion-emission surface, is now higher.

We increased the cathode mask aperture diameter from 3.2 to 4.1 cm. From the ratio of the areas of the two masks, we expect an increase in beam current of up to 64%. This is illustrated in the beam current scaling with discharge current in Figure 25 which shows that the beam current increases 2.3 A (from 4.2 to 6.5 A) for a discharge current of 100 A.

However, the problem with this arrangement is that some of the electrons at the edge of the beam will impact the sides of the waveguide cavity entrance aperture if the beam does not pinch before it reaches the cavity. The current injected into the waveguide cavity would be less than the beam current measured at the cathode, and the scaling curves would be difficult to interpret. This is apparently the situation. As shown in Figure 26, the scaling of radiation power with beam current is

18206-6
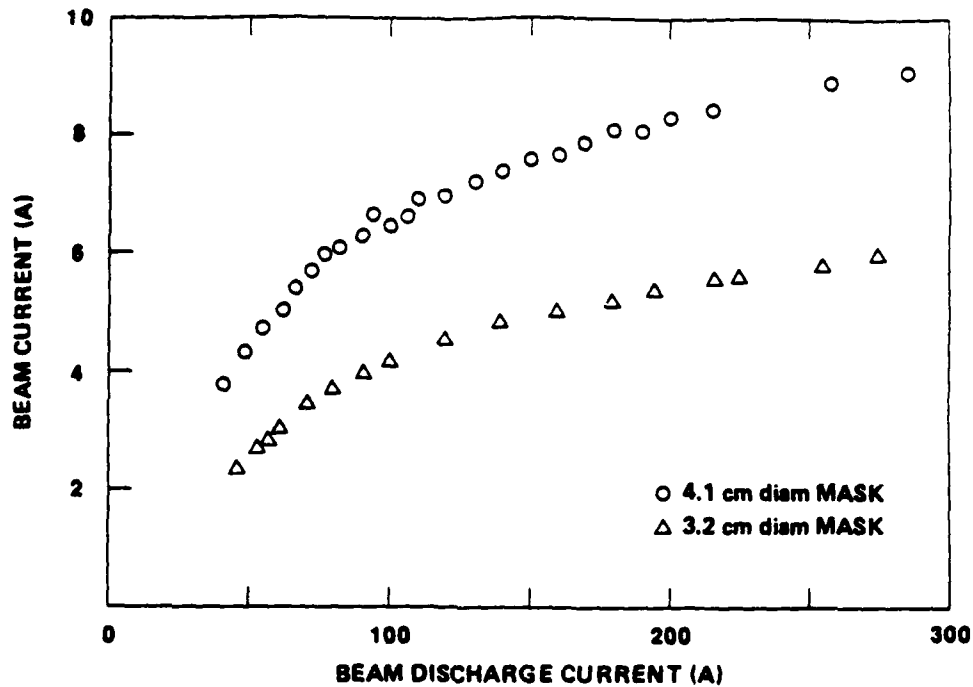
Figure 25. The emitted beam current increases when the beam mask diameter is increased.
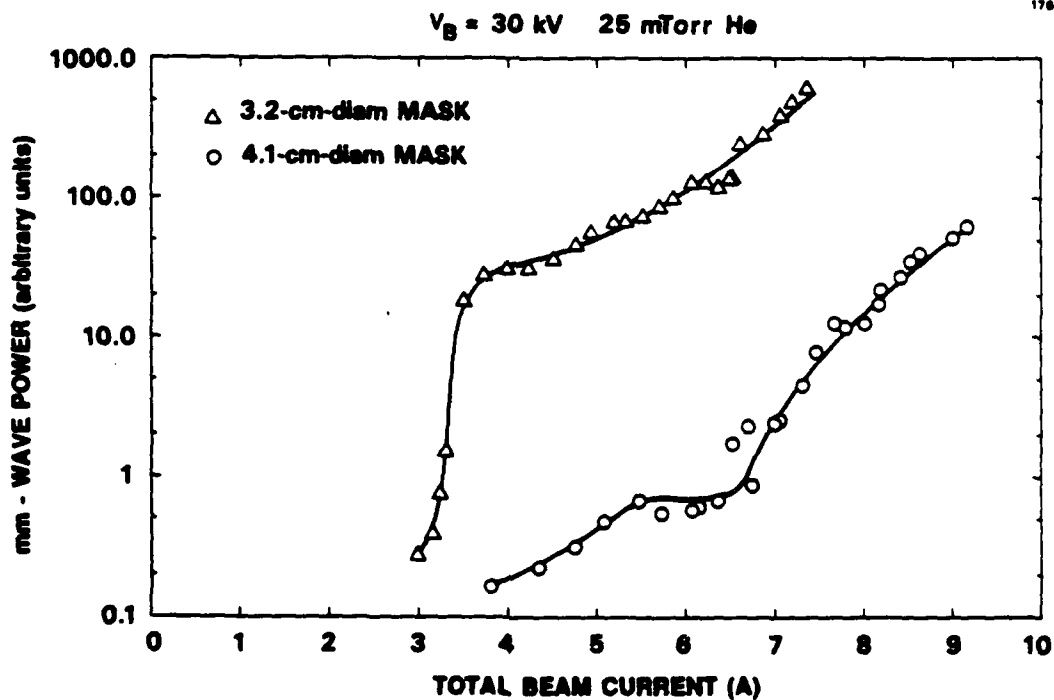
$V_B = 30$ kV   25 mTorr He

17647-7

Figure 26. The radiation power scaling with beam current indicates that some of the beam current intercepts the cavity entrance aperture and is not injected into the waveguide cavity.

46

shifted towards higher current values when the 4.1-cm-diameter
mask is used. Nonetheless, saturation of the radiation is not
observed.

3.3.3 HCP Electron Gun Development Under IR&D

An advanced electron-gun (E-gun) technique has recently been
developed for a separate Hughes IR&D-funded High-Power Microwave
(HPM) source project. The new gun is capable of producing much
higher current density E-beams, and it has been used to
demonstrate single-beam radiation emission via three-wave mixing
between beam-excited and backscattered EPWs. Called the Hollow-
Cathode-Plasma (HCP) E-gun, it employs a cold-cathode glow
discharge in low-pressure helium gas (1 to 50 mTorr) from the
inside surface of a hollow-cathode (HC) enclosure to an anode-
potential grid located just outside an aperture in the HC wall,
as shown in Figure 27.

The HC configuration with large cathode-to-anode area ratio
provides efficient confinement of ionizing electrons inside the
HC, and thus high-density plasma generation at low gas pressures.
The HC plasma is modulated by applying a negative pulse to the HC
relative to the anode grid with the HC-discharge pulse, as shown
in Figure 27. A positively biased (~1 kV) keep-alive anode-wire
is also inserted in the HC to maintain a low-current (10 mA)
continuous discharge between pulses so that the high-current
discharge pulse can be initiated on-command with low jitter
($\leq$10 ns). The HC-discharge grid has a high optical transparency
(~80%), yet ultrasmall apertures (~250 μm diameter). The high-
density plasma (n_e ~ 3×10^{12} cm^{-3} at 60 A/cm^2 current density)
behind the anode-sheath at this grid provides the high-current-
density electron emission in the HCP gun. Electrons are
extracted from the plasma and accelerated to high energy by
applying a high positive potential to the E-gun anode electrode,
which is to the right of the HC-discharge grid in Figure 27. The
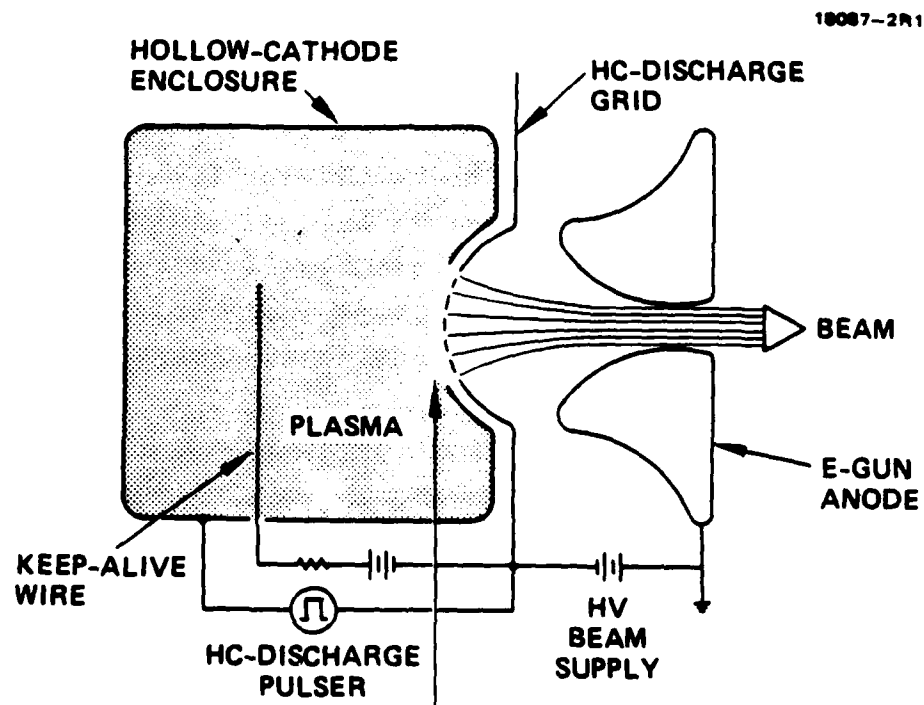
Figure 27. Hollow-cathode-plasma electron-gun configuration.

beam is electrostatically focused through the aperture in the anode to form a high-current-density, circular-cross-section beam.

The proof-of-principle HCP E-gun experiment has demonstrated the generation of well-collimated intense beams at voltages up to 70 kV, currents up to 90 A, and current densities up to 20 A/cm^2. The cathode itself has also demonstrated electron emission at a current density of 60 A/cm^2 for pulsewidths up to 100 μs. Furthermore, in a demonstration of single-beam radiation generation, the proof-of-principle HCP gun injected a single 33-kV, 18-A/cm^2 beam into a 1.6-cm-diameter waveguide and generated broadband radiation in the frequency range from 15 to 38 GHz. The radiation output had the same modulation characteristics and tunability as was previously measured in the counterstreaming beam experiment using the 15-cm-long waveguide cavity. The current-density threshold for single-beam radiation generation operation was approximately 12 A/cm^2. Next year we plan to install two HCP guns to inject higher-current-density E-beams into the 15-cm-long cavity.

3.4 RADIATION POWER SCALING AT LOW GAS PRESSURE

Many of the previous experiments were performed using helium gas pressures in the range of 25 to 50 mTorr. Recent theoretical analyses by M. Rosenberg and N. Krall have shown that the modulational instability can be an important EPW saturation mechanism. The high gas pressures typically used in the experiment help to suppress the modulational instability because the instability threshold depends on the electron collision frequency; high radiation power is generated because the instability does not limit the EPW amplitude. We investigated this by operating the 15-cm-long waveguide cavity system at reduced helium gas pressure.

3.4.1 Beam Current Scaling With Pressure

Figure 28 shows that the total beam current produced by the two-E-beam system increases as the pressure is reduced. To maximize both the influence of the modulational instability and the available beam current, we chose 12 mTorr as the operating pressure. The beam current scaling with beam discharge current at 12 mTorr is shown in Figure 29 for $V_B = 20$ kV.

3.4.2 Beam Voltage Tuning

Figure 30 displays the voltage tuning curve for 12 mTorr helium gas pressure measured using $V_B^{LV}=V_B^{HV}$. The maximum Ka-band power was observed for $V_B=20$ kV. As described in Section 3.2, this voltage tuning curve does not exhibit EM power variations due to the excitation of ES cavity modes because these modes are very closely spaced for the 15-cm-long cavity. As shown in Figure 31, the scaling of millimeter-wave power with beam voltage can be explained by considering the EPW profile that is excited by the beams. The main requirement for high power emission is that the EPWs overlap spatially so they can interact to generate the millimeter-wave radiation. In general, the EPW amplitude will grow, saturate, and then decay along the beam direction. When the beam voltage is too low, the EPWs saturate and decay at the near ends of the waveguide before they interact. When the voltage is too high, the EPWs do not grow to large amplitude until they have passed each other. The radiation generated under either of these two conditions is less then that which would be obtained if the optimum beam voltage were used. At the optimum voltage the EPWs overlap near the waveguide midplane where they have the largest amplitude.

The optimum beam voltage for 12 mTorr helium gas pressure is 10 kV lower than was measured at 30 mTorr (see Appendix A), indicating that collisional effects influence the EPW excitation and the radiation generation processess. This was confirmed by recording the radiation power scaling with beam current described in the next section.

V_B = 30 kV I_D^B = 200 A
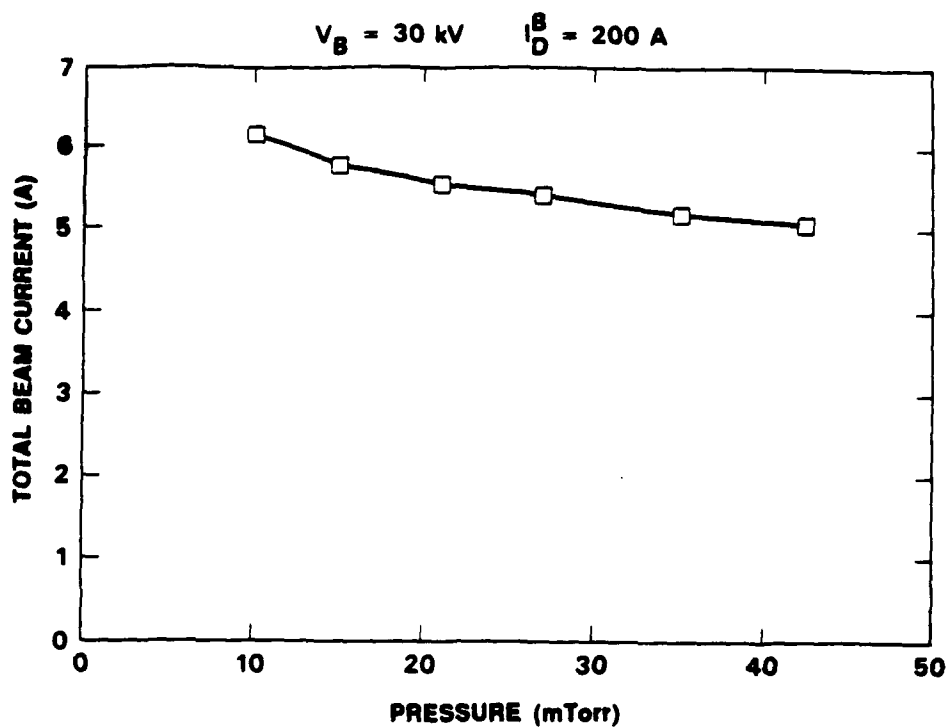
Figure 28.   The beam current is maximum at low helium
gas pressure.

V_B = 20 kV   12 mTorr He
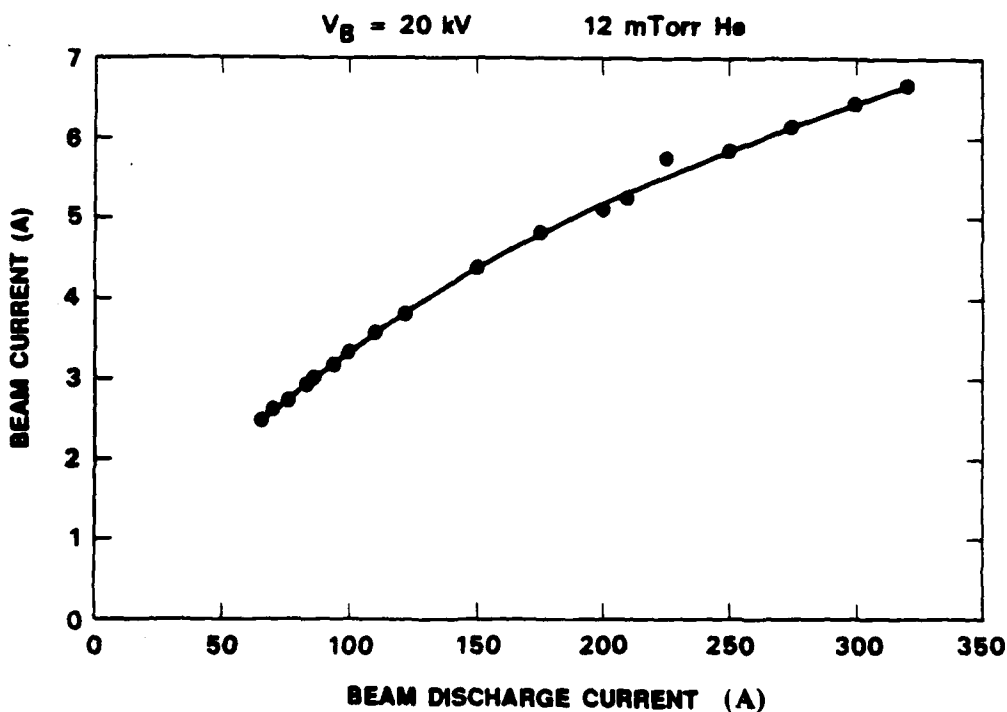
Figure 29.   Beam current scaling with beam discharge
current at low helium gas pressure.

51
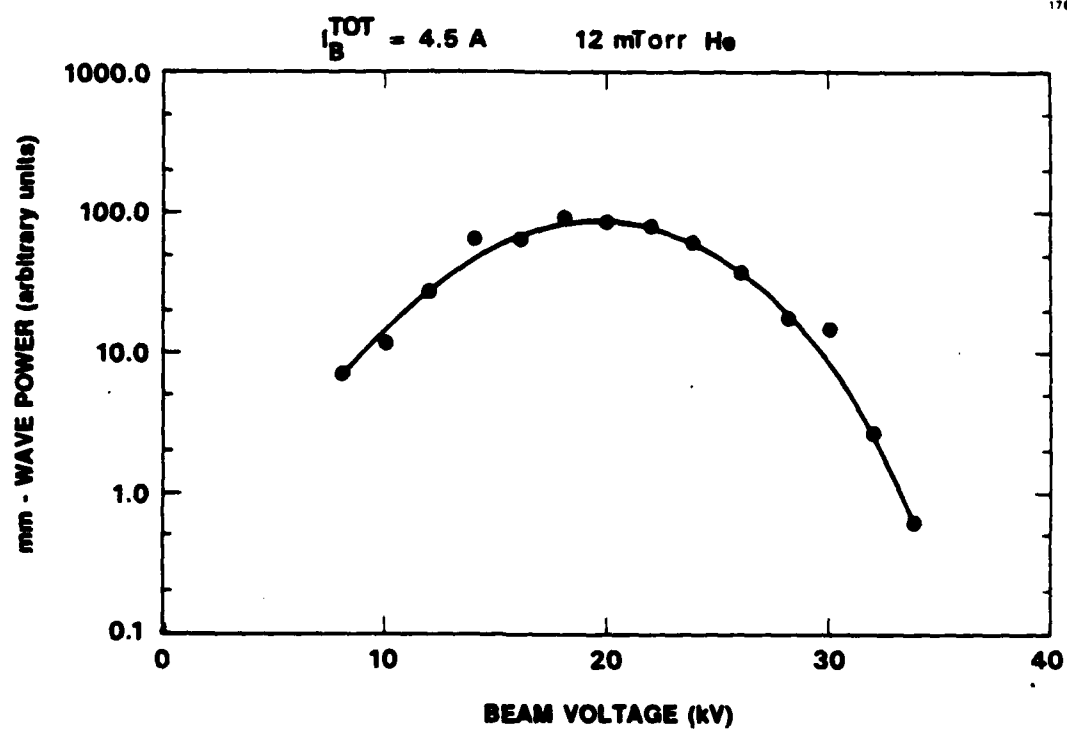
Figure 30. The radiation power scaling with beam voltage ($V_b^{LV} = V_b^{HV}$) shows that the power is maximised for 20 kV.

PLASMA -WAVE
ENERGY DENSITY

V_B TOO LOW

PLASMA-LOADED
WAVEGUIDE

$\dfrac{E_1^2}{8\pi}$

$\dfrac{E_2^2}{8\pi}$

BEAM NO. 1

BEAM NO. 2

$\dfrac{E_2^2}{8\pi}$

V_B TOO HIGH

$\dfrac{E_1^2}{8\pi}$
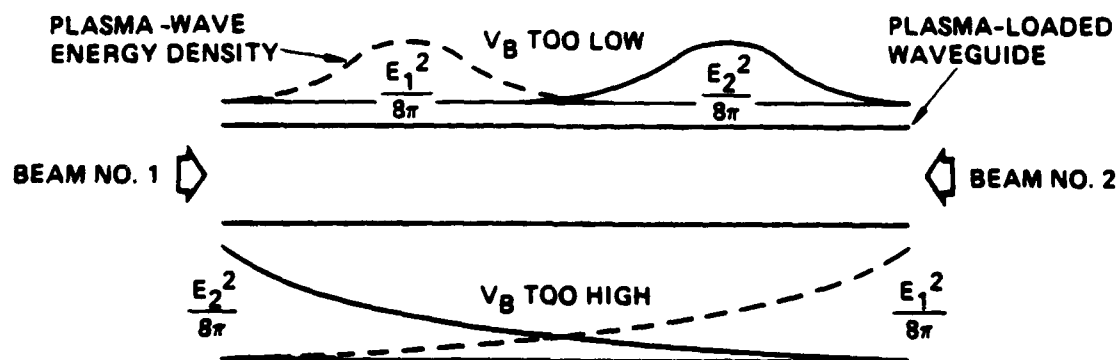
Figure 31.   Beam-plasma interaction deposits plasma-wave
energy density near the ends of the waveguide
when the beam voltages are below or above the
optimum value for a given waveguide plasma
density.   Radiation power is optimized for beam
voltages which overlap the envelopes of
plasma-wave energy density near the waveguide
midplane.

53

3.4.3 Saturation Of Output Power At Low Gas Pressure

The radiation power scaling with total beam current is presented in Figure 32. The usual threshold is observed at $I_B = 3$ A, accompanied by a rapid increase of power with beam current until $I_B = 3.8$ A. As the beam current is raised further, the curve changes slope until the radiation nearly saturates at $I_B = 6.2$ A. This saturation behavior is not observed when higher gas pressures are used (see Appendix A). This experiment provides direct confirmation that collisions control some aspects of the radiation generation saturation mechanisms.

Figure 32. The radiation power begins to saturate at high beam current when low helium gas pressure is used.

SECTION 4

INTERACTIONS

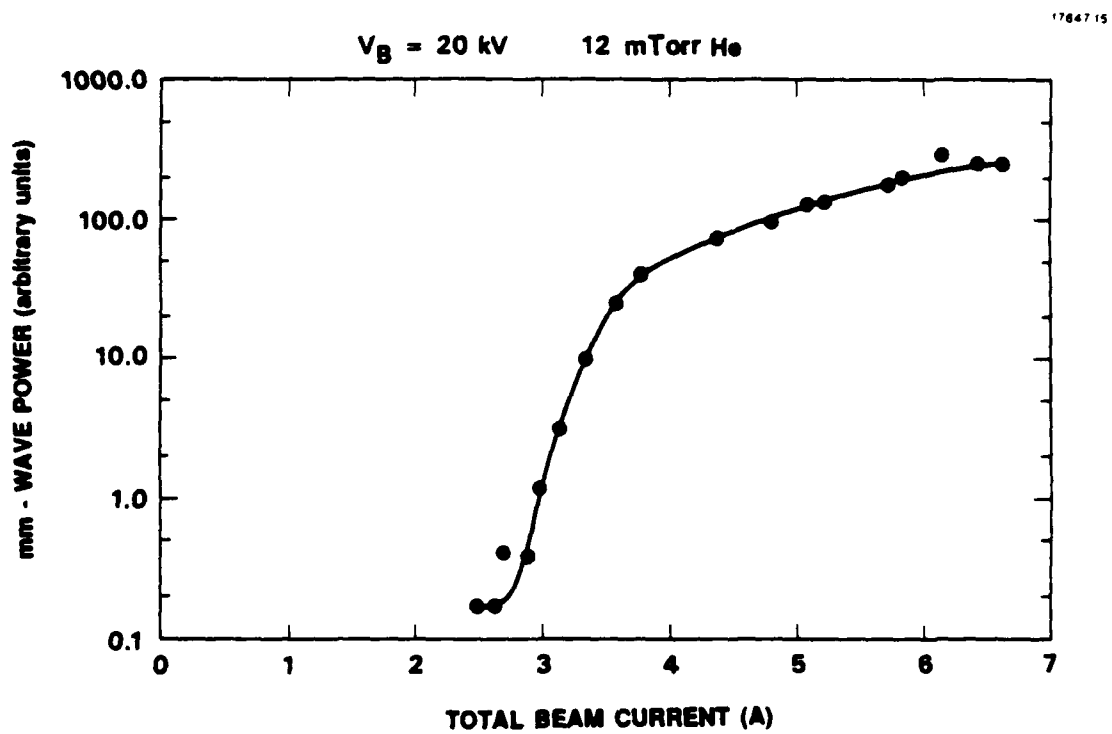**4.1** The three-wave mixing process investigated during this program has led to the development of the Plasma Wave Tube. This device incorporates a counterpropagating electron plasma wave topology to achieve multi-octave tunability in the microwave and millimeter-wave frequency range. The Plasma Wave Tube has been proposed to the Air Force Wright Aeronautical Laboratories as a broadband radiation source for an announced electronic warfare jammer.

4.2 The following papers were presented at the 1987 APS Plasma Physics Division Meeting in San Diego, California, on 5 November 1987.

"Scaling of Millimeter-Wave Radiation Generated by Counterstreaming Beams in a Plasma-Filled Waveguide," by R.W. Schumacher and J. Santoru.

"Plasma-Anode Electron Gun (PAG) Scaling," by J. Santoru, R.W. Schumacher, R.J. Harvey, and A.J. Palmer.

4.3 The following papers were presented at the 1987 IEEE International Conference on Plasma Science in Arlington, Virginia, on 1 June 1987.

"Scaling of Millimeter-Wave Radiation Generated by Counterstreaming Beams in a Plasma-Filled Waveguide," by R.W. Schumacher and J. Santoru.

"Plasma-Anode e-Gun," by J. Santoru, R.W. Schumacher, A.J. Palmer, R.J. Harvey, F.A. Dolezal, and D.J. Gregoire.

57

4.4 During the year, separate technical presentations on plasma three-wave mixing were given to members of the Air Force Wright Aeronautical Laboratories (Mr. Anthony White, Mr. Ken Helberg, and Mr. Jack Tehan).

4.5 Technical interaction between Hughes personnel and Drs. Nicholas Krall and Marlene Rosenberg of JAYCOR included meetings at HRL, at JAYCOR, and at the November APS conference.

SECTION 5

PUBLICATIONS AND PATENTS

The following publications are in preparation:

1. "Millimeter-Wave Generation Via Plasma Three-Wave Mixing," by R.W. Schumacher, J. Santoru, M. Rosenberg, and N.A. Krall. To be submitted to Physics of Fluids. A preliminary version of the paper is reproduced in Appendix A.

2. "Orbitron Radiation Mechanisms," by R.W. Schumacher. To be submitted to Physical Review Letters.

The following patent application has been submitted:

1. "Improved Plasma Wave Tube," Patent Disclosure No. PD-87441, by R.W. Schumacher and J. Santoru. This invention was made using scaling relationships developed with AFOSR support under this contract.

SECTION 6

RESEARCH PERSONNEL

The following personnel at Hughes Research Laboratories are associated with the research effort:

1. Robert W. Schumacher (Principal Investigator)
    Senior Staff Physicist (213) 317-5439.

2. Joseph Santoru (Co-Principal Investigator)
    Member of the Technical Staff (213) 317-5838.

3. Ronnie M. Watkins
    Development Engineer, Specialist (213) 317-5424.

REFERENCES

1. C. Chin-Fatt and H.R. Griem, Phys. Rev. Lett. 25, 1644 (1970).

2. P. Leung, J. Santoru, A.T. Wong, P.Y. Cheung, Physics of Auroral Arc Formation, Geophysical Monograph Series 25, 387 (1981).

3. M. Schneider and M.Q. Tran, Phys. Lett. 91A, 25 (1982).

4. P.Y. Cheung, A.Y. Wong, C.B. Darrow, S.J. Qian, Phys. Rev. Lett. 48, 1348 (1982).

5. D. Bohm and E.P. Gross, Phys. Rev. 75, 1851 and 1864 (1949).

6. M.A. Lampert, J. Appl. Phys. 27, 5 (1956).

7. F.W. Crawford, "Microwave Plasma Devices - Promise and Progress," Proc. IEEE 59, 4 (1971).

8. T.M. O'Neil, J.H. Winfreg, J.H. Malmberg, Phys. Flu. 14, 1204 (1979).

9. S. Kainer, J.M. Dawson, R. Shanny, Phys. Flu. 15, 493 (1972).

10. S.A. Self, M.M. Shoucri, F.W. Crawford, J. Appl. Phys. 42, 704 (1971).

11. I. Alexeff and F. Dyer, Phys. Rev. Lett. 45, 351 (1980).

12. G.W. McClure, "Low-pressure glow discharge," Appl. Phys. Lett. 2, p. 233 (1963).

13. J.R. Bayless and R.J. Harvey, U.S. Pat. No. 3, 949, 260 (1976) (Assigned to Hughes Aircraft Company).

14. D. Pigache and G. Fournier, "Secondary-emission electron gun for high-pressure molecular lasers," J. Vac. Sci. Tech. 12, 1197-1199 (November/December 1975).

15. G. Wakalopulos, "Ion Plasma Electron Gun," U.S. Pat. No. 3, 970, 892, Hughes Aircraft Company, July 20, 1976.

16. P.F. Little, "Secondary Effects," Band XXI, Vol. XXI, Handbook Der Physics (1956). Also see A.G. Hill et al., Phys. Rev. 55, 463-470 (March 1939).

17. R.W. Schumacher and R.J. Harvey, "CROSSATRON Modulator
    Switch," Conference Record of the Sixteenth IEEE Power
    Modulator Symposium," Arlington, Virginia, June 1984.
    (p. 139).

18. R.W. Schumacher and R.J. Harvey, "CROSSATRON Modulator
    Switch: A Long-Life Component for Pulsed-Power Systems,"
    Fifth IEEE Pulsed-Power Conference.

19. M. Rosenberg and N. Krall, Bull. Am. Phys. Soc. $\underline{32}$, 1885
    (1987).

APPENDIX A

This appendix contains a preliminary draft of the three-wave
mixing paper we are preparing for publication in collaboration
with Drs. N. Krall and M. Rosenberg of JAYCOR. The final draft
will include the extensive theoretical calculations performed by
Drs. Rosenberg and Krall, and in-depth discussions about the
experimental results.

ABSTRACT

We report the generation of microwave and millimeter-wave radiation via the nonlinear interaction of electron plasma waves. The experiment employs two counter-injected electron beams in a plasma-loaded waveguide to drive counterpropagating electron plasma waves. The nonlinear coupling of these waves generates an electromagnetic waveguide mode that oscillates at twice the plasma frequency. Independent control of waveguide plasma density, gas species, beam voltage, and beam current allows a careful parametric study of the interaction mechanisms. Radiation frequencies as high as 60 GHz with beam-to-radiation power conversion efficiencies of up to 4% are estimated.

SECTION 1

INTRODUCTION

The generation of electromagnetic (EM) radiation in plasmas has been studied intensely for many years. Areas of investigation range from space plasmas (e.g., Type III solar radio bursts[1]) to high-power microwave generators.[2,3] The energy source usually consists of an electron beam (E-beam) propagating through a background plasma. Depending on the plasma conditions, the beam drives instabilities which interact to generate radiation. One mechanism that produces radiation involves the interaction of electrostatic plasma waves.[4-14] These processes include the scattering of beam-excited electron plasma waves (EPWs) from lower-frequency ion waves (radiation is produced near the plasma frequency ν_p), and the beating of two counterpropagating EPWs to produce a transverse EM wave with frequency $2\nu_p$.[15-17] Although the latter process normally requires two E-beams directed toward a common interaction volume, a single E-beam can be used if the beam-driven EPWs are of sufficient amplitude that they can be backscattered. Another radiation-producing process is soliton collapse, in which the beam-excited EPWs collapse spatially; this process is accompanied by radiation emission at the plasma frequency and its harmonics.[18]

Prior experiments that explored the EPW-EPW interaction physics used low-voltage, low-current E-beams to excite the plasma waves.[15-17] The EPW growth and propagation properties were studied, together with the resultant radiation emission. The radiation levels were very low (~-60 dBm) with poor beam-to-EM wave conversion efficiencies.[15] To the best of our knowledge, our investigation is the first to use high-power ($\leq$90 kV, $\leq$6 A) beams in a high-density, plasma-filled waveguide to generate

substantial radiation power levels (≤ 8 kW) at millimeter-wave frequencies with efficiencies as high as a few percent.

The paper is organized as follows. In Section 2, we delineate a simple plasma three-wave mixing model. Section 3 contains a description of the experimental apparatus. In Section 4, the high-voltage beam dynamics are discussed. In Section 5 we present the experimental results, including plasma-density, beam-voltage, and beam-current scaling data.

SECTION 2

THEORETICAL BACKGROUND

Plasma three-wave mixing, which is the term we apply to the wave-wave coupling and radiation emission process, is based on beam-plasma interactions[19,20] that have been explored in numerous publications for almost 40 years. Beam-plasma phenomena are attractive for radiation generation because of the ease with which intense, high-frequency EPWs can be excited when a high-power E-beam is injected into a dense plasma. However, the problem of efficiently coupling the power in the electrostatic waves to a radiation field has hindered[21] previous attempts to use plasmas in millimeter-wave sources or amplifiers. These problems can be overcome by using the three-wave-mixing process. In the following theoretical discussion, we summarize the basic physics of beam-driven EPWs and present a simple kinematic model for the nonlinear coupling of two EPWs to the radiation field in a plasma-filled waveguide.

2.1 EXCITATION OF EPWS

We begin the discussion by restricting the treatment to a weak, cold beam with density n_b and velocity v_b. By "weak" beam we mean that the ratio of beam density to plasma electron density,

$$\frac{n_b}{n_e} \equiv \epsilon \quad , \tag{1}$$

is small compared with unity ($\epsilon \ll 1$); by "cold beam" we mean that the beam temperature is much less than the beam energy.

Under these conditions, linear hydrodynamic theory[19,20,22,23] (electron-beam flow through an electron fluid that is stationary in the lab frame with a fixed ion background) shows that the beam will excite electron-plasma waves with phase velocity

$$\frac{\omega_e}{k_e} \simeq v_b \quad , \tag{2}$$

and, with the well-known Bohm-Gross dispersion,

$$\omega_e^2 = \omega_p^2 + 3k_e^2 v_{th}^2 \simeq \omega_p^2 \quad , \tag{3}$$

where ω_e and k_e are the EPW frequency and wave number, v_{th} is the plasma-electron thermal speed, and ω_p (= $2\pi\nu_p$) is the plasma frequency given by

$$\omega_p = \left(\frac{4\pi n_e e^2}{m_e}\right)^{1/2} \quad . \tag{4}$$

Because v_{th} is much less than v_b, the second term in Eq. (3) is much less than ω_p^2, so we have $\omega_e \simeq \omega_p$. The waves will grow along the beam trajectory with temporal growth rate,

$$\Gamma_t = \frac{3^{1/2}}{2^{4/3}} \epsilon^{1/3} \omega_e \quad , \tag{5}$$

and spatial growth rate,[24]

$$\Gamma_z = \frac{3^{1/6}}{2^{4/3}} \epsilon^{1/3} \left(\frac{v_b}{v_{th}}\right)^{2/3} k_e \quad . \tag{6}$$

The linewidth of the excited waves expressed in terms of wave number spread is also related to beam strength ϵ according to

$$\frac{\Delta k_e}{k_e} \sim \frac{3}{2^{5/6}} \epsilon^{1/3} \quad . \tag{7}$$

Nonlinear theory[22,23] shows that the EPW gains energy from the beam until it saturates by trapping beam electrons and

broadening the beam-velocity distribution function. The saturated energy density in the EPW is given by

$$W = \frac{\langle E^2 \rangle}{4\pi} = \frac{n_b m_e v_b^2}{2} \left(\frac{\epsilon}{2}\right)^{1/3} . \tag{8}$$

Because the factor $n_b m_e v_b^2/2$ is just the energy density in the E-beam, Eq. (8) shows that the fraction of beam energy coupled to EPW energy is $\sim [(\epsilon/2)^{1/3}]$. Note that for $n_b/n_e = 4\%$, up to 27% of the beam energy can be transferred to the EPWs.

The EPWs can drive instabilities if they are of sufficient amplitude. For example, the large-amplitude EPWs can excite electron and ion plasma waves via the modulational instability, thereby limiting the EPW amplitude. In our experiment, however, we use high background pressures, which in turn increases the instability threshold. This can lead to a higher EPW amplitude and greater radiation conversion efficiencies because the EPWs can grow to larger amplitudes before the instability clamps the EPW amplitude.

The ratio $W/n_e T_e$ (where $n_e T_e$ is the plasma energy density) quantifies the strength of the beam-plasma interaction. For $W/n_e T_e$ greater than a few percent, the electric fields in the EPW begin to modify the plasma through ponderomotive-force effects. In this regime the EPWs and the plasma become strongly coupled and the beam-plasma system is said to be in the strong turbulence regime. In the opposite limit, where W is so small that

$$W/n_e T_e < (k_e \lambda_D)^2 , \tag{9}$$

where λ_D is the electron Debye length $[\lambda_D = (kT_e/4\pi n_e e^2)^{1/2}]$, the beam-plasma system is said to be weakly turbulent.

2.2 COUPLING OF THE EPWs TO THE RADIATION FIELD

The oscillating field of the EPW contains the power that we wish to extract from the E-beam, but the power is trapped in the plasma as an electrostatic wave and must be coupled out in some

manner as an electromagnetic mode. We employ two
counterstreaming E-beams to excite two counterpropagating EPWs,
as shown in Figure 1. These two waves are then nonlinearly
coupled to a TM electromagnetic waveguide mode via plasma three-
wave mixing. In this process, the electric field of one wave
induces a velocity increment δv_e in the electron density
fluctuations δn_e present in the second wave, thereby generating a
nonlinear source current that is expressed as

$$J = e\delta n_e \delta v_e \quad . \tag{10}$$

This source current is nonlinear because it is a product of two
first-order fluctuations of the two linear, primary waves.

The plasma three-wave-mixing process can be described
quantitatively by using the dispersion relation for the plasma-
loaded-waveguide mode and the energy and momentum conservation
relations for three-wave mixing:

$$[\text{dispersion}] \qquad \omega_o^2 = \omega_p^2 + \omega_c^2 + k_o^2 c^2 \tag{11}$$

$$[\text{energy conservation}] \qquad \omega_o = \omega_{p_1} + \omega_{p_2} = 2\omega_p \tag{12}$$

$$[\text{momentum conservation}] \qquad \vec{k}_{e_1} + \vec{k}_{e_2} = \vec{k}_o \quad . \tag{13}$$

In these relations ω_o is the electromagnetic-waveguide-mode
frequency; ω_{p_1} and ω_{p_2} are the EPW angular frequencies; ω_c is the
waveguide-cutoff frequency in vacuum; k_{e_1} and k_{e_2} are the EPW
wave numbers; and k_o is the electromagnetic wave number.
Dispersion for each beam-mode plasma wave is described by
Eq. (2). As a consequence of wave-energy conservation
[Eq. (12)], the current J [of Eq. (10)] oscillates at twice the
EPW frequency. The oscillating axial current then couples to a
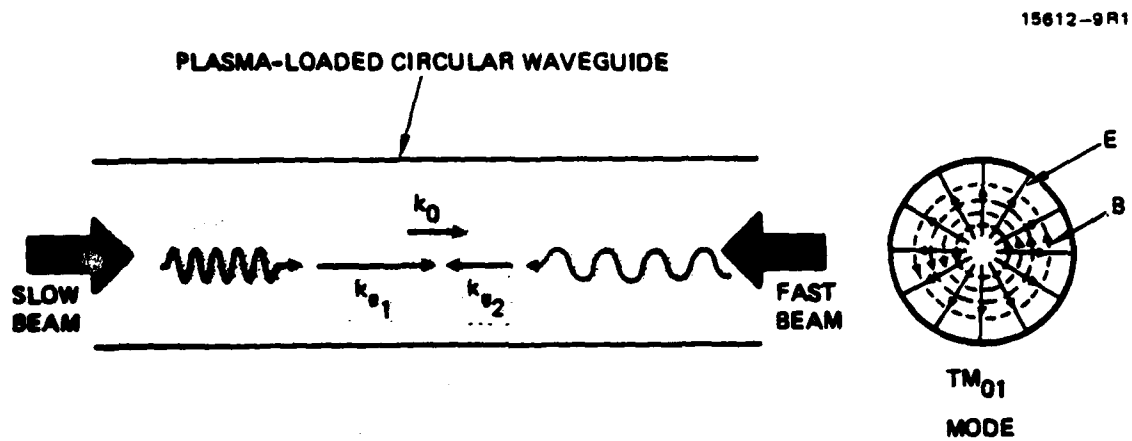TM electromagnetic waveguide mode at $2\nu_p$.

Figure 1. Beam-plasma-waveguide system.

The beam speeds, and thus the phase velocities of the EPWs, are always smaller than the phase velocity ($\geq c$) of the electromagnetic wave. Consequently, k_{e1} and k_{e2} will be larger than k_e. To satisfy Eq. (13) with colinear but oppositely directed EPWs, the two E-beam speeds must therefore be unequal for finite k_e. Cutoff waveguide modes with $k_e=0$ will be excited for equal beam speeds. The beam-speed difference can be expressed in terms of the plasma-waveguide parameters by solving Eqs. (2), (3), (11), (12), and (13) simultaneously. Inserting Eq. (12) into (11) and solving for k_e, we obtain the waveguide-mode wave number:

$$k_o = \frac{\left(3\omega_p^2 - \omega_c^2\right)^{1/2}}{c} \quad . \tag{14}$$

This equation shows that ω_p must be greater than or equal to $3^{-1/2}\,\omega_c$ in order to couple to a waveguide mode. Inserting Eqs. (2) and (3) into (13) and equating the result to (14), we obtain the desired equation that relates the beam speeds to the plasma-waveguide parameters:

$$v_{b_2} - v_{b_1} = \frac{\left(3 - \omega_c^2/\omega_p^2\right)^{1/2} v_{b_2}\, v_{b_1}}{c} \quad . \tag{15}$$

In this equation, v_{b1} is the speed of the slow beam from the low-voltage gun and v_{b2} is the speed of the fast beam from the high-voltage gun. Note that this tuning condition is applicable only to weak beams ($n_b/n_e < 10^{-4}$). In the strong-beam case (strong-turbulence regime), a broad spectrum of EPW wave numbers can be generated, and the velocity requirements in Eq. (15) can be relaxed. Note also that for high-order TM modes with large $\omega_c \sim 3^{1/2}\omega_p$, Eq. (13) requires that the two beam speeds be closely matched.

The dispersion relations described by Eqs. (2), (3), (11), (12), and (13) are plotted in Figure 2. The plot shows how two
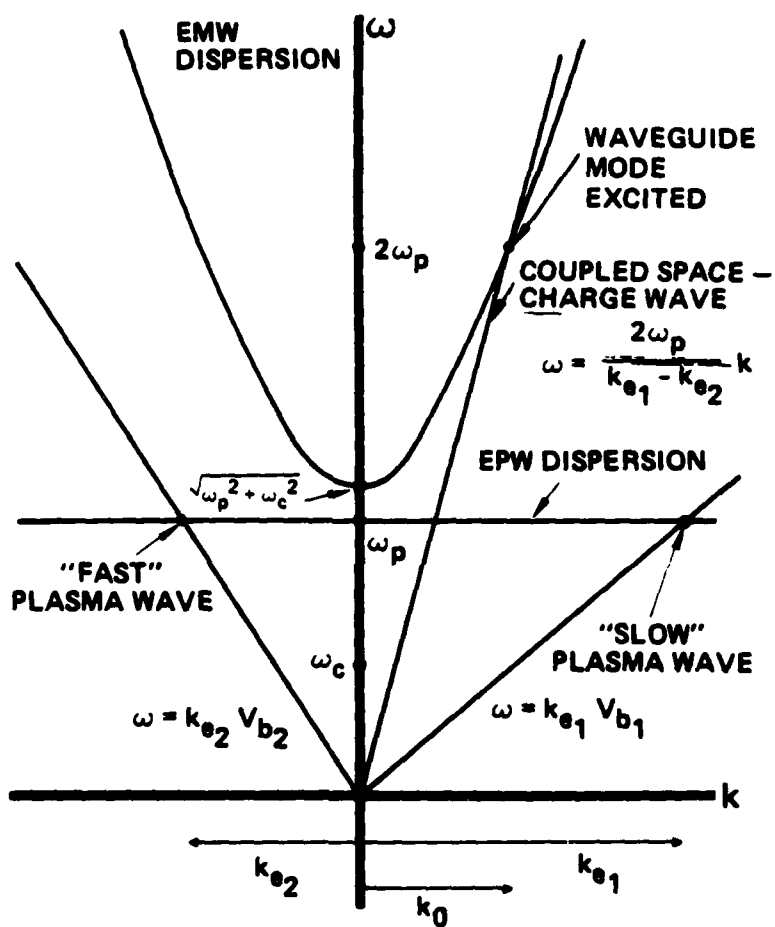
Figure 2. Dispersion relations for plasma three-wave mixing.

oppositely directed EPWs with different phase velocities (ω_p/k_{e1} and ω_p/k_{e2}) are coupled to a third space-charge wave with dispersion

$$\omega = \frac{2\omega_p}{k_{e_1} - k_{e_2}} \, k \quad .$$ (16)

A plasma-loaded-waveguide mode is excited at the intersection of this coupled space-charge wave with the electromagnetic dispersion curve.

As an example of a solution to Eq. (15), consider an experiment with a 3.81-cm-diameter waveguide operating in V-band at $\nu_o = 50$ GHz. The plasma frequency ν_p will be 25 GHz, so Eq. (4) indicates that the waveguide plasma density must be $7.8 \times 10^{12} \text{cm}^{-3}$. The cutoff frequency ν_c of the TM_{e1} mode in the waveguide in vacuum is 6 GHz. If the energy of the fast E-beam is chosen at 60 kV, then the slow-beam energy must be 18 kV in order to satisfy Eq. (15). However, if a higher-order $TM_{n e}$ mode is excited with $\nu_c \sim 43$ GHz, Eq. (15) requires that the beam energies be equal.

SECTION 3

EXPERIMENTAL APPARATUS

Figure 3 is a diagram of the experimental apparatus. High-density plasma ($\leq 1\times 10^{13}$ cm^{-3}) is generated by a 12-wire, wire-anode discharge[25-27] in the annular space surrounding a 3.8-cm-diameter, 15.2-cm-long perforated waveguide with the background gas pressure in the 1-to-50-mTorr range. The microperforations allow both ionizing discharge electrons and background plasma to penetrate the waveguide, thus loading it with a high-density, quiescent plasma. The perforations are large compared with a Debye length, but small compared with the electromagnetic wavelength; therefore, radiation remains trapped in the guide while plasma can pass through freely. Both ends of the circular waveguide are terminated by highly transparent grids (80%). Radiation is coupled out of this waveguide-cavity configuration through rectangular waveguides that are oriented to align the electric-field vector of the $TE_{1\theta}$ (rectangular-waveguide) mode with the axial electric field of a TM mode in the circular waveguide.

Secondary-emission electron guns[28,29] are used to generate the E-beams. As shown in Figure 3, each gun employs a separate wire-anode discharge in the region between the waveguide and the electron-gun E-beam cathode. The plasma in this discharge is partially confined between the waveguide-terminating grid on one side and a similar grid on the opposite side near the cathode. This latter grid also serves as the anode for the E-gun. A fraction of the ions produced in this plasma are extracted through the anode grid and are accelerated to the flat cathode (which is continuously held at negative high voltage), where they bombard the molybdenum electrode surface and produce secondary electrons. These electrons are accelerated back through the cathode-anode gap, forming a high-energy beam. The beam then passes through the anode grid and the waveguide-terminating grid and is injected into the waveguide with low (~36%) loss to the
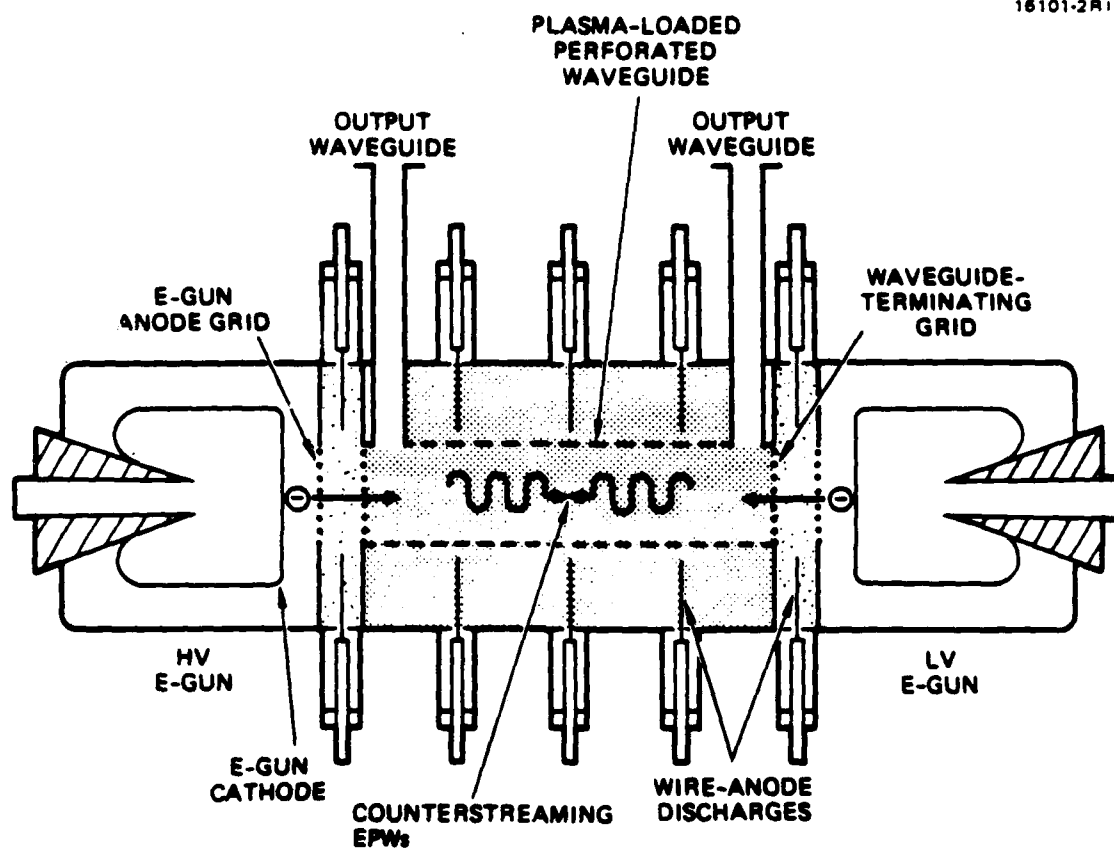
16101-2R1

Figure 8. Experimental beam-plasma apparatus.

grid structures. The beam then propagates through the plasma-filled waveguide where ion charge in the plasma neutralizes the electron space charge in the beam. This "ion-focusing" effect allows the beams to propagate without requiring the use of magnetic-focusing fields. The experimental parameters are listed in Table 1.

TABLE 1. Experimental Parameters.

Gas	H_2, He, Ne, Ar, Kr, or Xe at 1 to 50 mTorr; typically He at 24 mTorr
Plasma	$n_e = 2 \times 10^{11}$ cm^{-3} to 10^{13} cm^{-3}
Beams	$V_b \leq 90$ kV, typically 20 to 50 kV $I_b \leq 3.5$ A $T_b \geq 15$ eV $J_b \leq 4$ A/cm^2 $n_b \leq 6 \times 10^9$ cm^{-3}, $0.03\% \leq n_b/n_e \leq 3\%$
Waveguide	3.8-cm diameter, 15.2-cm long

The utility of the secondary-emission gun is based on the high secondary-emission yield γ_e, which is obtained when high-energy ions strike gas-covered cathode-electrode materials. For example, γ_e varies from 5 to 15 when helium ions in the 35-to-150-kV range strike a molybdenum cathode in the presence of 20 mTorr of helium gas.[36]

The E-beam current is controlled at low voltage by modulating the ($\leq$1-kV) wire-anode discharge at the ground-potential environment of the anode electrode. Because the plasma is confined within the gridded-anode structure (plasma electrons are unable to overcome the $\simeq$1-kV discharge-cathode drop to penetrate the gridded structure for ion current densities up to some limit), plasma closure of the high-voltage gap cannot occur and

long-pulse (>>1 μs) operation is achieved. Modulation of the plasma source modulates the ion flux incident upon the cathode, which in turn controls the beam current. A mono-energetic beam is obtained throughout the beam pulse because the E-beam is switched ON and OFF by the plasma source and not by the high-voltage supply for the cathode. Low-energy electrons produced from the rise and fall of the cathode voltage in conventional pulsed beams are not present. All of this is accomplished without heater power and without high-vacuum-environment requirements, because the metallic cathode used in the secondary-emission gun cannot be poisoned.

The experiment is typically operated with 10-to-25-μs-wide flat-top pulses at a pulse-repetition frequency of 1 Hz. A 25-μs pulse-forming network (PFN) is employed to drive current pulses up to 800 A in the main waveguide-plasma-discharge section. A higher-impedance 18-μs PFN drives the wire-anode discharge in the low-voltage (LV) E-gun. Ignitrons are used as closing switches to discharge both PFNs. The wire-anode discharge in the high-voltage (HV) E-gun is modulated by a circuit consisting of a capacitor and a XTRON-3 CROSSATRON[R] Modulator Switch (CMS).[31,32] The Hughes CMS is an advanced thyratron-like device that both closes and opens under grid control, so square-wave pulses can be obtained in hard-tube-modulator fashion without having to use a fixed-pulse-length PFN. The E-gun wire-anode current pulses are typically 10 to 150 A. Finally, capacitors are used to continuously maintain high voltage on the E-gun cathodes through 1-kΩ current-limiting resistors. The HV E-gun is designed to operate up to 120 kV, and the LV E-gun up to 50 kV.

Each of the discharge and high-voltage beam circuits is instrumented with high-voltage probes and current transformers. These diagnostics, as well as the Langmuir probes, are interfaced to an 11-channel PC-based data-acquisition system and an oscilloscope array, which are housed within an RFI-screen room. The output waveguides are also fed into the screen room where the radiation is analysed by a network of microwave and millimeter-

wave detectors, filters, attenuators, and mixers. Figure 4 is a schematic of the detection system. The maximum sampling rate of the analog-to-digital converters in the computerized data acquisition system is 1 GHz.

One axial and two radial Langmuir probes are employed to determine the plasma parameters in the plasma-loaded waveguide. Each probe consists of a 1-mm-diameter tantalum disk, which has a negligible perturbation effect on the discharge. The radial probes, which are attached to the experiment permanently, are also used to measure the E-beam profiles. One E-gun is removed and the axial probe is installed temporarily in order to measure the axial plasma profile. The observed profile is shown in Figure 5 under conditions where the center anode wires are either disconnected from the power supply or are driven through 47-Ω resistors. When the center wires collect discharge current, the profile is more strongly peaked near the midplane. When the center wires are disconnected so that all the current is collected by the eight end-wires, the profile is significantly more uniform. Plasma leakage from each E-gun wire-anode discharge also contributes to profile uniformity near the ends of the waveguide.
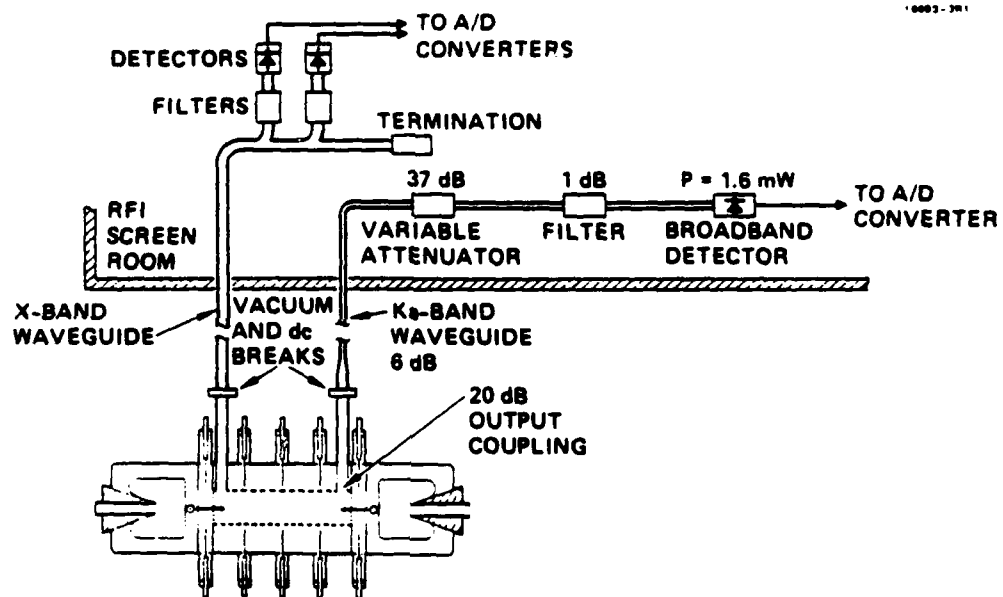
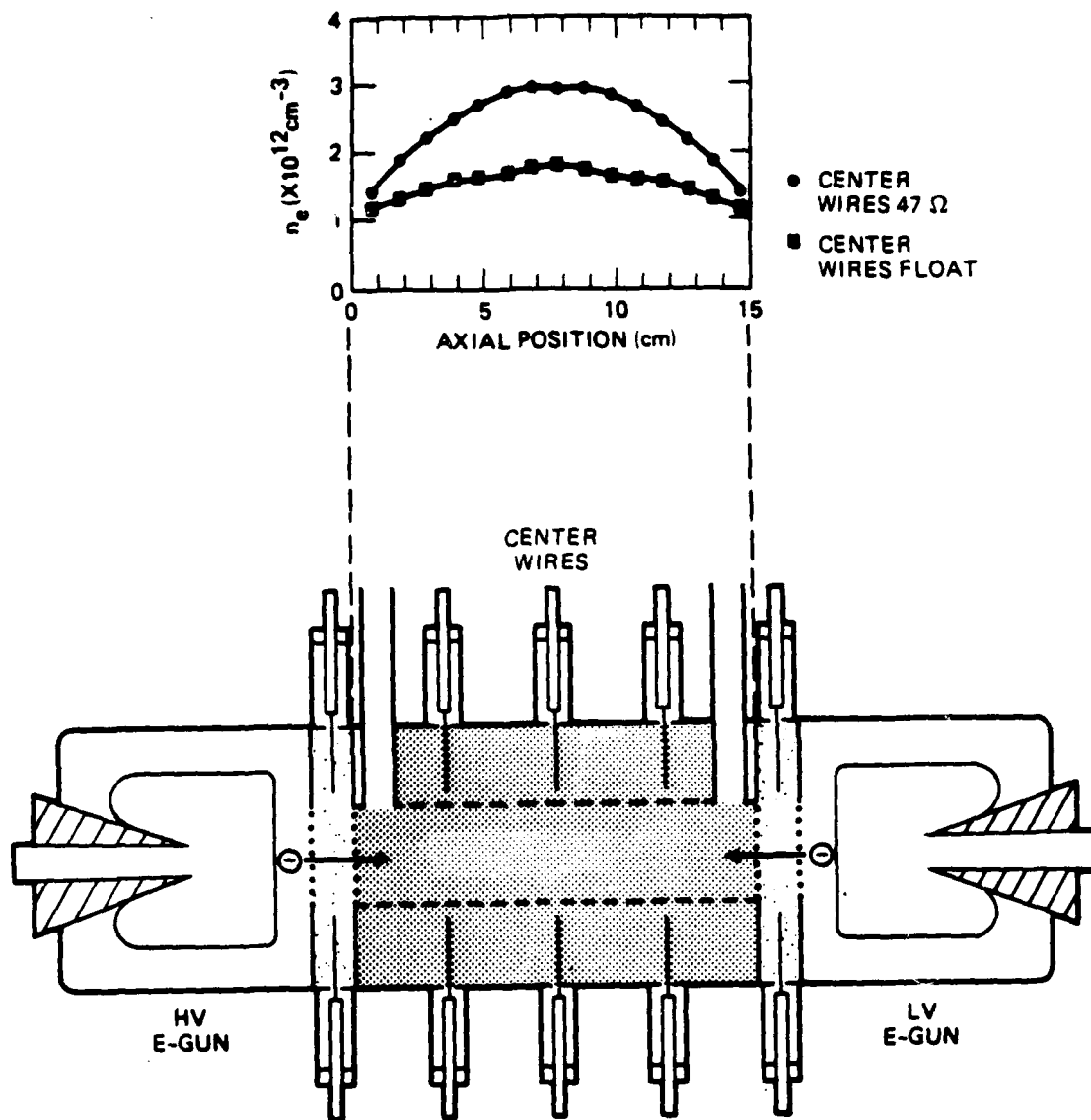**Figure 4.   Millimeter-wave diagnostics and power measurement system.**

Figure 5. Axial plasma-density profiles.

SECTION 4

BEAM DYNAMICS

The radial plasma-density and E-beam profiles measured in
the output-coupling sections using disk probes are shown in
Figure 6. The E-beam (50 kV, 5 A) profile reveals a well-
collimated beam that converges rather than diverges as the beam
propagates through the plasma-loaded waveguide. At the beam-
injection end of the waveguide (near the first output rectangular
waveguide), the beam-current profile rises sharply on the edges
and falls toward the axis. This profile is related to the ion
density profile in the wire-anode-discharge section of the E-gun.
The density is higher on the edge near the wires and lower near
the axis. The 3.18-cm-diameter anode grid defines the beam
diameter within the 3.81-cm-diameter waveguide.

At the opposite end of the waveguide (near the second output
rectangular waveguide), as shown in Figure 6, the beam has
converged after passing through the waveguide plasma. The full
width at half maximum has decreased from 2.7 to 0.45 cm, and the
beam current density on axis has increased by a factor of ~8
despite beam attenuation by the plasma.

This radial beam contraction is caused by the self-magnetic
pinch of the E-beam. The beam generates a poloidal magnetic
field, which can constrict the beam radius if the magnetic-field
pressure exceeds the (transverse) beam thermal pressure.
Electrostatic forces are neglected because the beam is charge-
neutralized by the waveguide plasma. This process is known as
the Bennett pinch effect.[33] Quantitatively, the pinch condition
can be expressed as:

$$\frac{B_p^2}{8\pi} \geq n_b T_b \quad , \tag{17}$$

where B_p is the poloidal magnetic field, and T_b is the
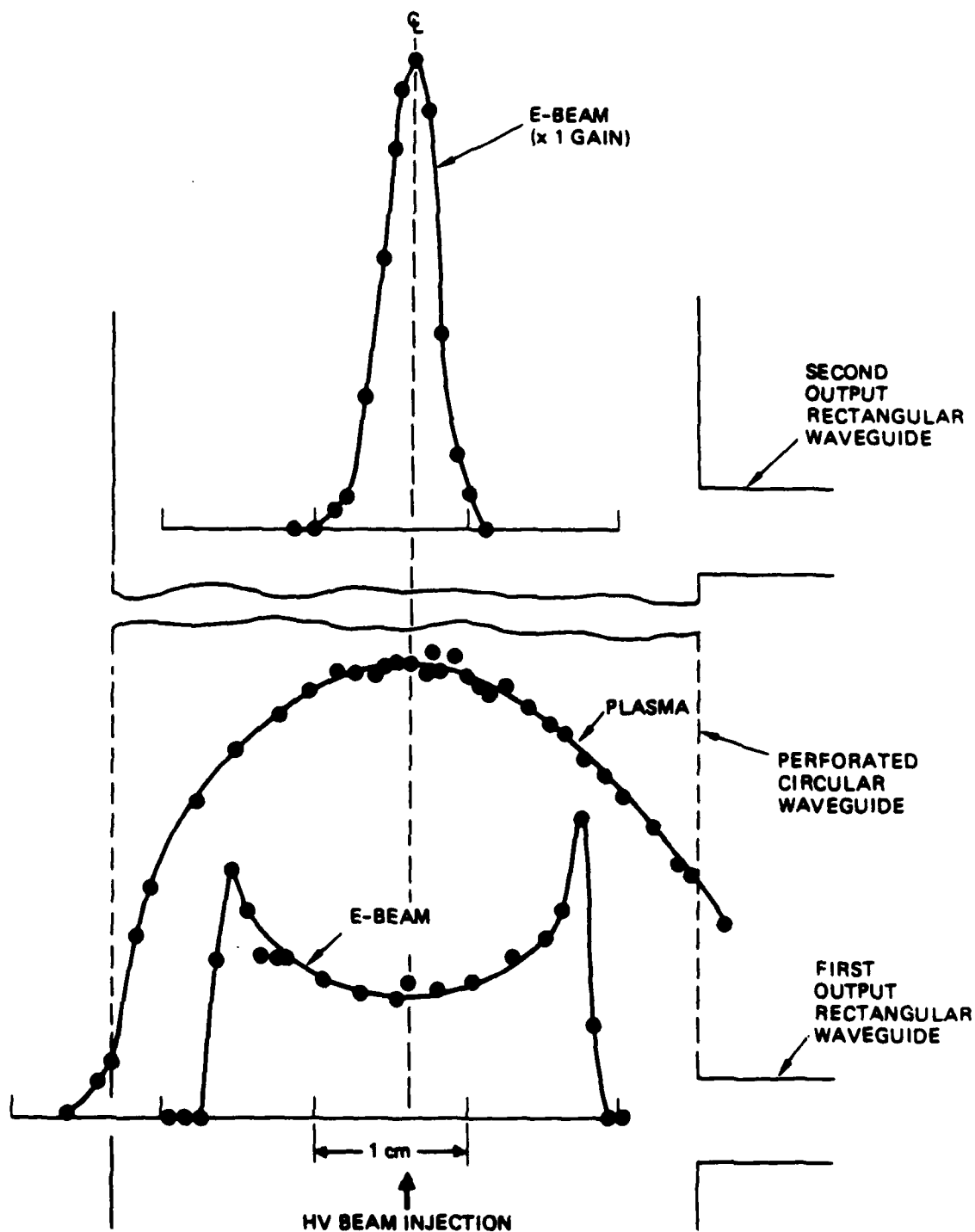perpendicular beam temperature. The threshold current at which

Figure 6. Radial plasma and electron-beam profiles measured across the diameter of the circular waveguide at two axial positions which correspond to the output waveguide locations.

the pinch occurs can be expressed as:

$$I_b^2 \geq 3.2 \times 10^{-10} \, n_b \, A_b \, T_b \quad , \tag{18}$$

where A_b is the cross-sectional beam area. Using a beam density of $3 \times 10^9 cm^{-3}$ and $T_b = 10$ eV we predict a threshold current of 1.5 A, which is consistent with our measurements, as discussed below.

The beam is predicted to evolve into the Bennett profile,

$$I_b(r) = \frac{I_{b_0}}{\left[1 + (r/a)^2 \right]^2} \quad , \tag{19}$$

where r is the radial position relative to the center of the beam, $a = (2\sqrt{2} \, \lambda_0/\beta) [T_b /(T_b - T_e)]^{1/2} \equiv$ Bennett radius, and $\beta = v/c$. A comparison of several measured radial beam profiles with the theoretically predicted Bennett profile is shown in Figures 7 and 8. In each case, we assume $T_b = 10$ eV. There is good agreement between experiment and Bennett-pinch theory.

The pinching length, or distance the beam travels before it becomes fully pinched, can be estimated from the inverse betatron wavenumber.[34] This is given by $k_\beta^{-1} \sim r_b (2I_b/I_A)^{-1/2}$, where r_b is the beam radius, I_b is the beam current, I_A is the Alfven current, $I_A = (m_e c^3/e)\beta_z \gamma = 1.7 \times 10^4 \beta_z \gamma$ amps, β_z is the beam velocity in the z direction normalized to the speed of light, and $\gamma = (1-\beta^2)^{-1/2}$. Using $r_b = 1.35$ cm, $E_b = 30$ kV, and $I_b = 1.5$ A, we obtain $I_A = 5.9 \times 10^3$ A and $k_\beta^{-1} = 60$ cm. This order-of-magnitude estimate is consistent with the beam propagation distance through the waveguide plasma (~14 cm), especially because this estimate does not include nonlinear effects that may account for the shorter measured pinch distance. If the beam current is adjusted to a value that is slightly below the Bennett-pinch threshold, we observe a temporal collapse in the radial beam profile, as shown in Figure 9. In this case, the initially broad, inverted profile evolves toward the pinched-beam condition over a period of 10 μs.

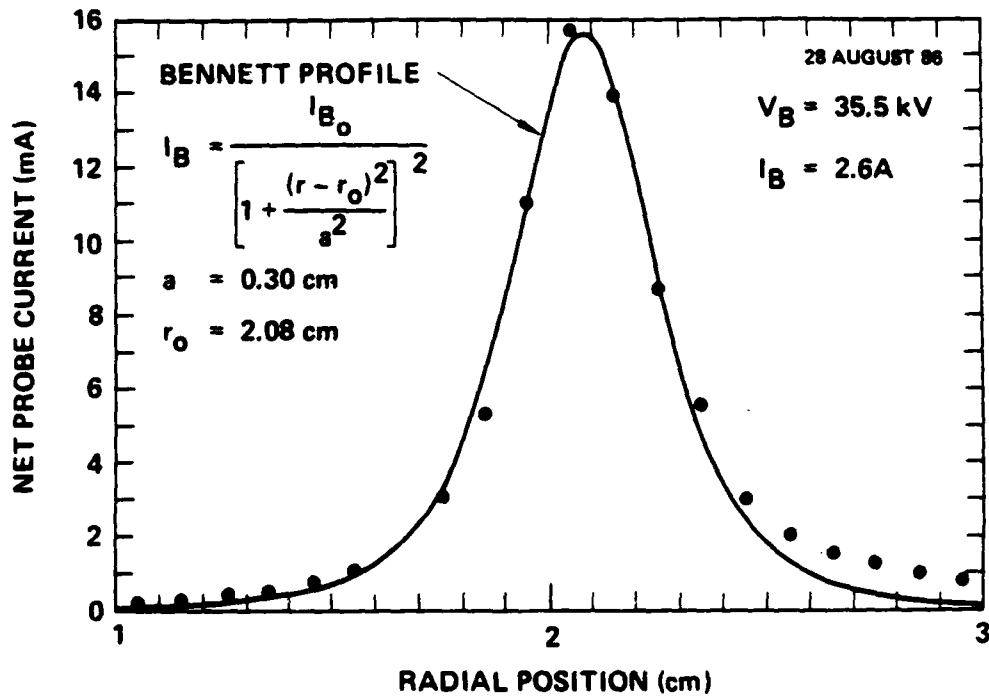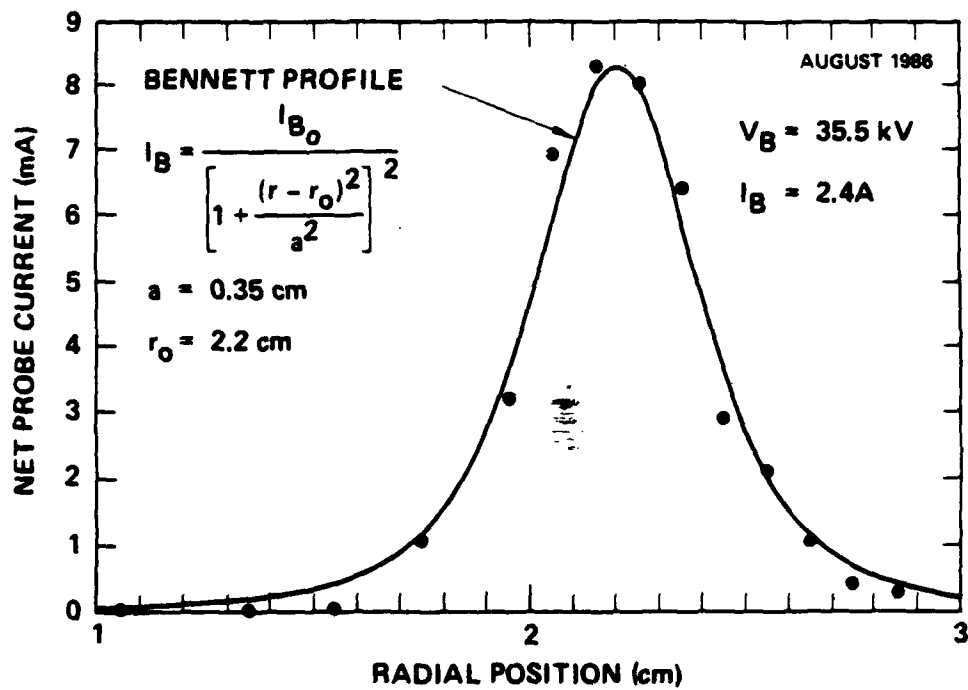Figure 7.   Radial beam profile at s = 15 cm,
n_e = 2x10^{11} cm^{-3}.

Figure 8. Radial beam profile at s = 15 cm, $n_e = 5 \times 10^{12}$ cm^{-3}.
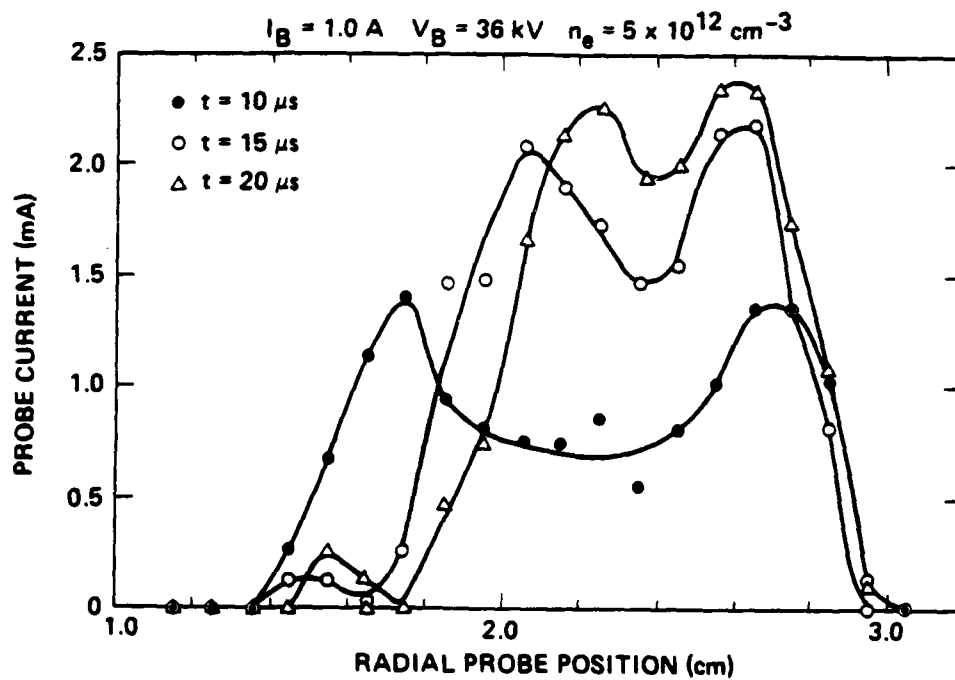
Figure 9. Temporal beam-profile evolution at low current.

The pinching of the E-beams enhances the $2\omega_p$ radiation power. When the beam pinches, the local beam density n_b increases. This, in turn, reduces the EPW growth distance, which is proportional to $(n_b/n_e)^{1/3}$. For the measurements described above, a reduction in the beam diameter from 2.7 to 0.45 cm and the accompanying increase in beam density by a factor of ~8 would result in a reduction in the growth distance by a factor of 2. The EPW temporal growth would change by the same factor because it also scales as $(n_b/n_e)^{1/3}$. With the higher pinched-beam density, the waves can grow at a faster rate, and thereby reach larger amplitudes more quickly.

The effect of the Bennett pinch is also evident in the scaling of radiation power with total beam current. This will be discussed in Section 5, where the radiation characteristics are presented.
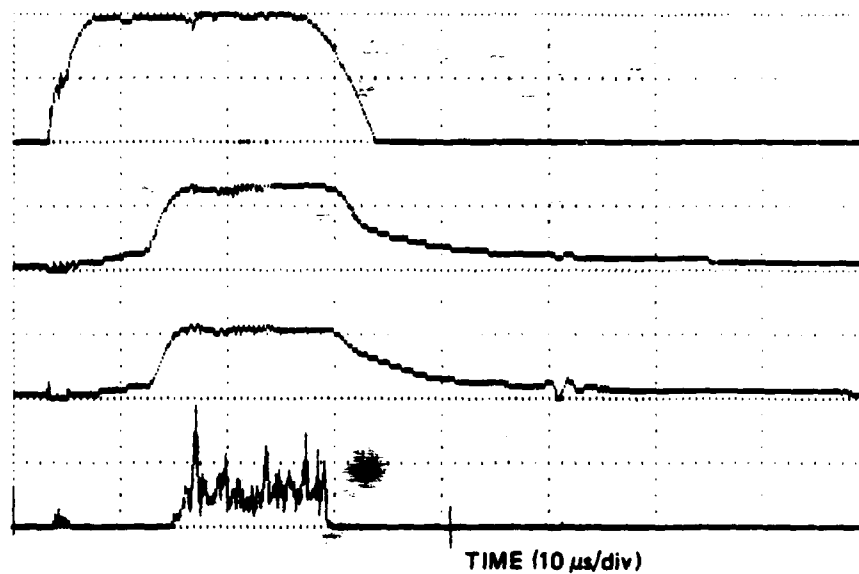
SECTION 5

RADIATION CHARACTERISTICS AND POWER SCALING

Microwave and millimeter-wave radiation is observed when two counterstreaming E-beams are injected into a plasma-loaded waveguide, without the presence of background radiation from the discharge plasma. Employing the detection techniques shown in Figure 4, we observed radiation at frequencies up to 60 GHz when the plasma discharge current was raised to 800 A. As shown in Figure 10, 60-GHz radiation is observed over a 13-μs period within the envelope of the E-beam pulses, which overlap the plasma-discharge pulse. Note that no background radiation is observed from the plasma discharge before the beams are injected.

A high-density discharge and simultaneous injection of both beams are required to generate the millimeter-wave radiation. As shown in Figure 11, no radiation is observed when only one of the two beams is injected into the plasma. This is observed for current values up to the maximum single-E-beam current of 6 A. This implies that the single beam is not sufficiently intense to produce backscattered EPWs via parametric decay (which would set up a counterpropagating EPW topology with only a single E-beam). The requirement of simultaneous beam injection is demonstrated by delaying the injection of one beam relative to the other (see Figure 12). Radiation at 50 GHz is observed only when the beams overlap in time. From Figure 12 we can also conclude that there is a beam-current threshold for detectable radiation. Radiation is not observed during the early portion of the LV E-beam pulse, even though the HV E-beam current is ~0.5 A. However, radiation is emitted when the HV beam current is increased to 2 A.

The data in Figure 13 demonstrate that the radiation frequency is controlled by the waveguide plasma density. The 36-GHz radiation, which is observed when the waveguide discharge is on, disappears when both beams are injected without the high-density waveguide discharge. However, even in the absence of a waveguide discharge, low-density (2×10^{11} cm^{-3}) plasma from the

16101—10

PRESSURE = 65 mTorr He

PLASMA DISCHARGE
400 A/div

HV E-BEAM
2A/div

LV E-BEAM
2A/div

60-GHz
RADIATION

TIME (10 μs/div)

|←— PLASMA PULSE —→|

|←— BEAM —→|
    PULSES

Figure 10.   Radiation at 60 GHz is generated by the beam-
             plasma system when counterstreaming beams are
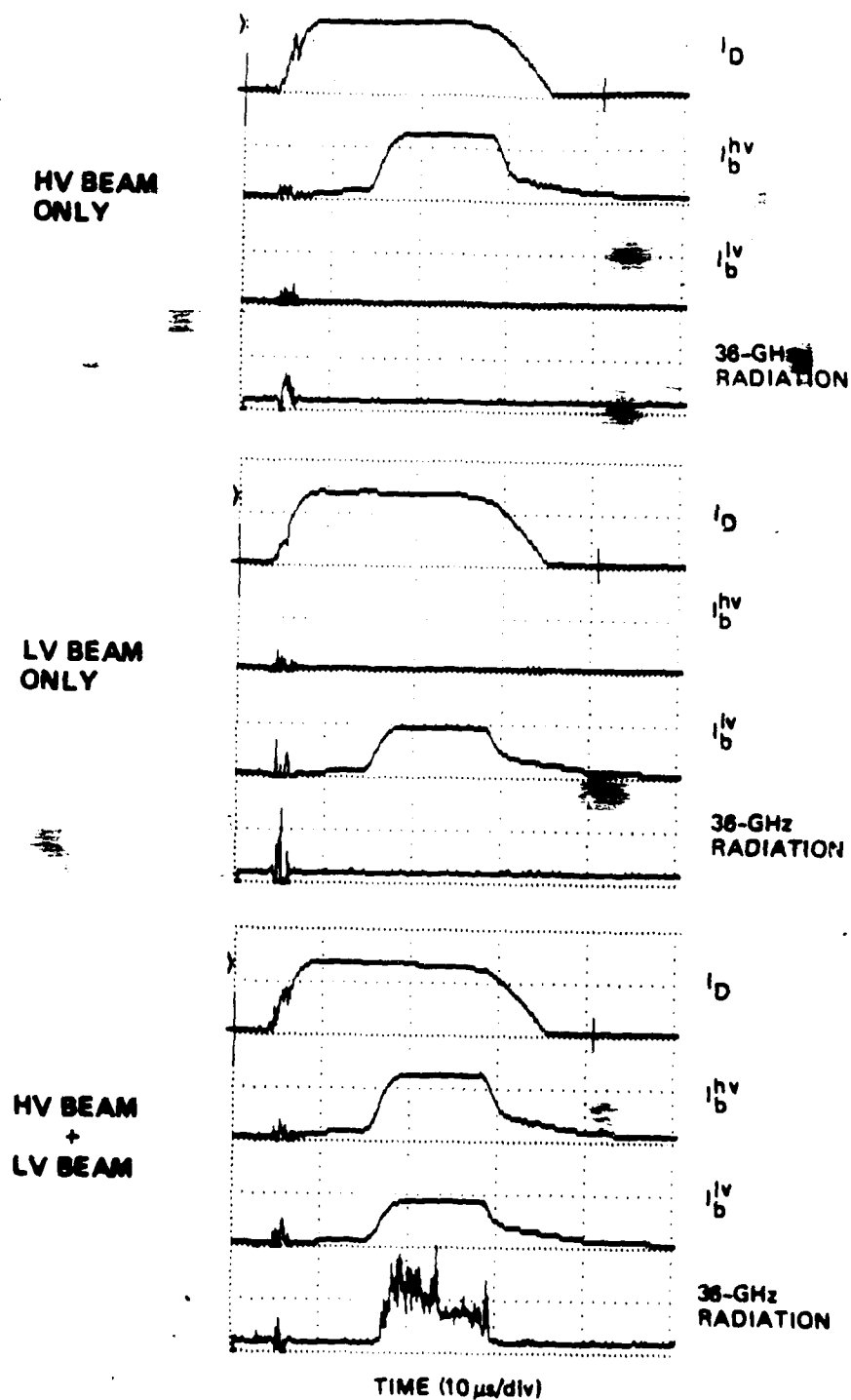   injected into the plasma-loaded waveguide.

A-30

HV BEAM
ONLY

I_D

I_b^{hv}

I_b^{lv}

36-GHz
RADIATION

LV BEAM
ONLY

I_D

I_b^{hv}

I_b^{lv}

36-GHz
RADIATION

HV BEAM
+
LV BEAM

I_D

I_b^{hv}

I_b^{lv}

36-GHz
RADIATION

TIME (10 μs/div)

Figure 11. Simultaneous injection of both beams is required to generate mm-wave radiation. No radiation is observed when only one beam is used.

A-31

PRESSURE = 50 mTorr He

PLASMA DISCHARGE
400 A/div
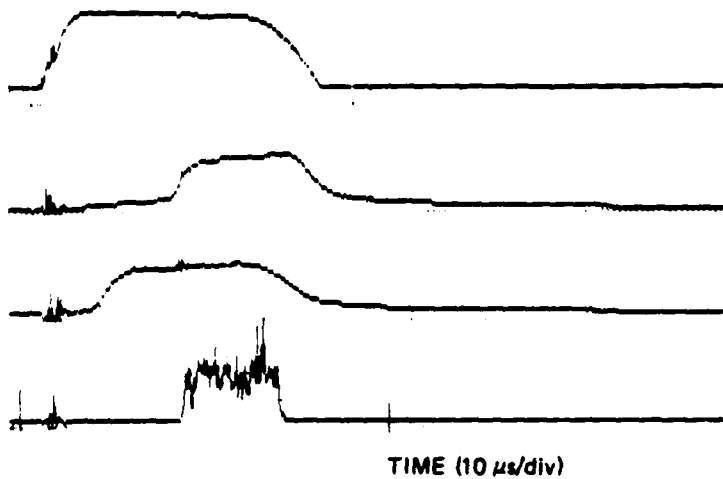
HV E-BEAM
2 A/div

LV E-BEAM
2 A/div

50-GHz
RADIATION

TIME (10 μs/div)

Figure 12.   Radiation at 50 GHz is observed only
when the two beam pulses overlap in time.

PLASMA DISCHARGE I_D

\+

HV BEAM I_b^{hv}

\+

LV BEAM I_b^{lv}

36-GHz
RADIATION

NO DISCHARGE I_D

HV BEAM I_b^{hv}

\+

LV BEAM I_b^{lv}

36-GHz
RADIATION

NO DISCHARGE I_D

HV BEAM I_b^{hv}

\+

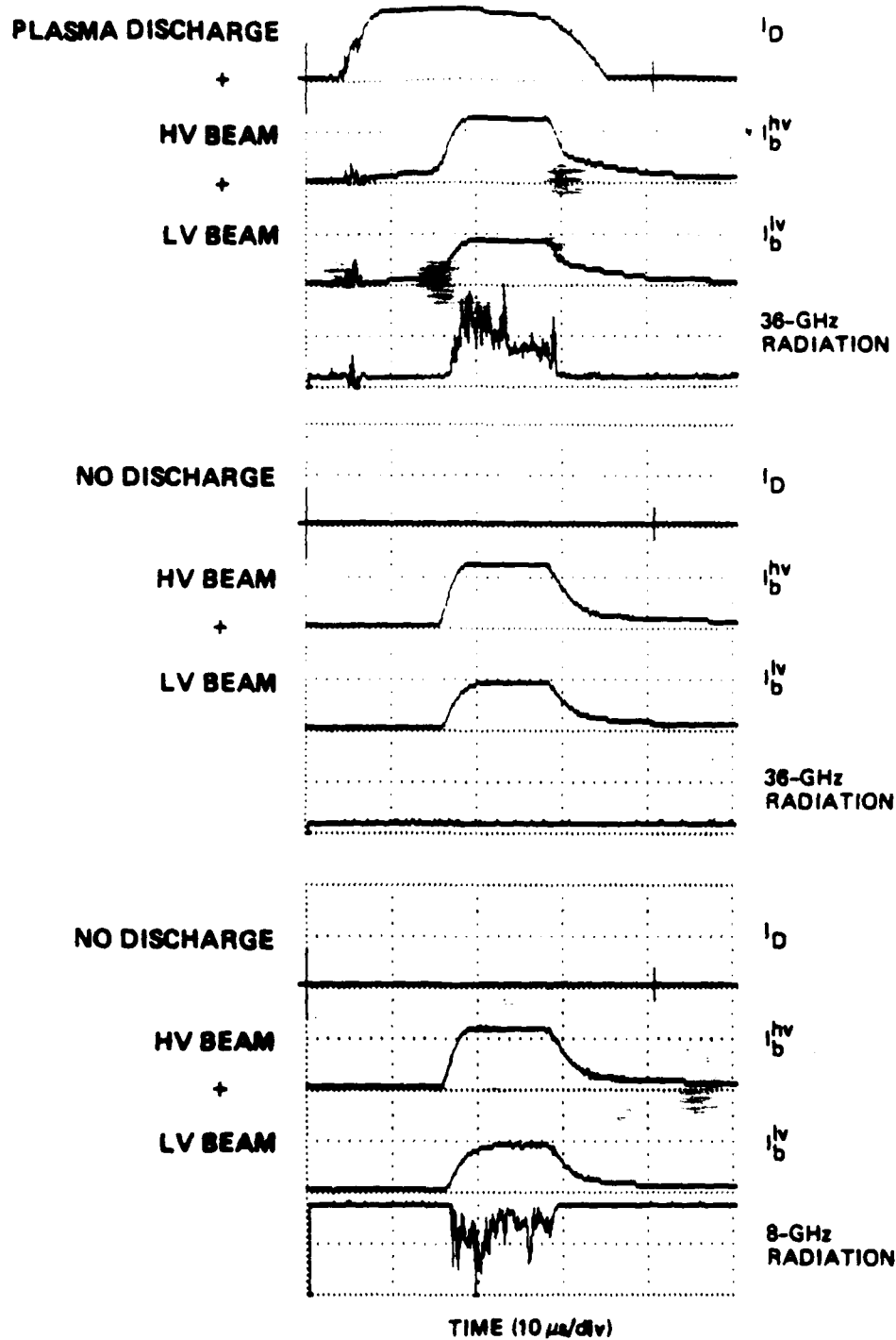LV BEAM I_b^{lv}

8-GHz
RADIATION

TIME (10 μs/div)

Figure 13.   Output radiation shifts to low frequency
when both beams are injected without the
high-density waveguide discharge.

A-33

E-gun wire-anode discharges and the beams partially fills the waveguide. As shown in the lower pulse sequence in Figure 13, radiation is observed at ~8 GHz, which is associated with twice the low-density plasma frequency.

The radiation produced in this experiment is strongly amplitude modulated. The radiation is emitted as bursts with inter-pulse periods (IPPs) and pulse widths that depend on the background gas species. As shown in Figure 14, the radiation is strongly modulated on a time scale that is near the ion-plasma frequency - behavior which is also characteristic of nonlinear beam-plasma instabilities. Figure 14 shows that the radiation at 35 GHz is emitted in random spikes with half-widths of ~10 ns. The spikes could be even narrower because the bandwidth limit of the oscilloscope was 100 MHz.

The millimeter-wave modulation frequency decreases as the ion mass is increased. Oscilloscope photos of the crystal detector outputs for five different gases (i.e., hydrogen, helium, argon, krypton, and xenon) are shown in Figure 15. These data are reduced to a quantitative form in Figure 16, where the modulation IPP and pulse width are plotted versus ion mass. The parameters scale approximately with the square root of the ion mass. These data clearly indicate that ion dynamics is important in determining the characteristics of the radiation. The modulation could be caused by ion acoustic waves that are known to be generated by parametric-decay instabilities in strong-EPW-turbulent systems. Using the beam-plasma parameters listed in Figure 14, together with Eq. (8), we estimate the ratio of EPW energy density to plasma energy density, W_{EPW}/n_eT_e, to be about 7×10^{-2}. The beam-plasma interaction in the experiment is strongly turbulent, because this ratio exceeds the weak turbulence parameter $(k_e \lambda_D)^2$ by 3 orders of magnitude.

We investigated the radiation modulation as a function of waveguide plasma density and beam current. Figure 17 shows the change in the modulation of 36-GHz radiation (filter pass-band = 35 to 37 GHz) as the waveguide plasma density is raised by increasing the discharge current by 50%. At 230 A, the radiation
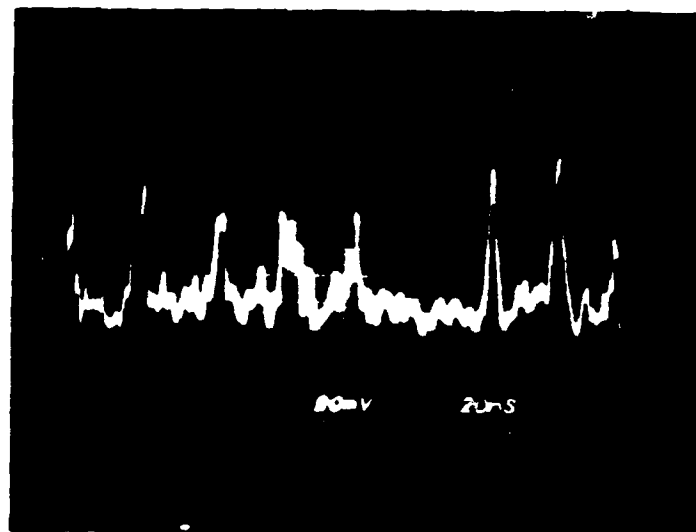
35-GHz
RADIATION

TIME (40 ns/div)

$n_e = 3.8 \times 10^{12}$ cm^{-3}

$T_e = 5$ eV

$I_b = 2.5$ A

$V_b = 30$ kV

$\dfrac{n_b}{n_e} \cong 2.3 \times 10^{-4}$

$\dfrac{W_{EPW}}{n_e T_e} \cong 7 \times 10^{-2}$

$(k_p \lambda_D)^2 \cong 8 \times 10^{-5}$

Figure 14.   Output mm-wave radiation is strongly
modulated on a time scale which is near
the ion-plasma frequency. Experiment
parameters corresponding to the observed
35-GHz radiation are listed below the
oscilloscope waveform.

A-35

HYDROGEN

KRYPTON

XENON

HELIUM

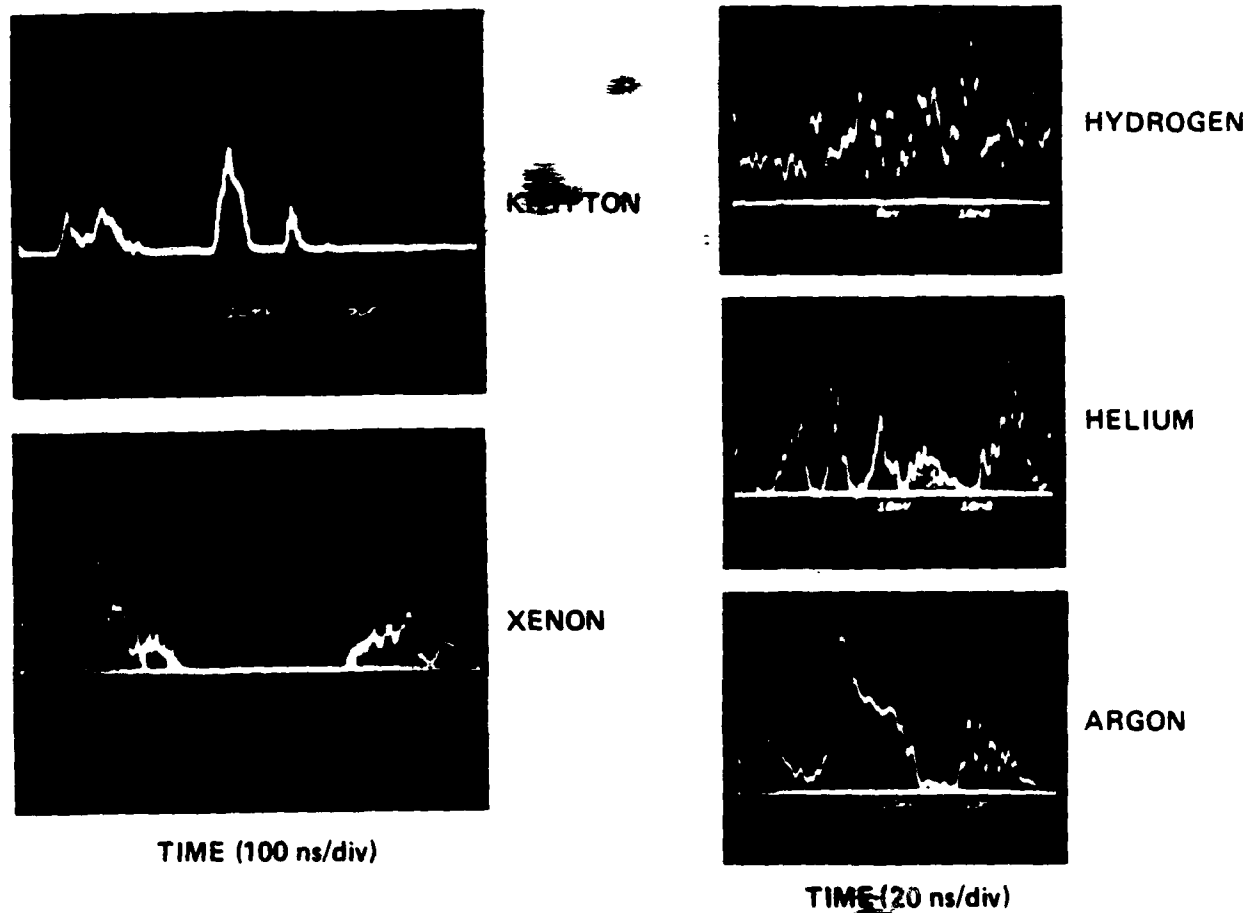ARGON

TIME (100 ns/div)

TIME (20 ns/div)

Figure 15. Millimeter-wave modulation frequency
decreases with ion mass.
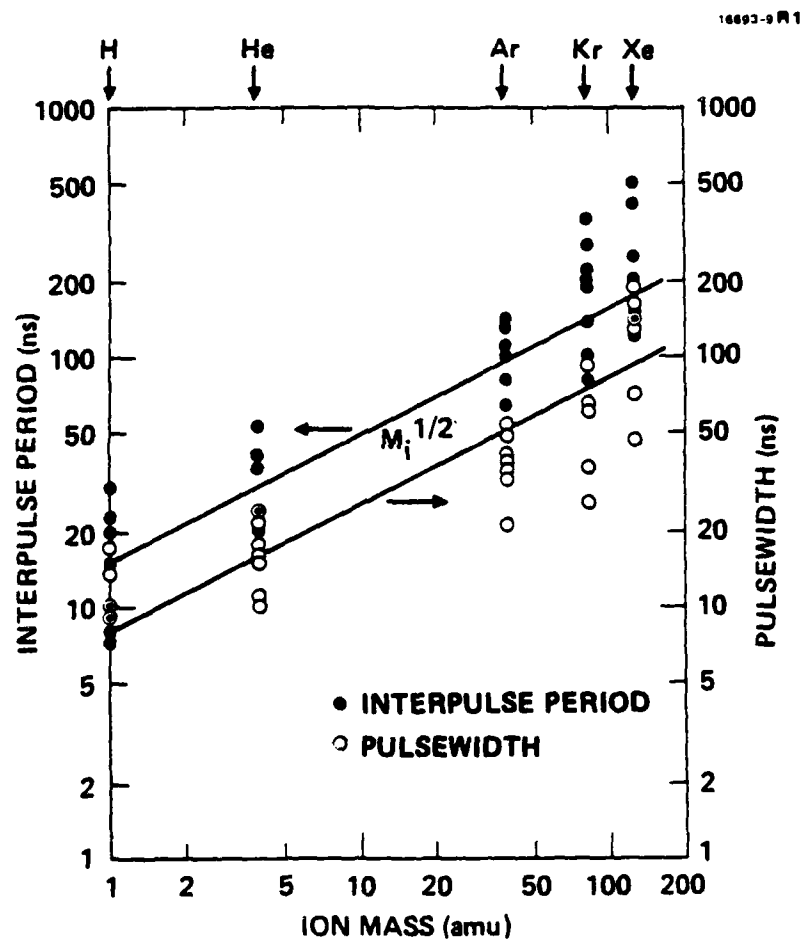
Figure 16.   Millimeter-wave pulsewidth and
interpulse-period scale as $M_i^{1/2}$.

$I_D = 310$ A

Ka-BAND
RADIATION

10 mV/div

TIME (200 ns/div)

$I_D = 230$ A

Ka-BAND
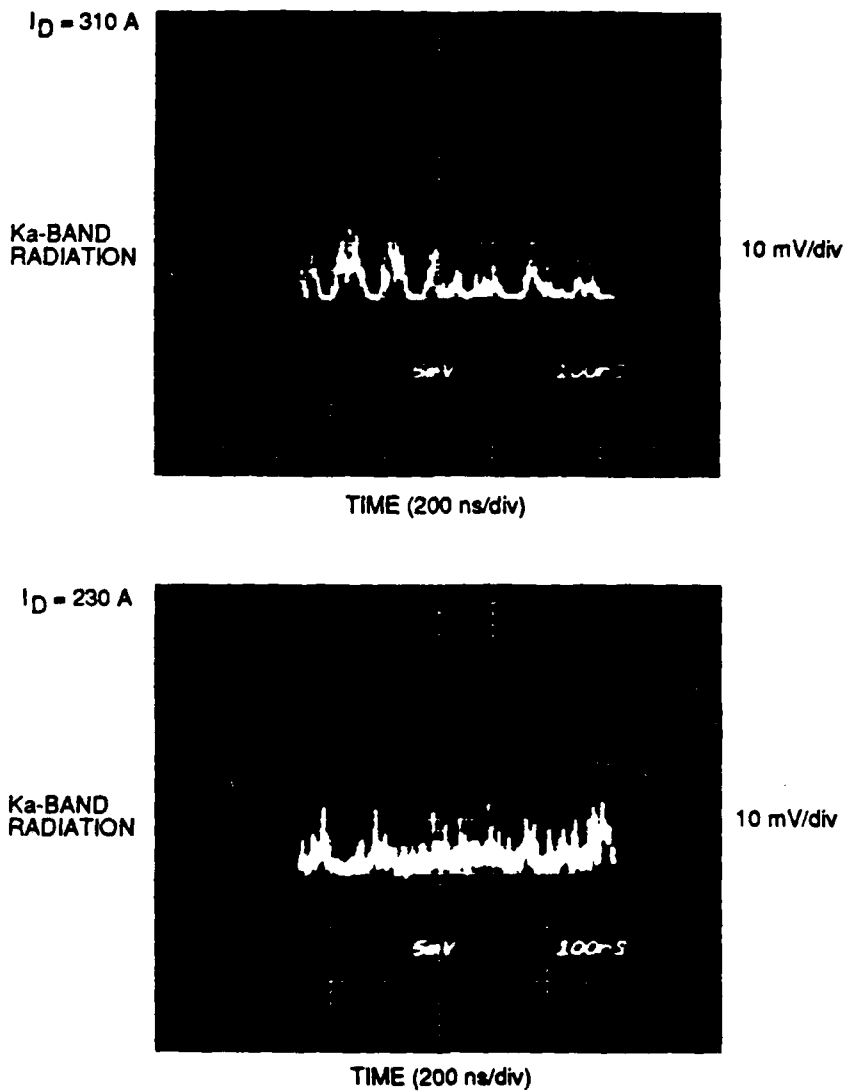RADIATION

10 mV/div

TIME (200 ns/div)

Figure 17. The modulation of Ka-band radiation is
dependent on the waveguide discharge
current. The total beam current was
5 A and the beam voltage was 30 kV.

A-38

consists of many very narrow width (5 to 25 ns wide) spikes with a short IPP of about 10 to 50 ns. The radiation is emitted continuously and we do not observe periods when the radiation power drops to zero. However, when the discharge current is increased to 310 A, the bursts become wider (50 to 100 ns), the IPP increases to 100 to 200 ns, and the signal amplitude between bursts is low compared with the peak amplitude. The radiation has changed from a nearly continuous radiation emission process at low discharge current, to a more ordered, burst emission at high discharge current.

These characteristics are also exhibited at higher discharge currents. Figure 18 compares the Ka-band emission measured with waveguide discharge currents equal to 500 and 200 A, respectively. In this experiment, the bandpass filter was not used. At 500 A, the emission is concentrated in a series of bursts and the signal amplitude between bursts is very low. When the discharge current is reduced to 200 A, the radiation power drops by about 14 dB and the bursts are replaced by narrow, high-frequency pulses.

The modulation also depends on beam current. The data shown in Figure 19 for three different $I_B{}^{LV}$ values was recorded while the HV beam current was held constant at 2.6 A. At $I_B{}^{LV} = 2.5$ A, the emission consists of 50-ns-wide bursts and the IPP is 50 to 200 ns. When $I_B{}^{LV}$ is reduced to 1.8 A, the radiation drops in power by about 16 dB, and is generated in burst clusters, with very little power emitted between bursts.

When $I_B{}^{LV}$ is set to zero, but with the beam voltage applied to the LV beam cathode, we still detect radiation. This occurs because electrons from the HV beam reach the LV cathode and some of the beam electrons are reflected into the waveguide plasma. The reflected electrons then excite EPWs, resulting in radiation emission. When the LV beam cathode is grounded so HV beam electrons traverse the waveguide plasma only one time, radiation is not detected.
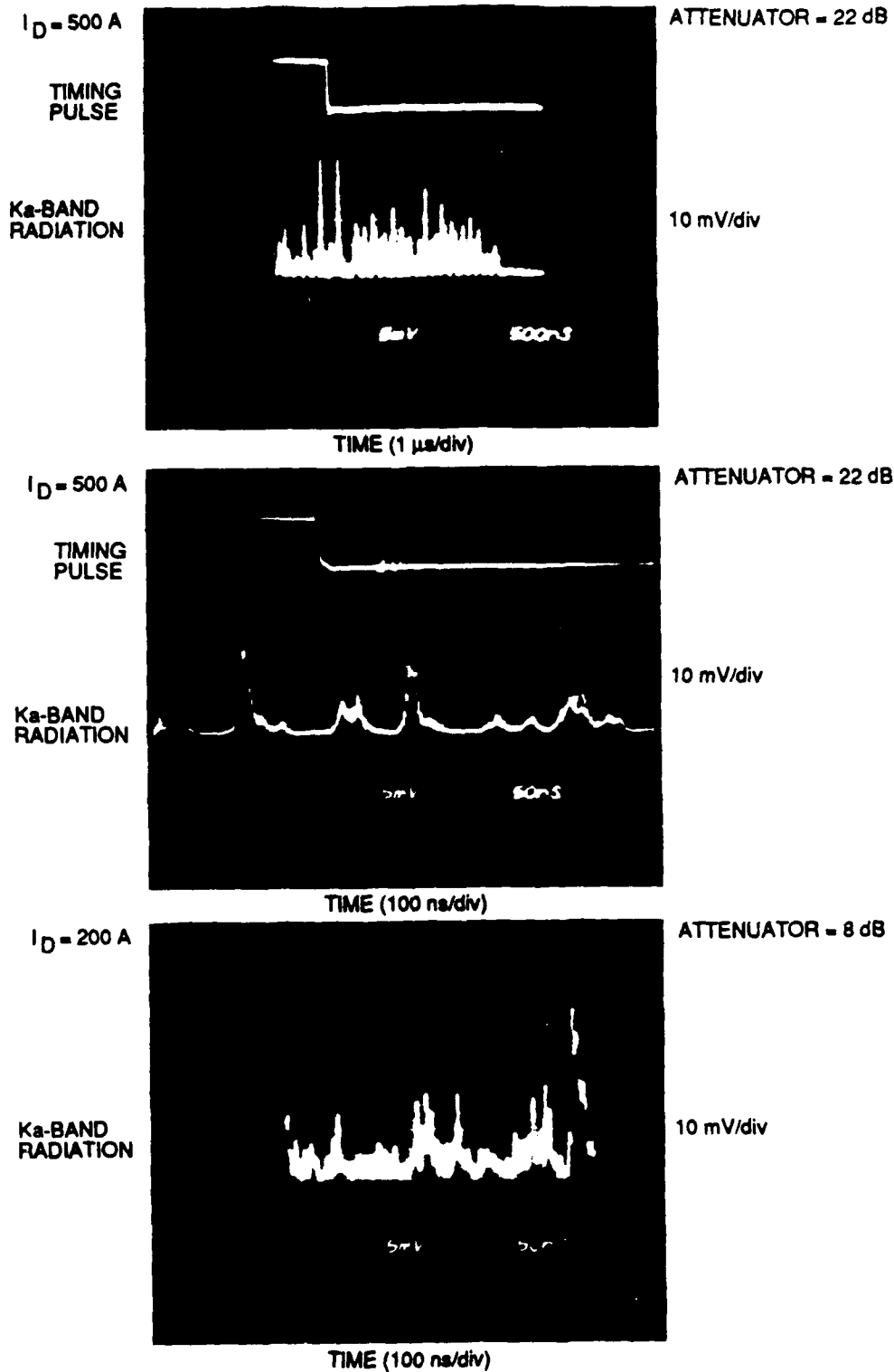
18206-3

$I_D = 500 \text{ A}$ ATTENUATOR = 22 dB

TIMING
PULSE

Ka-BAND
RADIATION   10 mV/div

TIME (1 µs/div)
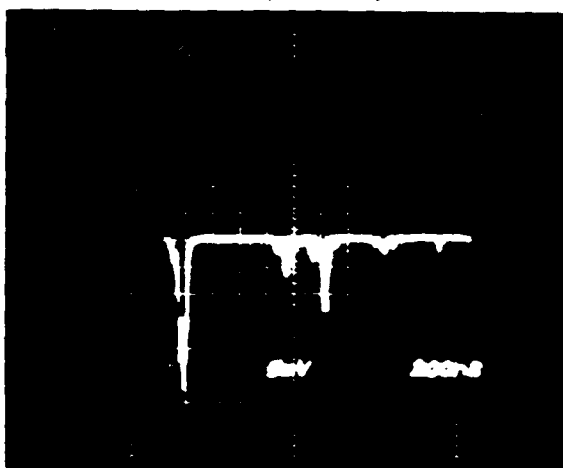
$I_D = 500 \text{ A}$ ATTENUATOR = 22 dB

TIMING
PULSE

Ka-BAND
RADIATION   10 mV/div

TIME (100 ns/div)

$I_D = 200 \text{ A}$ ATTENUATOR = 8 dB

Ka-BAND
RADIATION   10 mV/div

TIME (100 ns/div)

Figure 18.   The Ka-band radiation is strongly modulated for
a waveguide discharge current of 500 A. When the
discharge current is reduced to 200 A, the
radiation burst width becomes very narrow. The
total beam current was 5 A and the beam voltage
was 30 kV.

A-40

Figure 19. Ka-band modulation IPP depends on the beam current. When the HV beam is on, and $I_b^{LV} = 0$, but the LV cathode is biased to reflect the HV beam electrons back into the plasma, radiation is still observed. The HV beam current was held constant at 2.6 A, the beam voltage was 20 kV and the waveguide discharge current was 500 A.

A-41

Scaling of the millimeter-wave frequency with waveguide discharge current and plasma density was measured by varying the discharge current from 15 to 800 A and observing the output radiation with an array of waveguide bandpass and high-pass filters. The output of the filters is plotted in Figure 20 as a function of the waveguide discharge current from 200 to 800 A. The data indicate that the center frequency of the radiation increases as the discharge current is increased. By noting the discharge current value at which millimeter-wave power is received in each filter, we can determine the scaling of frequency with discharge current.

We performed this scaling experiment at low discharge current and low helium-gas pressure, and with reduced E-gun wire-anode and beam current in order to minimize plasma production in the waveguide by the guns and beams. The scaling of radiation frequency versus discharge current presented in Figure 21 shows a good fit to $I_0^{1/2}$ scaling. This is expected with low gas pressure because the discharge voltage remains constant as the discharge current is increased; under these conditions $n_e \propto I_d$ and $\omega_p \propto I_d^{1/2}$. As shown in Figure 22, the millimeter-wave frequency scales as twice the waveguide plasma frequency, as predicted by the three-wave-mixing theory.

To further investigate the scaling of the radiation frequency with discharge current, we repeated the experiment using lower gas pressure, higher discharge current, and a 9.5-cm-diameter waveguide section. As shown in Figure 23, the radiation frequency scaled as $I_d^{1/2}$, as predicted from the argument presented above.

We have investigated the scaling of radiation power with E-beam voltage. This experiment was performed by holding the first E-beam voltage constant at 19.5 kV, and scanning the second E-beam voltage over a broad range while simultaneously observing the output radiation power at 35 GHz. To reduce the effects of shot-to-shot variations, and the radiation power variations within a single pulse (i.e., amplitude modulation described previously) we used an RC circuit to integrate the total power in
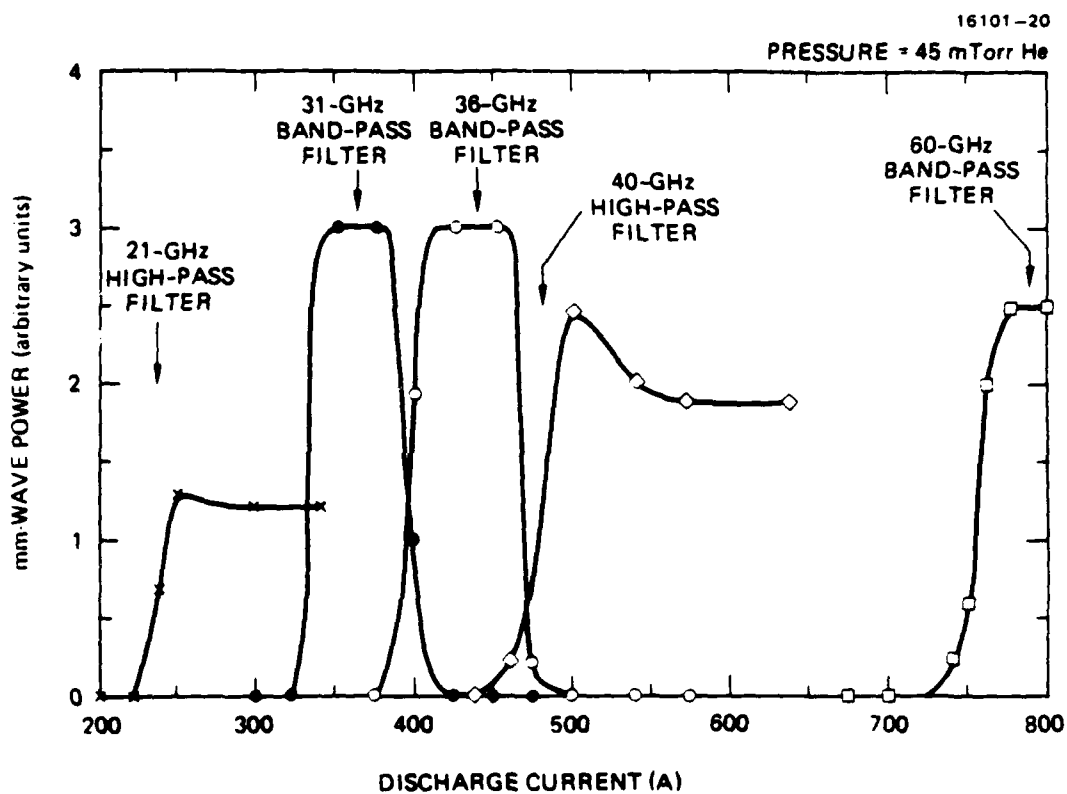
Figure 20.   Frequency scaling with waveguide discharge
current is determined by observing the mm-wave
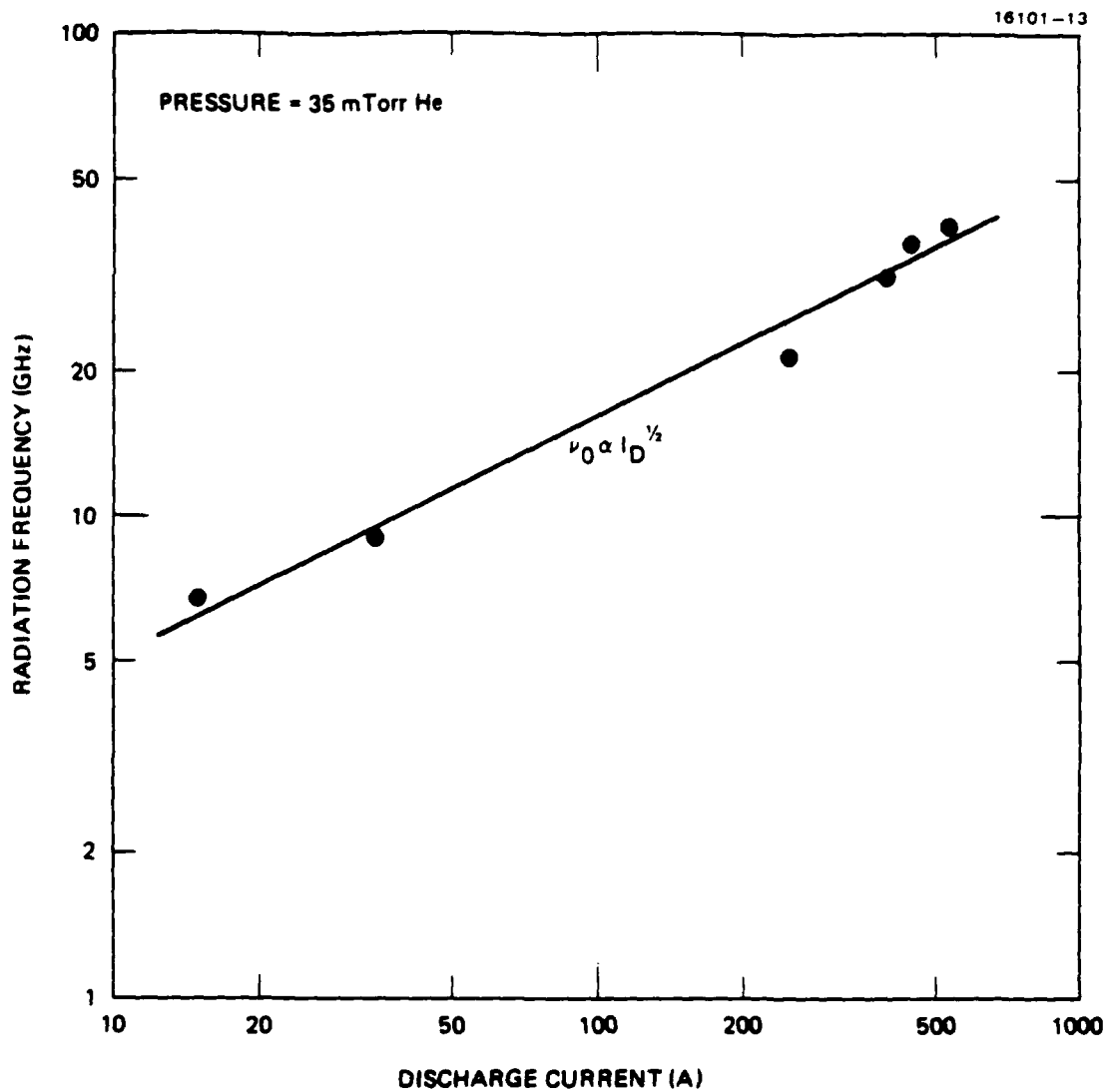output with an array of waveguide high-pass
and band-pass filters.

100 ─
PRESSURE = 35 mTorr He

50 ─

RADIATION FREQUENCY (GHz)

$\nu_0 \alpha \, I_D{}^{\frac{1}{2}}$

20 ─

10 ─

5 ─

2 ─

1 ─
10   20   50   100   200   500   1000

DISCHARGE CURRENT (A)

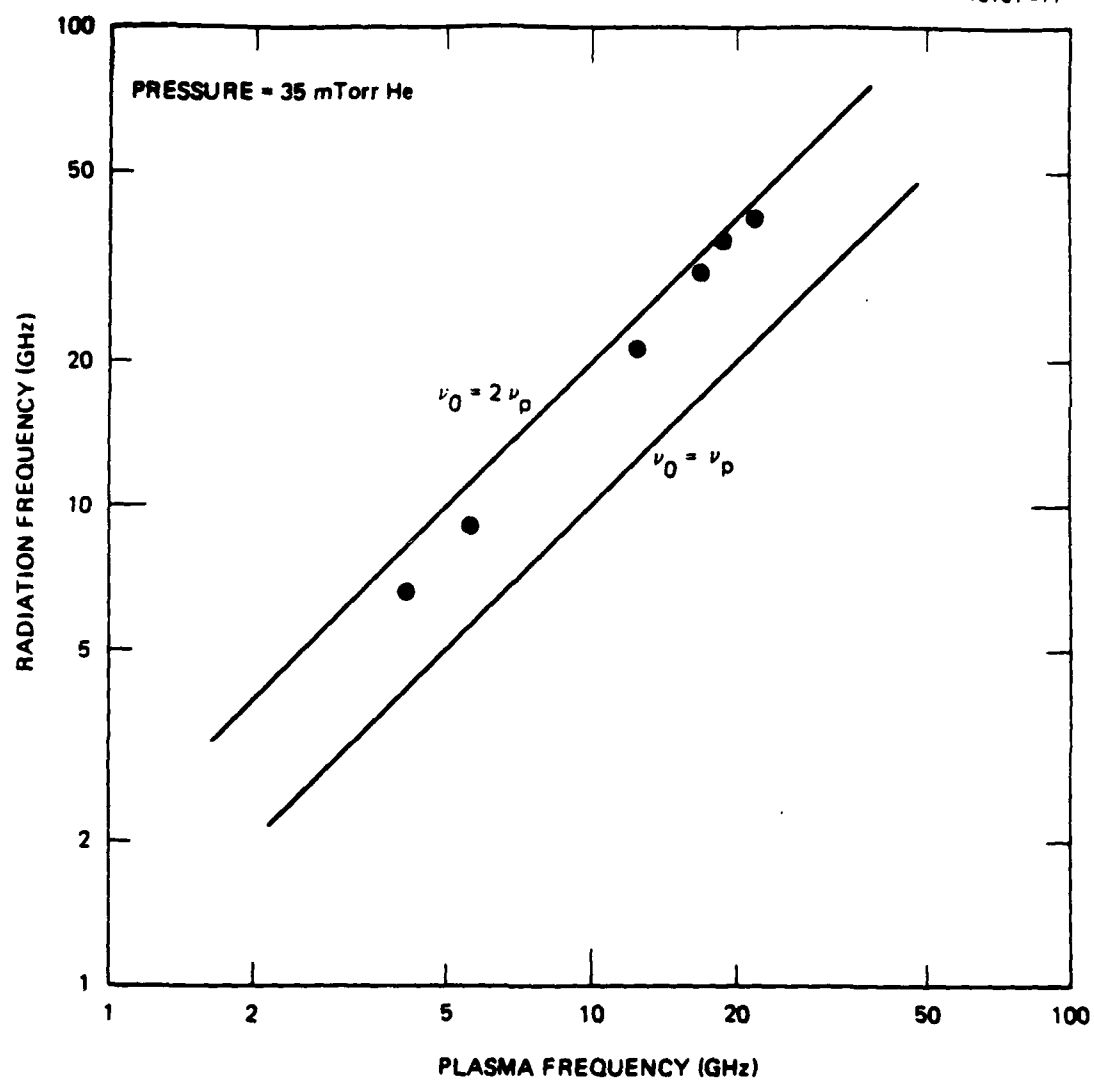Figure 21.   Frequency scaling with discharge current.

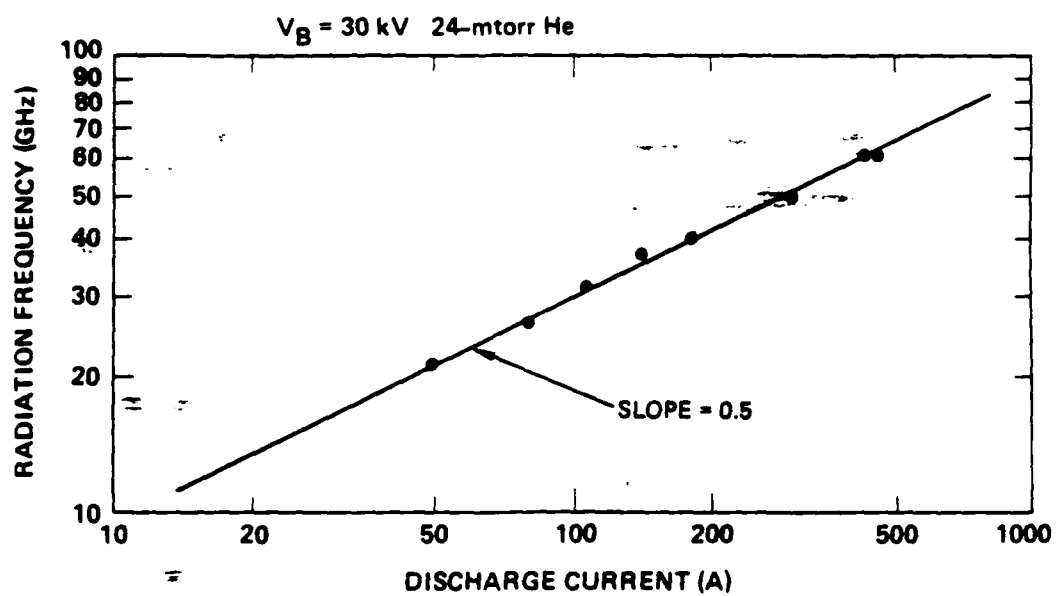Figure 22. Output frequency scales as $2\nu_p$.

A-45

Figure 23. Radiation frequency scales as $I_0^{1/2}$.

each shot, and this number was then averaged over ten successive shots using the computer. The results are plotted in Figure 24 for total cathode currents (sum of both E-beams) of 2.8, 3.0, 4.1, 5.6, 7.4, and 8.5 A (the cathode current in each gun is roughly twice the injected current in each beam). At the lowest current, radiation is detected only for $V_b^{LV} = V_b^{HV}$. As the beam current is increased, the beam-voltage "tuning" envelope broadens and suggests the generation of a broad spread of EPW wave numbers at high beam current. In general, however, Figure 24 shows that the radiation is optimized for almost equal beam voltages. These data contrast sharply with the solutions presented earlier, which predicted that the TM_{01} mode would be excited at $V_b^{HV} = 65$ kV for $V_b^{LV} = 18.8$ kV and $\nu_0 = 35$ GHz. Apparently, the beams are exciting higher order TM modes near the cutoff frequency of the plasma-loaded guide where $k_e \simeq 0$ and where Eq. (15) requires $V_b^{LV} = V_b^{HV}$.

Figure 25 is a comparison of voltage tuning curves at high beam currents with $V_b^{LV} = 20$ and 30 kV. The curves nearly overlap, indicating that a substantial spreading in k-space has occurred; that is, precise beam voltage selection rules are not required because a broad k-spectrum is generated at high beam currents.

We have also set $V_b^{LV} = V_b^{HV}$ and plotted the scaling of millimeter-wave power with beam voltage. The results at 30-GHz output frequency are shown in Figure 26, which indicates an optimum beam voltage of 30 kV. In this case, very little change in the optimum beam voltage setting is noted as the beam current is increased from 3.5 to 5.3 A. We repeated the experiment at higher waveguide plasma density so that the radiation center frequency is at 60 GHz. These data are shown in Figure 27. Note that at higher density and frequency, the optimum beam voltage has shifted to 41 kV.

The observed scaling of millimeter-wave power with beam voltage (Figures 26 and 27) can be explained by considering the EPW profile that is excited by the beams. The main requirement for high power emission is that the EPWs overlap spatially so they can interact to generate the millimeter-wave radiation. In
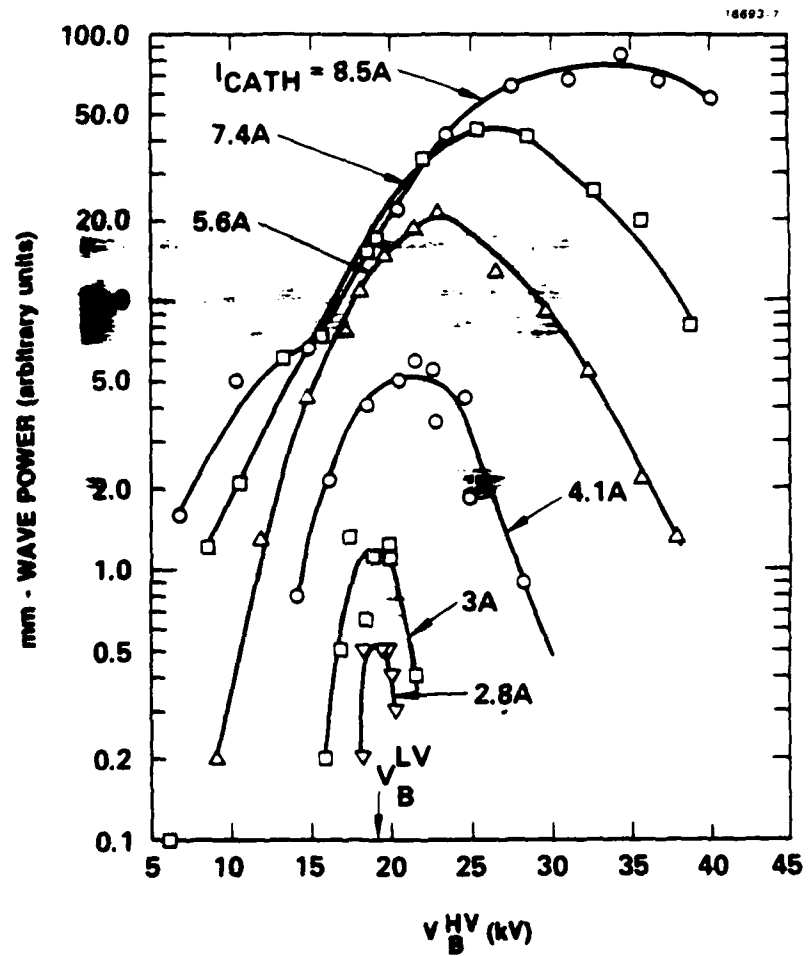
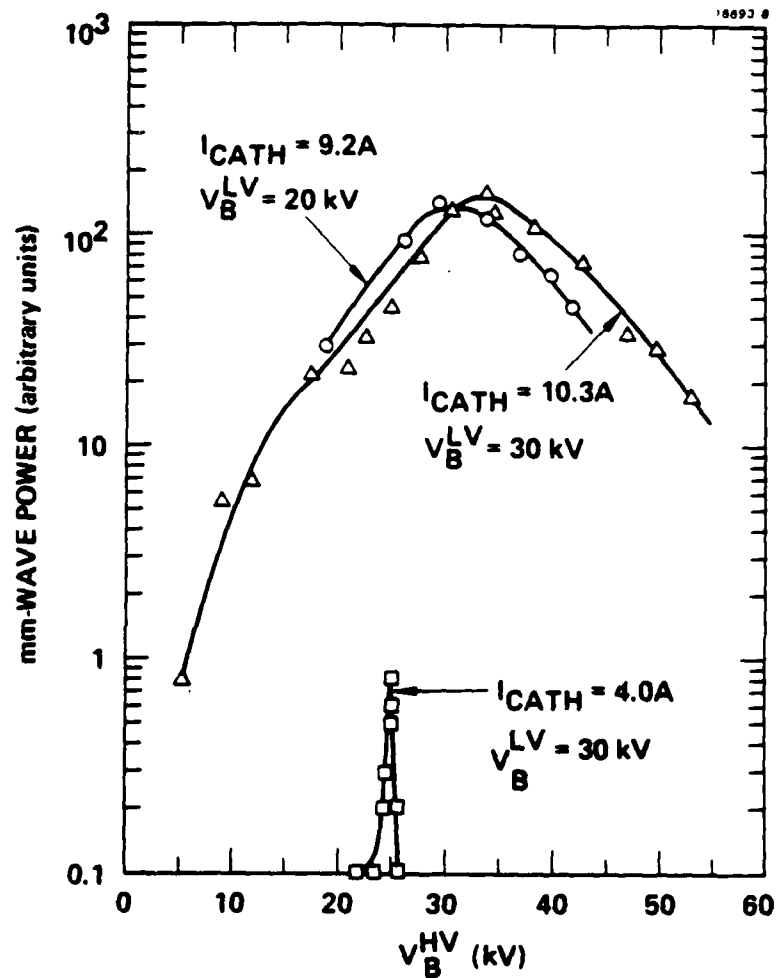Figure 24.   Beam-voltage tuning for V_b^{LV} = 19.5 kV.

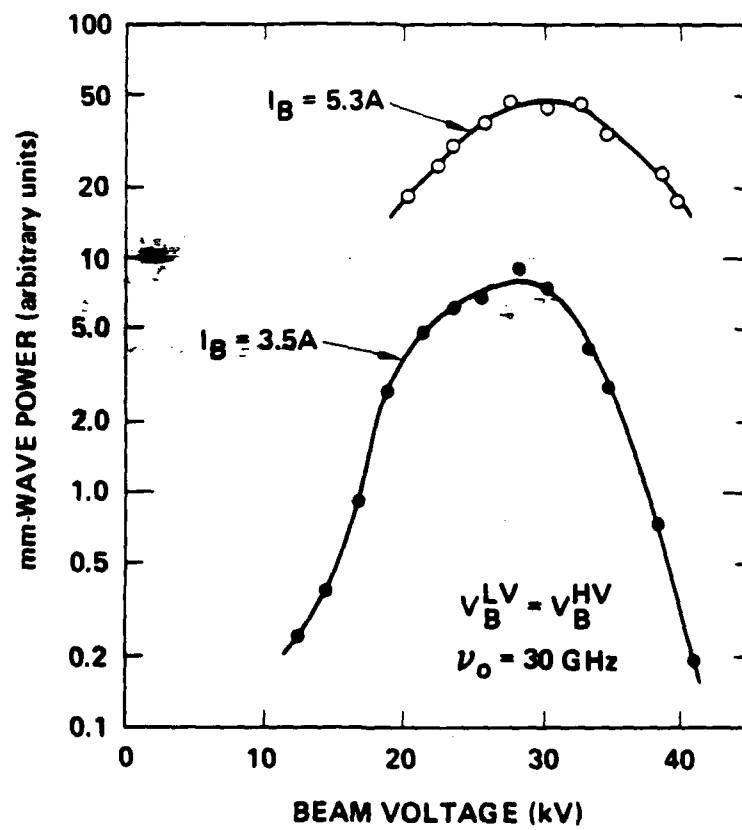Figure 25.   Beam-voltage tuning for $V_B^{LV} = 20$ and 30 kV.

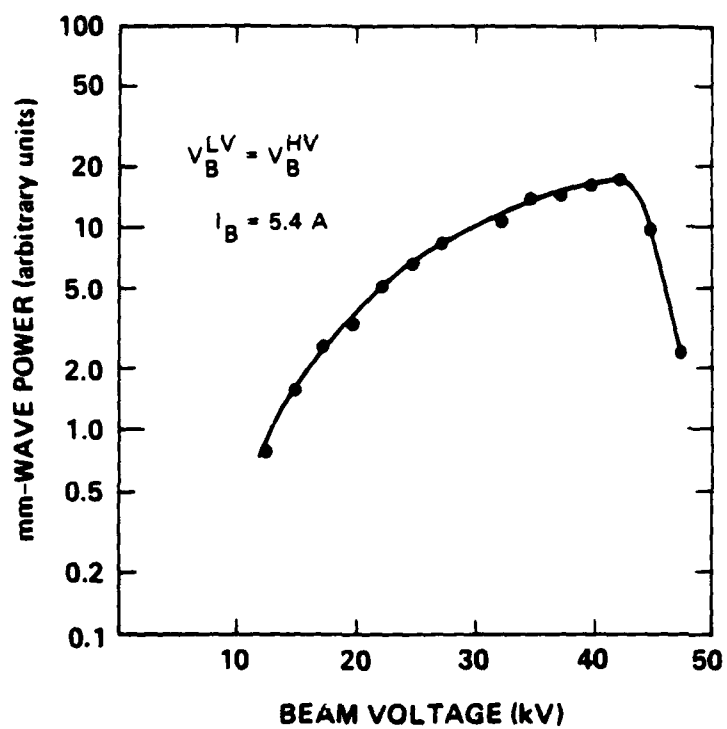Figure 26. Millimeter-wave power scaling with beam voltage.

Figure 27.   Millimeter-wave power scaling
with beam voltage at 60 GHz.

general, the EPW amplitude will grow, saturate, and then decay along the beam direction, as shown schematically in Figure 28. When the beam voltage is too low, the EPWs saturate and decay near the ends of the waveguide before they interact. When the voltage is too high, the EPWs require a long distance before they can grow to large amplitude. The radiation generated under either of these two conditions is less than that which would be obtained if the optimum beam voltage were used. At the optimum voltage the EPWs overlap near the waveguide midplane where they have the largest amplitude.

Radiation power scaling with total beam current (sum of the injected beam currents) is plotted in Figure 29. There are three salient features of the scaling. First, there is a sharp threshold current below which we observe no detectable power. Second, once the threshold current of ~3 A is reached, the power rises rapidly over 2 orders of magnitude. Third, just above 3 A the sharply rising curve shifts to a power scaling that is approximately proportional to I_b^6, where I_b is the sum of the currents from both beams.

The current-threshold effect is controlled by E-beam dynamics. At total beam-current values below 3 A, the current in each beam is below the Bennett-pinch current of 1.5 A. In this regime the beam channel is broad, the beam density is low, the beam-plasma interaction is weak, and the millimeter-wave power is below our detection threshold. When the current in each beam reaches 1.5 A (3.0-A total), the beam rapidly collapses, the beam density increases sharply, the beam-plasma-instability growth rate increases, and the millimeter-wave radiation suddenly rises. Once each beam becomes fully pinched with the Bennett equilibrium profile, the power rises more slowly and we observe the I_b^6 scaling for I_b up to 5 A.

In Figure 30 we have extended the power scaling to higher total beam currents and we have plotted the scaling for different gases including hydrogen, helium, and neon. For each gas species the same current-threshold phenomena is observed. The data also indicate that the power increases with ion mass.
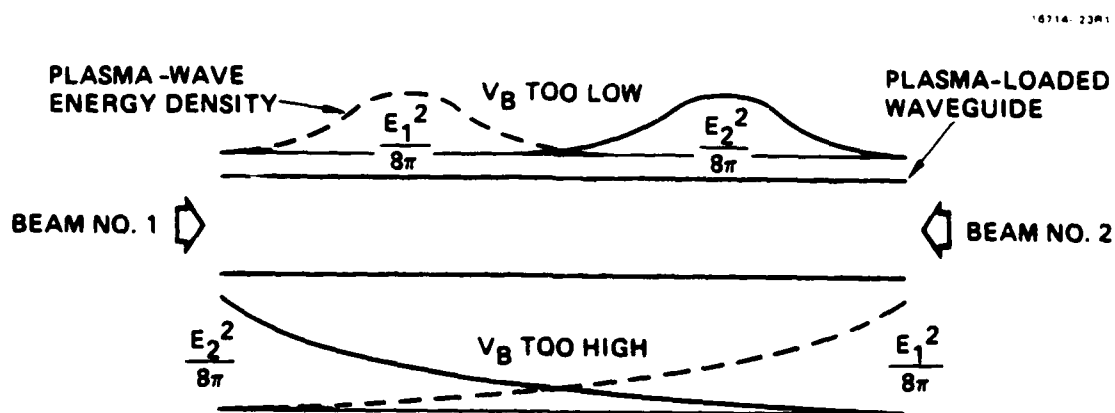
Figure 28. Beam-plasma interaction deposits plasma-wave energy density near the ends of the waveguide when the beam voltages are below or above the optimum value for a given waveguide plasma density. Radiation power is optimized for beam voltages which overlap the envelopes of plasma-wave energy density near the waveguide midplane.
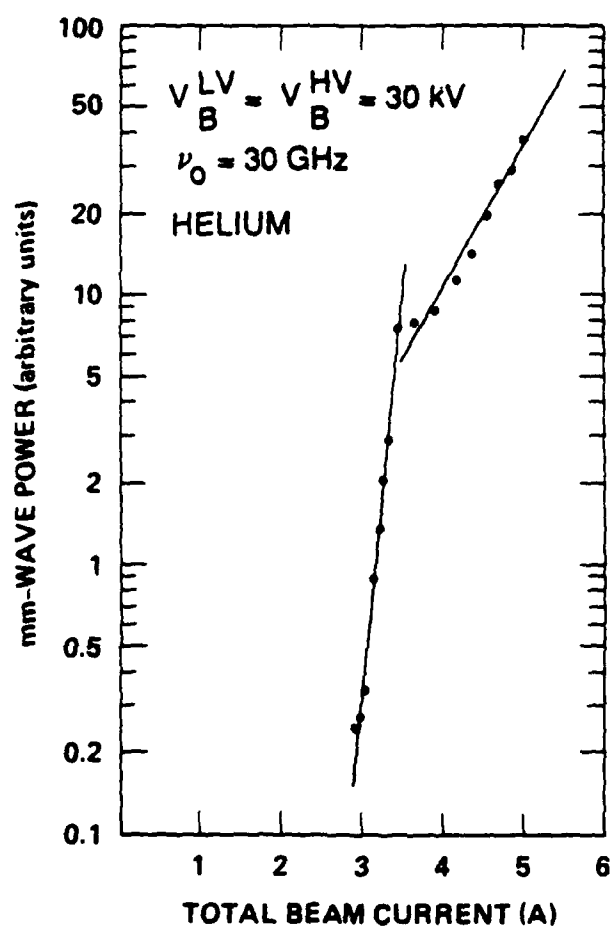
Figure 29. Millimeter-wave power scales
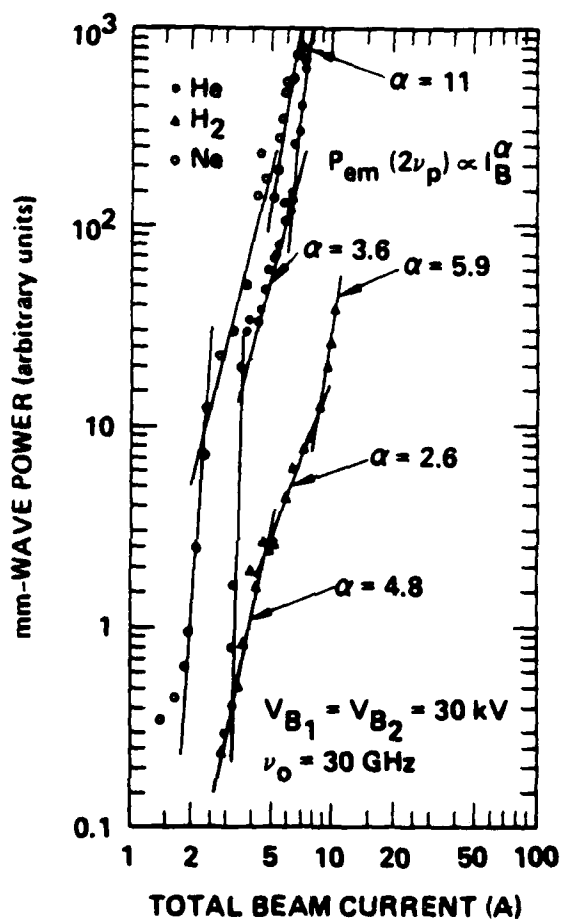nonlinearly with beam current.

A-54

Figure 30. Millimeter-wave power scaling curves for He, H$_2$, and Ne.

The most significant result of this scaling experiment is that at the highest beam currents available, the millimeter-wave power is still increasing rapidly with beam current. At 7 A in helium, for example, we estimate peak power levels of 8 kW at 31 GHz with peak efficiency of 4% within the plasma-loaded waveguide. If the power continues to scale as I_b^6, the efficiency will increase as I_b^5

Because the pinched-beam cross-section is so small, radiation generation should strongly depend on the relative beam positions inside the waveguide. To investigate this issue, we installed beam-steering coils along the waveguide to adjust the radial position of each beam. As shown in Figure 31, we found that a displacement of one beam by 2 mm increased the radiation power by 3 dB. When the beam was displaced by only 1.2 cm, the radiation level fell below our detection threshold. This simple experiment dramatically demonstrates that beam dynamics play a dominant role in the plasma three-wave mixing process.
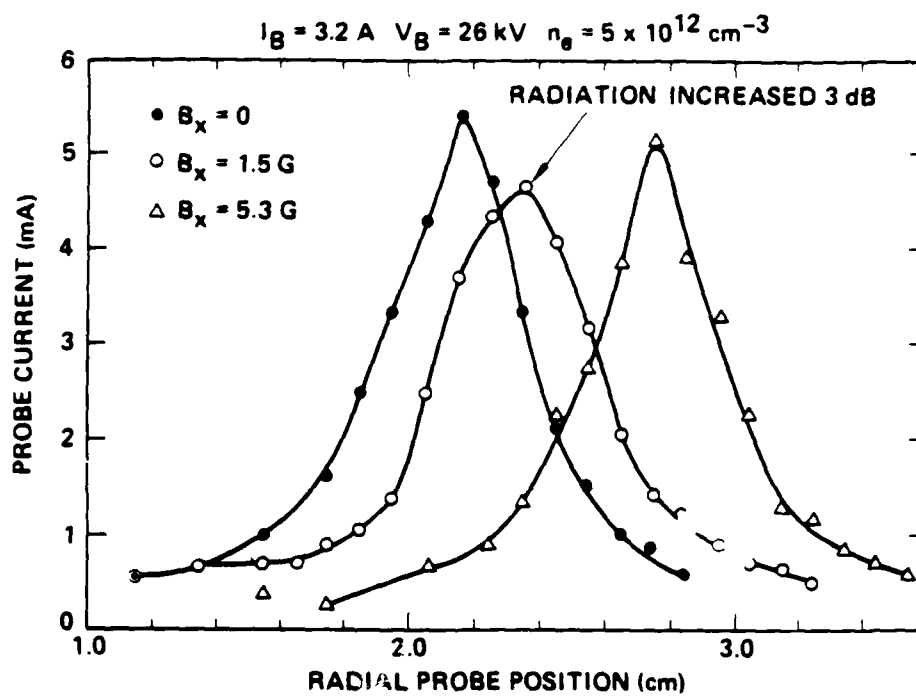
Figure 31. Beam steering optimizes output
radiation.

SECTION 6

SUMMARY

Radiation with frequencies ranging from 6 to 60 GHz is generated by the nonlinear interaction of counterpropagating, E-beam-excited EPWs in a plasma-loaded waveguide. The radiation frequency is found to be twice the waveguide plasma frequency. The radiation is strongly amplitude modulated, and modulation pulse width and IPP are related to the ion mass. Ion dynamics clearly play a role in determining the characteristics of the radiation. A beam-current threshold of about 3 A for radiation emission is consistent with the Bennett pinching of the beam; the pinched beam has increased beam density, which leads to larger EPW growth rates and, consequently, to higher radiation powers. Above the beam threshold current, the radiation power increases as I_b^6 up to the maximum beam current available (~10 A). Beam voltage tuning curves validate the model that the EPW growth rates determine an optimum beam voltage for radiation generation.

Unprecedentedly high radiation power ($\leq$8 kW) and high beam-to-radiation power conversion efficiency ($\leq$4%) is estimated. This could be the result of the high background gas pressures required for efficient plasma production. The high-pressure gas increases the threshold of the modulational instability, which would otherwise limit the peak EPW amplitude. Since larger-amplitude EPWs can be excited, higher radiation powers are produced.

REFERENCES

1. K. Papadopoulos, Rev. Geophys. Space Phys. $\underline{17}$, 624 (1979)

2. J. Benford, "High power microwave simulator development," Microwave Journal, p. 97 (Dec. 1987).

3. M.V. Kuzelev, F. Kh. Mukhametzyanov, M.S. Rabinovich, A.A. Rukhadze, P.S. Strelkov, and A.G. Shkvarunets, Sov. Phys. JETP Lett. $\underline{56}$, 780 (1982)

4. L.D. Bollinger and H. Bohmer, Phys. Rev. Lett. $\underline{26}$, 535 (1971)

5. L.D. Bollinger and H. Bohmer, Phys. Fluids $\underline{15}$, 693 (1972)

6. J.R. Apel, Phys. Rev. Lett. $\underline{19}$, 744 (1967)

7. J.R. Apel, Phys. Fluids $\underline{12}$, 640 (1969)

8. D.A. Whelan and R.L. Stenzel, Phys. Rev. Lett. $\underline{47}$, 95 (1981)

9. D.A. Whelan and R.L. Stenzel, Phys. Fluids $\underline{28}$, 958 (1985)

10. R.E. Aamodt and W.E. Drummond, J. Plasma Phys. $\underline{6}$, 147 (1964)

11. R.A. Sturrock, Plasma Phys. $\underline{2}$, 158 (1961)

12. R.A. Sturrock, R.H. Ball, and D.E. Baldwin, Phys. Fluids $\underline{8}$, 1509 (1965)

13. T.J.M. Boyd, Phys. Fluids $\underline{7}$, 59 (1964)

14. K. Papadopoulous, Space Science Rev. $\underline{24}$, 511 (1979)

15. P. Leung, J. Santoru, A.Y. Wong, and P.Y. Cheung, "Physics of Auroral Arc Formation," Giophysical Monograph Series $\underline{25}$, 387 (1981)

16. T. Intrator, N. Hershkowitz, and C. Chan, Phys. Fluids $\underline{27}$, 527 (1984)

17. M. Schneider and M.Q. Tran, Phys. Lett. $\underline{91A}$, 25 (1982)

18. P.Y. Cheung, A.Y. Wong, C.V. Darrow, S.J. Qian, Phys. Rev. Lett. $\underline{48}$, 1348 (1982)

19. D. Bohm and E.P. Gross, Phys. Rev. $\underline{75}$, 1851 and 1864 (1949).

20. M.A. Lampert, J. Appl. Phys. 27, 5 (1956).

21. F.W. Crawford, "Microwave plasma devices - promise and progress," Proc. IEEE 59, 4 (1971).

22. T.M. O'Neil, J.H. Winfreg, and J.H. Malmberg, Phys. Fluids 14, 1204 (1971).

23. S. Kainer, J.M. Dawson, and R. Shanny, Phys. Flu. 15, 493 (1972).

24. S.A. Self, M.M. Shoucri, F.W. Crawford, J. Appl. Phys. 42, 704 (1971).

25. I. Alexeff and F. Dyer, Phys. Rev. Lett. 45, 351 (1980).

26. G.W. McClure, Appl. Phys. Lett. 2, 233 (1963).

27. J.R. Bayless and R.J. Harvey, U.S. Pat. No. 3, 949, 260 (1976) (Assigned to Hughes Aircraft Company).

28. D. Pigache and G. Fournier, J. Vac. Sci. Technol. 12, 1197 (1975).

29. G. Wakalopulos, "Ion Plasma Electron Gun," U.S. Pat. No. 3, 970, 892, Hughes Aircraft Company, July 20, 1976.

30. P.F. Little, "Secondary effects," Band XXI, Vol. XXI, Handbook Der Physics (1956). Also see A.G. Hill et al., Phys. Rev. 55, 463-470 (March 1939).

31. R.W. Schumacher and R.J. Harvey, "CROSSATRON Modulator Switch," Conference Record of the Sixteenth IEEE Power Modulator Symposium," Arlington, Virginia, June 1984, (p. 139).

32. R.W. Schumacher and R.J. Harvey, "CROSSATRON Modulator Switch: A Long-Life Component for Pulsed-Power Systems," Fifth IEEE Pulsed-Power Conference.

33. N.A. Krall and A.W. Trivelpiece, Principles of Plasma Physics, (McGraw-Hill, New York, 1973) p. 495.

34. D.A. Dunn and A.S. Halsted, Proceedings of the Seventh International Conference on Phenomena in Ionized Gases, Vol. 1, 429 (1966).